Technische Universität München
Fakultät für Chemie
Lehrstuhl für Theoretische Chemie

Implementation of DFT+U and its use in simulating Polarons in Oxide- and Battery Materials

Matthias Kick

Dissertation

$$H = U \sum_I n_{I\uparrow} n_{I\downarrow} - t \sum_I \sum_{\sigma=\uparrow,\downarrow} \left(a^\dagger_{I,\sigma} a_{I+1,\sigma} + a^\dagger_{I+1,\sigma} a_{I,\sigma} \right)$$

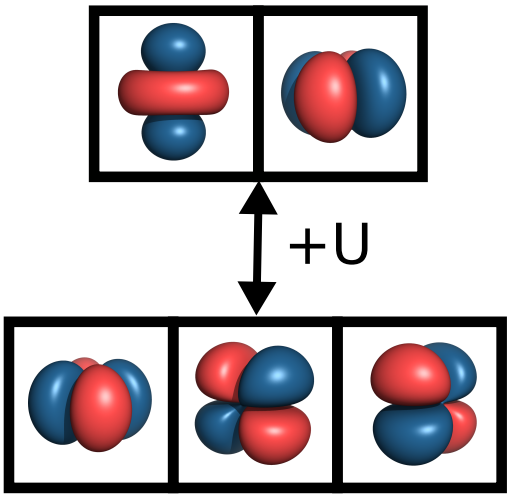

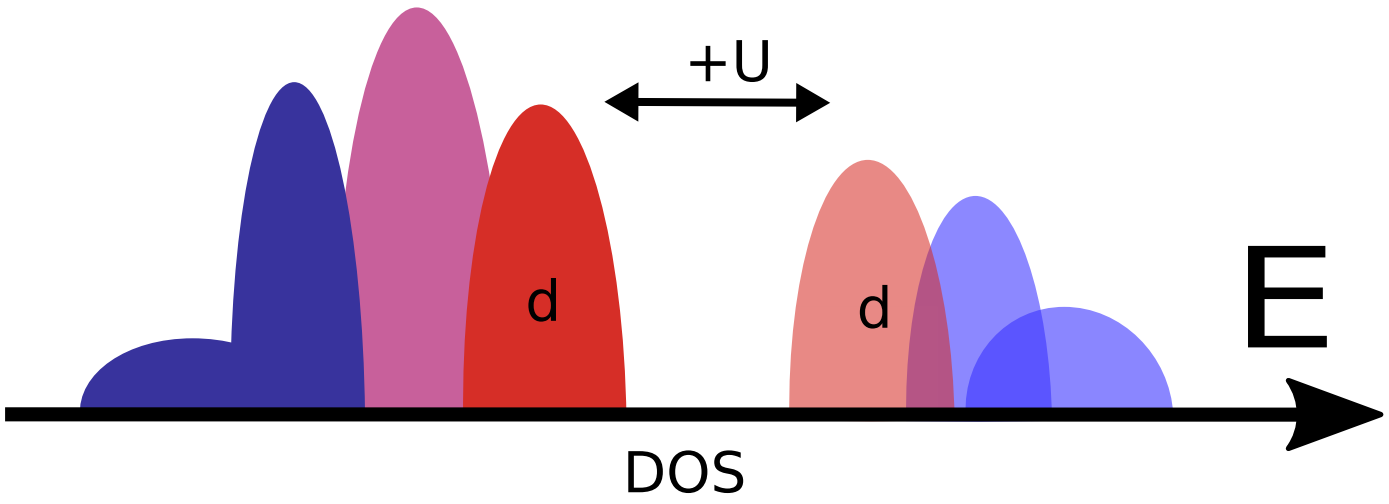

Technische Universität München
Fakultät für Chemie
Lehrstuhl für Theoretische Chemie

Implementation of DFT+U and its use for simulating Polarons in Oxide- and Battery materials

Matthias Kick

Vollständiger Abdruck der von der Fakultät für Chemie der Technischen Universität München zur Erlangung des akademischen Grades eines

Doktors der Naturwissenschaften (Dr. rer. nat.)

genehmigten Dissertation.

Vorsitzender: Prof. Dr. Karsten Reuter

Prüfer der Dissertation:

1. Priv.-Doz. Dr. Harald Oberhofer
2. Prof. Dr. Alessio Gagliardi

Die Dissertation wurde am 05.03.2020 bei der Technischen Universität München eingereicht und durch die Fakultät für Chemie am 13.04.2020 angenommen.

”Ich habe fertig!"

— Giovanni “Trap” Trapattoni —

Preface

This thesis is a publication based thesis. It is based on the scientific work with the title *Intricacies of DFT+U, Not Only in a Numeric Atom Centered Orbital Framework* which is published in *The Journal of Chemical Theory and Computation*. The second work is titled *Towards a Transferable Design of Solid-state Embedding Models on the Example of a Rutile TiO_2 (110) Surface* published in *The Journal of Chemical Physics*. The last publication—*Mobile Small Polarons Explain Conductivity in Lithium Titanium Oxide Battery Electrodes*–deals with Lithium-Ion Batteries. Due to time constraints at the end of my PhD period this work has not yet been published within a peer reviewed journal. It is published on the open access platform *arXiv.org*.

Munich, May 18, 2020

Abstract

Density functional theory (DFT) is by far the most employed method when it comes to the description of extended solid-state systems. Easily explained as it shows great efficiency and accuracy regarding the description of metals and classical semiconductors. However, DFT written in Kohn-Sham formalism has one major drawback which manifests itself in an nonphysical interaction of the charge density. Even if there is just one electron present, the self-interaction error (SIE) does not vanish. As a consequence standard DFT is not suitable to describe systems which are characterized by localized electrons e.g. transition metal oxides or rare earth compounds. In this publication based thesis, we deal with an extension to the usual Kohn-Sham DFT (KS-DFT) formalism. This extension is based on the Hubbard model and adds an *ad hoc* correction term to the DFT Hamiltonian. The so called DFT+U method will be extensively discussed regarding its advantages and disadvantages. A focus will be on pitfalls regarding its practical use. The detailed methodology will be presented in terms of a localized orbital basis set. Further, we explicitly address the formation of small polarons– which is not accessible using standard DFT— and show that polarons can serve as an excellent test case for the DFT+U method. Further, we will demonstrate that polaron formation and DFT+U can also be used to judge the quality of a solid state QM/MM embedding approach. Moving away from method development work, this thesis further demonstrates the capabilities of the DFT+U approach by calculating explicitly the electronic conductivity in lithium titanium oxide (LTO), a promising anode material for future solid state Li-ion batteries.

Zusammenfassung

Die Dichte-Funktional-Theorie (DFT) stellt die am häufigsten verwendete Methode dar, die zur Beschreibung von ausgedehnten Festkörpern verwendet wird. Dies lässt sich dadurch erklären, dass diese Methode eine hohe Effizienz und Genauigkeit hinsichtlich der Beschreibung von Metallen und klassischen Halbleitern aufweist. Jedoch geschrieben im Kohn-Sham-Formalismus, weist DFT einen Nachteil auf, der sich in einer unphysikalischen Wechselwirkung der Ladungsdichte manifestiert. Dieser Nachteil zeigt sich dadurch, dass der sogenannte Selbstwechselwirkungsfehler nicht verschwindet, auch wenn nur ein Elektron im System enthalten ist. Eine Konsequenz daraus ist, dass Standard DFT nicht in der Lage ist Systeme zu beschreiben, die durch lokalisierte Elektronen charakterisiert sind. Dies trifft unter normalen Bedingungen auf Übergangsmetalloxide und Seltenerdverbindungen zu. In dieser voliegenden publikationsbasierten Dissertation wird eine Erweiterung des Kohn-Sham DFT Formalismus vorgestellt. Diese Erweiterung fügt einen *ad hoc* Korrekturterm zum Hamiltonoperator hinzu und basiert auf dem Hubbardmodell. Im Folgenden wird auf die sogenannte DFT+U Methode eingegangen und die Vor- und Nachteile ausführlich diskutiert. Der Fokus ist hierbei auf die Schwierigkeiten gerichtet, die diese Methode hinsichtlich einer praktischen Anwendung, zur Folge hat. Die Details werden anhand eines lokalisierten Basissatzes veranschaulicht. Des Weiteren wird explizit auf die Bildung von kleinen Polaronen eingegangen, welche ein exzellentes Testsystem für DFT+U darstellen und mit herkömmlicher Standard DFT nicht zugänglich sind. Zusätzlich wird demonstriert, dass die Bildung von Polaronen und DFT+U genutzt werden kann, um die Qualität eines QM/MM Einbettungsansatzes zu testen. Im Anschluss wird im Rahmen dieser Arbeit die Fähigkeit dieser Methode beschrieben, indem unter der Verwendung eines DFT+U Ansatzes die Elektronenleitfähigkeit in Lithiumtitanoxid explizit berechnet wird, welches ein vielversprechendes Anodenmaterial für zukünftige Festkörper Lithium-Ionen-Batterien darstellt.

Contents

List of Figures

List of Abbreviations

AMF	around mean-field
cDFT	constraint DFT
DFT	density functional theory
DFT+U	density functional theory with hubbard correction
FHI-aims	Fritz-Haber-Institut *ab initio* molecular simulations
FLL	fully-localized limit
GGA	generalized gradient approximation
HF	Hartree-Fock
KS-DFT	Kohn-Sham DFT
LDA	local spin-density approximation
LTO	lithium titanium oxide
PBC	periodic boundary conditions
SCF	self-consistent field
SIC-DFT	self-interaction corrected density functional theory
SIE	self-interaction error
xc	exchange-correlation

1 Introduction

This thesis is based on three publications on the topic of polarons in oxide materials. The following introductory sections are aimed at familiarizing the reader with all relevant aspects of the methods therein. At the heart of each publication lies the so-called DFT+U approach, therefore, this introduction will guide the reader, in a step-wise fashion, towards a deeper understanding of this method. The main focus therein lies in presenting all relevant theory in an easily understandable manner.

Density functional theory (DFT) is the *de facto* standard when it comes to the description of extended solid-state systems, [1–5] as it is able to describe systems such as metals and classical semiconductors with great efficiency and accuracy.[6] Despite its tremendous success in treating such systems, simulating systems like transition metal oxides or rare earth compounds is still challenging. Characteristic for these type of materials is that they often posses partly filled d- and f-shells with strong localized electrons.[7–10] In such cases, electrons can not longer be viewed as a particle in a bath, they still partly retain their atomic orbital character, [11] and thus are subject to strong Coulomb interactions. Approaching this kind of systems by using semi-local DFT functionals utterly fails. At the heart of this failure is the well-known self-interaction error (SIE) which results from an unphysical density-density interaction which is not completely compensated as it would be in the case of Hartree-Fock (HF) theory. Usually, electron-electron repulsion is therefore overestimated and it is not possible to describe localized electrons in an adequate fashion. The electron density simply suffers from being too delocalized.[12] Several attempts have been made to cure this failure of DFT. Without going into to much detail here, so-called hybrid DFT [13, 14] is possibly one of the most popular approaches to reduce the amount of SIE. However, the evaluation of the corresponding density functional is very costly which limits its use even on modern computer hardware. A very elegant and efficient alternative to hybrid functionals is DFT+U[15–17]. An easy interpretation for DFT+U would be that it describes the Coulomb interaction more accurately than semi-local DFT does by using a model Hamiltonian derived from the Hubbard model [18]. Although its use is in principle restricted to systems characterized by localized electrons, its great strength lies in its simplicity and high efficiency regarding computational costs. Both render DFT+U in principle a powerful simulation method enabling the computation of large extended systems. However, apart from the previously described benefits of using DFT+U, the method is by far not a black box method to use. Choosing the correct on-site Coulomb-interaction parameter and choosing the correct method for counting the number of electrons occupying localized states can drastically influence the outcome of a calculation. An important fact that the standard user is usually not fully aware of.

Within all publications linked to this work, DFT+U is the core method for simulating all ground state properties of the systems in question. Therefore, in a first step the detailed origin of the SIE and its consequences will be addressed. We then move forward to methods which are able to partly cure for the SIE with a focus on advantages and disadvantages. Afterwards, a detailed description of DFT+U is given by comparing it with popular methods such as hybrid DFT. The chapter will

address in detail the origin of DFT+U, aspects such as the definition of the DFT+U occupation matrix or the shape of the projector functions. The latter is a key element in counting the number of electrons occupying localized states. Overall every relevant aspect of DFT+U will be discussed regarding its capabilities and limitations. As one part of the thesis was to implement DFT+U into the Fritz-Haber-Institut *ab initio* molecular simulations (FHI-aims) [19] package, the next chapter then describes what is necessary to implement DFT+U in a modern quantum chemistry code. Also a detailed description of all features is given there.

Furthermore, the scientific publications which have been made during the period of this PhD thesis involve describing the formation of small polarons. At the first glance a concept which is not immediately related to DFT+U. However, a small polaron in this context describes an excess electron which is trapped on a specific lattice cite through the corresponding lattice distortion.[20] Usually, a polaron is quite sensitive to the underlying electronic structure and can therefore serve as a perfect test system for the DFT+U scheme. We make use of this fact in a work [21] published in *The Journal of Chemical Theory and Computation*, which also explains in detail the implementation of DFT+U within FHI-aims.

The standard approach to simulate polarons in solid-state systems is to apply periodic boundary conditions (PBC).[22] However, simulation cells should be rather large in order to prevent interaction of polarons with their periodic image. This is even more critical if the overall system in question possesses a net charge different from zero. Exceedingly large cells are necessary to avoid spuriously periodic interactions.[23, 24] An elegant way to overcome this drawback is to use a so-called solid-state embedding approach (QM/MM).[25] Here, one uses a finite QM-region which is embedded in a point charge environment (MM).[26] The latter mimics the Madelung potential of the in principle infinite crystal.[27] This approach enables studying polarons in the dilute limit and gives easy accesses for studying charged systems as no PBC are required. Moreover, the QM-region usually consists of less atoms then a supercell calculation would involve. Hence, a QM/MM approach enables the use of costly modern higher-rung techniques such as (double-) hybrid functionals [28] for describing solid-state systems.[29] Therefore, the second scientific work presented in this thesis, deals with the question how accurately a QM/MM approach can describe sensitive systems like polarons. Again, the sensitivity of polarons serve as an perfect test case for this kind of approach.

In another scientific work, the established the DFT+U infrastructure of FHI-aims is further used to address the question if a polaron hopping mechanism is responsible for the increase of electronic conductivity in reduced lithium titanium oxide (LTO)—a promising candidate for anodes in future solid state Li-ion batteries.[30–33] Further, by calculating hopping activation energies, we are able to give an upper bound regarding the theoretical possible electronic conductivity in LTO.

In that sense, the aim of chapter 4 is to make the reader more familiar with the concept of a polaron.

The final chapter of this thesis collects a short summary of all publications made during the period of this PhD thesis.

2 Theory

In this chapter, the reader is introduced to the DFT+U formalism and its impact and meaning w.r.t. electronic structure calculations. The focus lies on the ability of DFT+U at least to partially correct for the SIE arising from approximations made in the standard Kohn-Sham DFT (KS-DFT) formalism. This view of DFT+U, as a SIE correction method, is in fact the modern interpretation of DFT+U. The chapter starts with a general introduction to DFT and an explanation of the arising SIE followed by a detailed description of how DFT+U is able to cure this deficit.

2.1 Density-Functional-Theory in a Nutshell

2.1.1 Kohn-Sham DFT

State of the art simulation techniques still rely heavily on DFT due to its tremendous efficiency enabling quantum mechanical descriptions of systems consisting of several hundred atoms. The well known Hohenberg-Kohn theorems [34] lay the theoretical foundations of this theory. They state that once the ground state density of a system is known, every ground state property can in principle be described as a functional of the obtained density. Moreover, the Hohenberg-Kohn theorems also show that there is a variational principle for calculating and finding the ground state density.

Modern quantum chemistry codes apply these theorems almost exclusively using the Kohn-Sham formalism [35] (KS-DFT) which renders DFT a practical computational tool with high efficiency. Although, the Hohenberg-Kohn theorems show that it is possible to describe a quantum system with the corresponding electron density (ρ), only KS-DFT enables fast calculations without explicitly evaluating the wavefunction of a system. The idea behind KS-DFT is to describe the electrons as a system of non-interacting particles which are subject to an effective potential designed in such a way that the density of the non-interacting electron system matches the electron density of the true counterpart. The total energy of the system is then given by

$$E\left[\rho\right] = T_\mathrm{s}\left[\rho\right] + \int \rho\left(\mathbf{r}\right) v_\mathrm{ext}\left(\rho\right) d\mathbf{r} + J\left[\mathbf{r}\right] + E_\mathrm{xc}\left[\rho\right] \quad , \tag{2.1}$$

where T_s is the non-interaction kinetic energy and J describes the classical Coulomb repulsion of a charge density. The external potential $v_\mathrm{ext}\left(\rho\right)$ is an attracting potential due to the presence of positively charged atomic nuclei. Within KS-DFT all quantum mechanical aspects of an interacting many-body system are contained in the so called exchange-correlation (xc) functional E_xc. The above description directly leads to the so called Kohn-Sham equations which define the the electron orbitals Φ_i,

$$\left(-\frac{\nabla^2}{2} + v_\mathrm{ext}\left(\mathbf{r}\right) + v_\mathrm{J}\left(\mathbf{r}\right) + v_\mathrm{xc}\left(\mathbf{r}\right)\right)\Phi_i = \epsilon_i \Phi_i \quad . \tag{2.2}$$

Here $v_{\mathrm{J}}(r)$ and $v_{\mathrm{xc}}(r)$ denote the Coulomb potential and the xc potential, respectively. The latter, as the name already suggests, combines to contributions of electron exchange and correlation interactions. Exchange is a quantum-mechanical interaction which only occurs between particles being in the same spin state. In case of fermionic particles—electrons—this interaction is also known as Pauli repulsion and manifests itself as the Pauli exclusion principle [36] which states that two electrons can not be in the same state at the same time. Correlation instead describes the effect which electrons have on the other electrons due to their own motion.

From the above listed equations it can be easily seen what the implications of the Kohn-Sham formalism are: The electrons move under an effective potential yielding single-particle orbitals from which the electron density of the true system can be constructed by

$$\rho(\mathbf{r}) = \sum_i |\Phi_i(\mathbf{r})|^2 \quad . \tag{2.3}$$

In principle, on its own a single Kohn-Sham orbital does not have any physical meaning at all, only in total they yield the electron density. However, it turns out that in most cases they are very good approximations to the real orbitals of the system.[37]

The above sketched formalism is in principle exact, however, this only holds true if the exact xc functional is known. In practice this is not the case and E_{xc} always needs to be approximated. Obviously an approximated effective potential leads to approximated orbitals and hence to an approximated electron density. In general, the difficulties in finding a proper xc functional arise from expressing all missing quantum mechanical many-body features in terms of the underlying density.[11] However, including missing quantum-mechanical interactions is not the only requirement, a proper xc functional should also correct for the errors made in using a non-interacting electron system. By far the most important error is the so called self-interaction error (SIE)[38, 39]. Without going into detail—the detailed description will be part of section 2.1.2—the SIE arises from an incomplete cancellation of the errors made using a classical Coulomb description for modeling the electron-electron repulsion.[40] Although there exist several attempts to overcome this problem, up to now, none of them is really able to remove the SIE entirely.[11, 12] In general the SIE leads to an over-delocalized electron density and many failures such as the well-known band gap problem can be attributed to it. Moreover, it turns out, that the SIE is one of the major sources for the failing of KS-DFT in yielding a qualitatively incorrect ground state for systems which are characterized by localized electrons—this is often the case in rare-earth compounds and transition-metal oxides with partially filled d- or f-shells.[7–9, 41]

2.1.2 Origin of the Self-Interaction Error

As stated before, one of the major sources for errors in KS-DFT is the self-interaction error (SIE). It arises from the use of a classical Coulomb description for describing the electron-electron repulsion of the non-interacting electron system.[11, 40, 42] Within KS-DFT the Coulomb energy is defined in terms of the density as

$$J[\rho] = \frac{1}{2}\int\int \frac{\rho(\mathbf{r})\,\rho(\mathbf{r}')}{|\mathbf{r}-\mathbf{r}'|} d\mathbf{r} d\mathbf{r}' \quad . \tag{2.4}$$

In that description, the charge density at place $\mathbf{r}$ will interact with the charge density at $\mathbf{r}'$. Obviously, this term does not fully vanish even if there is just one electron in the system.[43] However, at least for a one-electron system it is easy to define the SIE as it is just the given

Coulomb contribution. Therefore, in the limit of having one electron, one can easily derive a first requirement for a proper DFT functional, namely that exchange and Coulomb contribution should cancel each other out. As there is just one electron, of course, the correlation energy should vanish too.[44] This is exactly the case for HF-theory. The spurious self-interaction contribution is cancelled out completely by the corresponding exchange term. This self-interaction-free character of HF is easily verified if one considers the formular for the Coulomb integral,

$$J_{ij} = \int |\Phi_i(\mathbf{r})|^2 \frac{1}{|\mathbf{r}-\mathbf{r}'|} |\Phi_j(\mathbf{r}')|^2 d\mathbf{r} d\mathbf{r}' \tag{2.5}$$

and for the exchange integral

$$K_{ij} = \int \Phi_i^*(\mathbf{r}) \Phi_j(\mathbf{r}) \frac{1}{|\mathbf{r}-\mathbf{r}'|} \Phi_j^*(\mathbf{r}') \Phi_i(\mathbf{r}') \, d\mathbf{r} d\mathbf{r}' \quad . \tag{2.6}$$

Here, the self-interaction terms J_{ii} are canceled out by K_{ii} and within the limit of a one-electron system HF-theory is exact.[45] However, electronic correlation is not included at all. Nevertheless, in a many-body system, it is not so easy to define a unique mathematical definition of the SIE[40, 46] and hence there is no unique recipe to construct the xc functional in such a way that it fully compensates for the unphysical Coulomb contribution.[39] As a result, up to now, approximated KS-DFT is not a SIE-free theory at all.[47] Besides the previous mentioned failures of DFT, the SIE error gives rise to too low orbital energies and leads to an unphysical stabilization of delocalized states. Especially standard local or semi-local functionals which are based on the local spin-density approximation (LDA) [34] or on the generalized gradient approximation (GGA)[48] show a pronounced amount of self-interaction and entirely fail in describing localized electrons.[49, 50] Furthermore, correctly describing the dissociation of rare gas cation dimers or neutral reactions such as the hydrogen abstraction reaction $H_2 + H \longrightarrow H + H_2$ is nearly impossible using standard local or semi-local DFT functionals.[40, 51, 52]. Finally, it should be highlighted, that the systems described in the appendix are also examples where a description using standard DFT functionals will lead to a wrong prediction of electronic ground state properties.

2.1.3 Correcting the Self-Interaction error

In literature there exist several attempts for correcting the SIE. One of them is self-interaction corrected density functional theory (SIC-DFT)[43]. Within SIC-DFT the total energy is given by

$$E^{\text{SIC-DFT}} = E^{\text{DFT}}[\rho] + \sum_i U^{\text{SIC}}[\rho_i] \quad , \tag{2.7}$$

where U^{SIC} is defined as

$$U^{\text{SIC}}[\rho_i] = -\frac{1}{2} \int \int \frac{\rho_i(\mathbf{r}) \rho_i(\mathbf{r}')}{|\mathbf{r}-\mathbf{r}'|} - E_{\text{xc}}[\rho_{i,0}] \quad . \tag{2.8}$$

In that formula ρ_i denotes the density of a single Kohn-Sham orbital Φ_i with $\rho_i, 0$ being the explicit ground-state density. In general, this additional term introduces an orbital-dependent potential to the usual Kohn-Sham description and the SIE is removed orbital wise.[53] However, it usually worsens the atomization energy of molecules [54], and it struggles to correctly describe the stretching of bonds [54] as well as quantities related to thermochemistry.[12] Moreover, without

going into detail, solving equations 2.7 and 2.8 self-consistently results in a large computational overhead, thus limiting its usage. In addition, simply adding the SIC correction (cf. eq. 2.7) to the usual DFT functional, ignores a possible error cancellation between exchange and correlation contributions.[55] Nowadays new attempts have been made to improve SIC-DFT like Fermi-Löwdin orbital self-interaction correction (FLO-SIC) which already showed promising results in small molecular systems.[53, 56–58]

One of the most prominent methods to mitigate the SIE problem is to use hybrid xc-functionals. The idea behind this class of functionals is in fact quite simple. Considering that HF treats the exchange interaction exactly and is SIE-free (see above), hybrid functionals simply admix some percentage of the orbital dependent HF exchange to the xc-functional. Therefore, a general hybrid functional can be written as

$$E_{\mathrm{xc}}^{\mathrm{hybrid}}\left[\rho\right] = E_{\mathrm{xc}}^{\text{KS-DFT}} + \alpha\left(E_{\mathrm{x}}^{\mathrm{HF}} - E_{\mathrm{xc}}^{\text{KS-DFT}}\right) \tag{2.9}$$

where α denotes the mixing factor which determines the amount of HF exchange. Within hybrid functionals, HF exchange (E_x^{HF}) is usually evaluated in the KS-orbital basis. This evaluation is usually considered to be the bottleneck of these class of functionals as the evaluation of the so called Fock integrals is computationally rather demanding. Therefore, despite the power of modern supercomputers, this fact usually restricts the application of hybrid functionals to rather small systems. Moreover, the quality of the results also depends on α, which adds another ambiguity as there is no unique way in determining it. Nevertheless, hybrid functionals showed quite a lot of success in mitigating the SIE in molecular system. Furthermore, they also show remarkable performance in describing systems such as semi-conductors or oxide materials[59]. To name just a few, the most prominent hybrid functionals which are used nowadays are HSE06[13], B3LYP[60, 61], or PBE0[14].

As already mentioned DFT+U can also be seen as a SIE correction method. It is usually employed for the description of localized d- or f-electrons and was originally inspired by the Hubbard-model, cf. section2.2.1 [18]. Moreover, it can be considered to work in a similar way as hybrid functionals do, however, its usage is restricted to just a subset of all electrons. Its great strength lies in the simplicity of its corrective term and its very low computational cost. Generally, the DFT+U correction is usually applied to LDA or GGA based functionals to describe solid-state systems. Applying the Hubbard correction to e.g. hybrid functionals usually results in an overcompensation of the SIE. Nevertheless, there exist also variants of DFT+U which are quite successful in describing molecular systems.[11, 62] The detailed origin of the DFT+U approach and its advantages and disadvantages will be explained in section 2.2.

For completeness, methods based on constraint DFT (cDFT) can also be considered to be methods to compensate for the SIE. Without going into detail, within cDFT a corrective potential is added to the standard Kohn-Sham description in form of a Lagrange-multiplier. The KS-equations are then solved self-consistently under some certain constraint. One such constraint can be to fix the number of electrons located on a certain atom or within a certain fragment of the system. Also constraining the magnetic moment or the atomic charges is possible.[63–65]

2.2 DFT+U

This section should be seen as an introduction to the DFT+U approach and its theoretical background. Therefore, all important aspects of the method will be introduced in a step by step fashion.

2.2.1 The Hubbard Model

The idea behind DFT+U originally comes from the Hubbard model. Within this model one assumes that strongly localized d- or f-electrons are subject to an on-site Coulomb repulsion. Usually, the strength of the on-site Coulomb repulsion is described by the Hubbard parameter U. The Hamiltonian for a 1D lattice is given by

$$H = U \sum_I n_{I\uparrow} n_{I\downarrow} - t \sum_I \sum_{\sigma=\uparrow,\downarrow} \left(a^\dagger_{I,\sigma} a_{I+1,\sigma} + a^\dagger_{I+1,\sigma} a_{I,\sigma} \right) \quad , \tag{2.10}$$

where the second term describes the movement of electrons between different lattice sites I with the hopping strength t. This hopping term is also known from the standard tight binding approach.[66, 67] The first term, however, describes the Coulomb repulsion of electrons which are located at the same lattice site. $a^\dagger_{j,\sigma}$ and $a_{j,\sigma}$ are the fermionic creation and annihilation operators with $n_{j,\sigma} = a^\dagger_{j,\sigma} a_{j,\sigma}$. Here σ denotes the spin index.[18, 68] As already mentioned previously, LDA or GGA based functionals are not able to describe localized electrons in an adequate way. As a remedy, Anisimov *et al.* [15] suggested to augment semi-local DFT with a correction term based on the Hubbard model Hamiltonian and accounting for the on-site repulsion of localized electrons. This has an important implication, namely only the subset of localized electrons are described via the Hubbard model while all the other electrons are still described on the level of standard local or semi-local DFT. Although, in principle, the Hubbard correction can be applied to every state, usually, on-site Coulomb repulsion is strongest for localized d- or f-electrons. Less localized electrons e.g. states with p character are usually not subject to the Hubbard correction.[11, 69]

2.2.2 Arriving at a DFT+U Description

By adding the Hubbard correction term to the DFT description one obtains the following general DFT+U functional,

$$E^{\mathrm{DFT+U}}\left[\rho\right] = E^{\mathrm{DFT}}\left[\rho\right] + E^0_{\mathrm{U}}\left[n_I\right] - E^{\mathrm{dc}}_{\mathrm{U}}\left[n_I\right] \quad . \tag{2.11}$$

Here, E^0_{U} is the energy contribution due to the Hubbard model description. This term now models the localized electronic states and is directly depending on the orbital occupation n_I of these states at lattice site I. The first problem which arises in that description is that all electron-electron interactions are treated by the standard DFT functional as well. In order to avoid a double-counting of interactions one therefore has to subtract $E^{\mathrm{dc}}_{\mathrm{U}}$. However, as indicated by equation 2.11 the Hubbard contribution depends on orbital occupation numbers whereas the DFT functional depends on the electron density.[70] It turned out to be impossible to find a direct link between these descriptions, which means that the double counting correction cannot be derived exactly and needs to be approximated. Different approximations can seriously affect the outcome of a calculation as, of course, they will alter the DFT+U functional. One possible approximations is the so called fully-localized limit (FLL). This is in fact the most common one used in literature. Here, one assumes that the occupation numbers are either 0 or 1.[71] Moreover, it is also assumed that when having integer occupation numbers the SIE in LDA or GGA should be small which means that the DFT part itself should be good enough to describe the system. Therefore, E^0_{U} and

$E_{\mathrm{U}}^{\mathrm{dc}}$ should cancel each other out to restore the actual DFT functional. Next to this form there also exists the around mean-field (AMF) formulation for the double-counting correction designed to describe systems with less localized electrons. There, the basic assumption is that in the limit of uniform occupancy the DFT+U energy contribution should vanish.[11] In the following, for simplicity and without loss of generality, only the FLL approximation will be considered. However, the issue of choosing a proper double-counting correction in a simulation will be addressed later on.

As shown before, the DFT+U correction in principle contains two different terms, the Hubbard part and a double-counting correction. However, in literature both are usually combined to one description,

$$E^{\mathrm{DFT+U}}\left[\rho\right] = E^{\mathrm{DFT}}\left[\rho\right] + E_{\mathrm{U}}\left[n_I\right] \quad . \tag{2.12}$$

In order to gain a better understanding of DFT+U and its impact on the electronic structure of a system it is best to start with DFT+U in its rotationally invariant formulation. It can be derived in a mean-field sense and one arrives at [11]

$$\begin{aligned} E_{\mathrm{U}}^{0}\left[n_{Imm'}^{\sigma}\right] =& \frac{1}{2}\sum_{I,\{m\},\sigma}\Big[\ \langle m,m''|V_{\mathrm{ee}}|m',m'''\rangle\, n_{Imm'}^{\sigma} n_{Im''m'''}^{-\sigma} \\ &+ \left(\langle m,m'''|V_{\mathrm{ee}}|m',m'''\rangle - \langle m,m''|V_{\mathrm{ee}}|m''',m'\rangle\right) \times n_{Imm'}^{\sigma} n_{Im''m'''}^{\sigma}\ \Big] \quad . \end{aligned} \tag{2.13}$$

Here the orbital occupation numbers enter via elements of the so called DFT+U occupation matrix $n_{Imm'}^{\sigma}$.[11, 16] Coming from the Hubbard model, in principle, these are, as already mentioned, the localized orbitals $|m\rangle$ at some certain atomic site I where the index m denotes the magnetic quantum number corresponding to a certain angular momentum l. In other words the elements of these occupation numbers describe the occupations of a certain angular momentum shell on a specific atomic site I. However, using a localized basis set, the localized states are always represented as linear combination of the present basis functions. This has a quite large impact on the complete DFT+U approach as one does not know beforehand what the localized states are and which basis function will contribute most in the linear expansion. Hence, there is an ambiguity in selecting and clearly identifying these localized states. Usually, the occupation numbers are obtained via a projection on more or less localized reference functions which where chosen to resemble the likely shape of the localized orbitals. In practice, as the main focus of DFT+U is to describe d- or f-electrons, one usually projects on the d- and f-manifold of the underlying basis sets simply due to the fact that these basis function can be considered to contribute most to the localized states. This is also consistent with a plane wave basis, however, one does not project onto the basis functions one is projecting the KS states onto predefined reference functions which are often drawn from atomic reference states. Overall, this already shows that the performance of DFT+U is significantly depending on the chosen projector functions.

The corresponding double-counting correction term written using the FLL approximation is given by [11]

$$E_{\mathrm{U}}^{\mathrm{dc,FLL}}\left[n_{Imm'}^{\sigma}\right] = \frac{1}{2}U_I n_I\left(n_I - 1\right) - \frac{1}{2}J_I\left[n_I^{\uparrow}\left(n_I^{\uparrow} - 1\right) + n_I^{\downarrow}\left(n_I^{\downarrow} - 1\right)\right] \tag{2.14}$$

with U_I and J_I being parameters modeling the Coulomb and exchange contribution and $n_I = \sum_{m,\sigma} n_{Imm}^{\sigma}$.

Equation 2.13 shows large similarities with the energy expression known from HF theory[1]. In fact, the integrals involved in that description can be interpreted as Coulomb and exchange contributions. The similarities with equation 2.5 and equation 2.6 can be clearly shown if one writes the integrals explicitly. For example,

$$\langle m, m'' | V_{\mathrm{ee}} | m', m''' \rangle = \int \int \Phi^*_{Im}(\mathbf{r}) \Phi_{Im}(\mathbf{r}) V_{\mathrm{ee}} \Phi^*_{Im'}(\mathbf{r}') \Phi_{Im'''}(\mathbf{r}') \, d\mathbf{r} d\mathbf{r}' \quad , \tag{2.15}$$

Therefore, one can interpret the Hubbard correction as replacing the mean-field density-density interaction with an expression similar to HF.[11] As in HF self-interaction terms are canceled out by corresponding exchange terms. However, here V_{ee} is the screened Coulomb operator.

Here, the similarities to hybrid functionals become quite obvious.[72] Within hybrid functionals one is mixing in a part of exact exchange from HF. As the parameter U in DFT+U determines the strength of the on-site interaction one can also regard the mixing-factor α as the corresponding counter part in hybrid functionals. However, in hybrid functionals all electron-electron interactions are treated in the same way involving the evaluation of explicit Fock-integrals, causing high computational costs. Contrary, within DFT+U the shown integrals are usually factorized and expressed by parameters. Moreover, only a subset of electrons is subjected to the Hubbard correction, all other states are still described by standard local or semi-local DFT. Therefore, in principle, hybrid functionals usually give a more accurate description of the system as they improve the description of all electronic states in the system.

As Perdew *et al.* [73] demonstrated, the energy and density of a system is piece-wise linear w.r.t. to integer electron numbers with lines connecting each integer point. Hence, its derivative should show discontinuities at these points.[39] This is in fact an important property a density functional should have. Now, by incorporating the Hubbard correction into DFT one is able to reintroduce the derivative discontinuity in the exchange-correlation functional [11] This is not fully surprising, as the Hubbard model itself shows a derivative discontinuity.[39] However, this derivative discontinuity is only introduced in the subset of the localized states. The main effect of this is that, if the localized states states form the frontier orbitals of the system DFT+U is able to impose an opening of the band gap proportional to the chosen U parameter.[11]

DFT+U in its simplified Formulation

Equation 2.13 and 2.14 have been introduced to clearly demonstrate how the Hubbard correction describes localized states. However, usually one uses a simpler formulation of the DFT+U functional. One can assume that localized states retain their atomic character and therefore should show similar spherical symmetry. As a result one can simplify integrals involved in expression 2.13 and one obtains the so called spherically averaged from [17] of the DFT+U description,

$$E^{\mathrm{FLL}}_{\mathrm{U}}\left[n^{\sigma}_{Imm'}\right] = \frac{1}{2}\sum_{I,\sigma} U_I \left[\mathrm{Tr}\left(\mathbf{n}^{\sigma}_I\right) - \mathrm{Tr}\left(\mathbf{n}^{\sigma}_I \mathbf{n}^{\sigma}_I\right)\right] \quad . \tag{2.16}$$

Here, the double-counting correction in the FLL is already incorporated. This formulation is the *de facto* standard used in literature.[9, 74–77] Although the clear similarity with HF is lost in this formulation, it shows similar accuracy as the previously introduced formulation which,

[1] $E_{\mathrm{HF}} = \sum_i^N \langle \Phi_i | \hat{h} | \Phi_i \rangle + \frac{1}{2}\sum_i^N \sum_{i \neq j}^N \left[\langle \Phi_i \Phi_j | \frac{1}{|\mathbf{r}_1 - \mathbf{r}_2|} | \Phi_j \Phi_i \rangle - \langle \Phi_i \Phi_j | \frac{1}{|\mathbf{r}_1 - \mathbf{r}_2|} | \Phi_i \Phi_j \rangle \right]$,
with N being the number of electrons.

however, does not account for orbital dependent interactions. From eq. 2.16 it is also clear why the computational overhead of a standard DFT+U calculation is only marginal compared to LDA or GGA calculations. No integrals need to be evaluated, the only quantity which needs to be determined is the DFT+U occupation matrix n_I^σ.

From equation 2.16 one can derive the effective potential which will enter the Kohn-Sham Hamiltonian quite easily by

$$v_{Imm'}^{\sigma,\mathrm{FLL}} = \frac{\partial E_{\mathrm{U}}^{\mathrm{FLL}}}{\partial D_{ij}^{\sigma}} = -U_I \left(n_{Imm'}^{\sigma} - \frac{\delta_{mm'}}{2} \right) \quad . \tag{2.17}$$

Here, D_{ij}^{σ} denotes a general matrix element of the contracted density matrix of the system. The meaning of this equation can be interpreted as following: if an orbital is fully occupied, meaning it shows an occupancy of 1, the orbital energy is subject to a down shift of $-\frac{U}{2}$. On the other side, if the orbital is empty it is shifted up in energy by $\frac{U}{2}$. As a result, if the orbitals form the frontier orbitals of the system, DFT+U is able to introduce a band gap opening proportional to the on-site strength U. This fact is illustrated in Figure 2.1 where a band gap is introduced between the d-bands. Another interpretation is that the DFT+U correction in the FLL approximation acts as a penalty function which enforces the system to have either full or empty orbitals. This is analogous to cDFT where an energy penalty is imposed if the electron density does not match the employed constraint.[63]

As the effect of DFT+U is to shift d- or f-bands up and down in energy, one can easily imagine, that with a high enough U value, at some point, one would shift one band over another. In other words one could change the energetic ordering of the different bands if the U value is high enough. In addition the hybridization between the states of course is also affected. As a consequence, improvement of the electronic structure will only take place within a certain range of U values. A too large U value could lead to overcompensation and hence to an entirely wrong electronic structure.

2.2.3 The on-site U Parameter

So far it has only been mentioned that U measures the strength of the on-site repulsion of electrons. However, the question still remains how to obtain the correct parameter for a certain system. The problem is that U depends on the chemical environment of the atomic site in question. In principle this means one has to determine for each specific site a unique interaction parameter. However, in practice one considers different parameters only for different atomic species. Even worse, it does not only depend on the chemical environment it also depends on the underlying basis set of the quantum chemistry code, making it impossible to compare the U parameters between different codes. The standard strategy to determine the parameter is to simply fit it to some experimental data. This means one would then choose some experimental observable like e.g. the band gap and tune the U parameter until simulation and experiment agrees. The obtained U value is then used in further simulations to predict other material parameters.[11] It is important to note, though, that such an approach makes DFT+U a semi-empirical method. On the other hand, there is still the possibility to calculate the U parameter using a linear response approach.[78, 79] A quite elegant method if there is no experimental data available, however, care must be take to ensure that the calculated U parameter is still physically meaningful. Both methods have in common, that one should never use U parameters obtained from different electronic structure packages as this can in principle lead to the prediction of unphysical results.

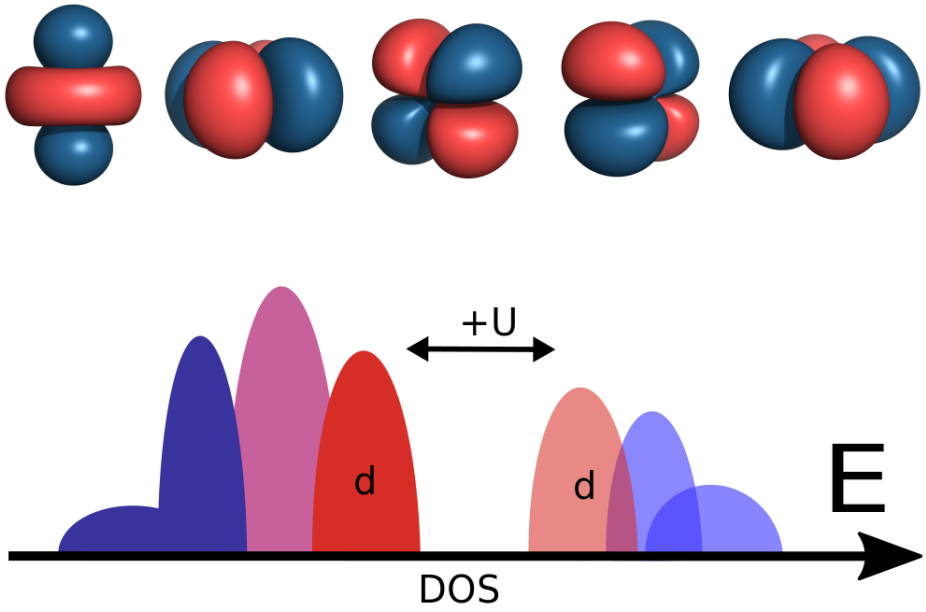

Fig. 2.1: *Illustration of the band gap opening between the d-states of a system. The amount of how the band gap is increased is proportional to U if the localized states are the frontier orbitals of the system. Also illustrated are the d-orbitals to which the +U correction is usually applied. Unoccupied states are depicted in transparent color.*

2.2.4 Double-Counting Correction

As already mentioned, there are two common approximations for the double-counting correction, the FLL and AMF approaches. So far, for the sake of simplicity, only DFT+U in its FLL formulation has been discussed. As already mentioned, FLL is widely employed in literature often without ever mentioning which double-counting actually was used, simply due to the fact that most of the quantum chemistry packages do not offer to switch to other definitions. However, one can consider the FLL as best suited for describing systems which are characterized by strongly localized electrons. This already justifies its predominant usage as DFT+U is actually designed for describing such systems. Nevertheless, it is worth mentioning that there exists also a double-counting correction for less localized electrons with the around mean-field (AMF) description. As already mentioned in section 2.2.2 within the AMF approximations one assumes uniform occupancy of the localized states. Like in the FLL where the energy term vanishes if integer occupation numbers are reached, the energy term in the AMF description vanishes if all orbitals are equally populated. The energy correction to standard DFT is then given by [11, 70]

$$E_{\mathrm{Us}}^{\mathrm{AMF}}\left[n_{Imm'}^{\sigma}\right] = \frac{1}{2}\sum_{I,\sigma} U_I \,\mathrm{Tr}\left(\left[\mathbf{n}_I^{\sigma} - \frac{\mathrm{Tr}\left(\mathbf{n}_I^{\sigma}\right)}{2l+1}\right]^2\right) \quad . \tag{2.18}$$

Of course the above equation is again written in its spherically averaged form where l denotes the angular momentum quantum number of the shell to which the Hubbard correction is applied. Also for this description one can derive a formulation for the effective potential which will enter the DFT Hamiltonian matrix, namely

$$v_{Imm'}^{\sigma,\mathrm{AMF}} = -U_I \left(n_{Imm'}^{\sigma} - \frac{\mathrm{Tr}\left(\mathbf{n}_I^{\sigma}\right)}{2l+1}\delta_{mm'} \right) \quad . \tag{2.19}$$

Here, the localized orbitals are subject to an upward or downward shift depending on how the occupancies are differing from the average occupation of the corresponding shell. In other words, it imposes an energy penalty on the states which differ from uniform occupancy. In contrast to FLL which imposes a energy penalty if the occupation number is differing from 0 or 1.

Strictly speaking, the truth lies somewhere between the two described limits. Therefore, attempts have been made bridging these two approximation using a linear interpolation scheme.[70] However, this approach is not frequently used in literature as for example FLL. One reason is that FLL shows a better ability to describe Mott localization and it is also more suitable for increasing the band gap in the KS spectrum.[11] As a general note, the double-counting correction has to be chosen according to the properties of the system in which one is interested in. Of course, a wrong choice of the double-counting correction could yield an incorrect electronic ground-state.

2.2.5 Obtaining the Occupation Number Matrix

A very important aspect of DFT+U is the question of how one obtains the occupation numbers from the underlying electron density. The question is related to the problem of identifying the localized states out of the Kohn-Sham state spectrum. This is not a trivial task due to hybridization of the orbitals and mixing of the states. In principle, one has to identify the states which contribute to the localized d- and f-states. Moreover, they should enter the correction according to their weight depending on how they contribute to the localized states. Such difficulties are closely related to the problem of finding the angular momentum character of an orbital or its contribution to the partial charge of an atom. In the case of assigning partial charges to a specific atom, there exist quite a number of approximations such as the Mulliken method [80] or the Löwdin population analysis [81]. Both have in common that the contribution of a Kohn-Sham state to a specific angular momentum state or due to a localized orbital is determined by a projection of all Kohn-Sham states onto a reference representation of a specific state, called projector function. Within DFT+U these projector functions are also often termed Hubbard projectors. Of course, different choices of projector functions can affect the outcome of a calculation and for each system or each element one has to determine in principle a unique set of projector functions. However, for simplicity and to avoid excessive computational overhead, common choices for projector functions are the basis functions of a localized basis set itself. This closely follows the assumption that basis function of specific d- or f-character will largely contribute to the localized states. Nevertheless, there exists also implementations using for example maximally localized Wannier functions.[62] For more details regarding the influence of the projector functions the reader is referred to [21] which is also included in the appendix of this thesis.

As this thesis is concerned with the implementation of DFT+U into the FHI-aims package [19], all working equations regarding the determination of the occupation numbers will be introduced

in terms of a localized basis set.
As already mentioned, the occupation numbers in DFT+U enter via the so called DFT+U occupation matrix. This matrix is in general defined via a local projection operator, $\hat{P}^{\sigma}_{Imm'}$.[82] One can then obtain the corresponding matrix elements of $\mathbf{n}^{\sigma}_{I}$ by calculating the projection of all Kohn-Sham states,

$$n^{\sigma}_{Imm'} = \sum_{\gamma} f_{\gamma} \langle \Phi^{\sigma}_{\gamma} | \hat{P}^{\sigma}_{Imm'} | \Phi^{\sigma}_{\gamma} \rangle \quad . \tag{2.20}$$

In the above formular f_{γ} denotes the occupation of a certain Kohn-Sham state Φ^{σ}_{γ}. The index m here then denotes the index of the projection function associated to a certain magnetic quantum number of a specific angular momentum shell. The index I is again the atomic site index. In principle, projector functions here can be the basis functions itself or linear combinations of the basis functions as long as they can be associated to a certain angular momentum. At that point it is also quite useful to speak in terms of a localized subspace instead of localized states simply due to the fact that by projecting onto reference functions only a certain subspace will be affected by the DFT+U correction.[83]

Things get even more complicated as not only the choice of the projector functions affect the description but also the definition of the projector operator itself. To date now there is no unique way to define such a projector which accounts for the number of electrons on an atom.[11, 82, 83] Within DFT+U three different common choices for the operator exists, differing in the way how they account for the overlap with the surrounding basis functions. In other words, they differ in the way how they assign electrons to an atom occupying also neighboring basis functions.

One of the simplest choices for the projection operator is the so-called on-site representation where the projection operator is given by

$$\hat{P}^{\sigma}_{Imm'}(\text{on-site}) = |\tilde{\varphi}^{\sigma}_{Im'}\rangle \langle \tilde{\varphi}^{\sigma}_{Im}| \tag{2.21}$$

Here, the $\tilde{\varphi}^{\sigma}_{Im'}$ determines the Hubbard projectors dual, which are defined in terms of the inverse overlap matrix S^{-1},

$$|\tilde{\varphi}^{\sigma}_{Im}\rangle = \sum_{m'} S^{-1}_{Imm'} |\varphi^{\sigma}_{Im'}\rangle \quad . \tag{2.22}$$

They are introduced in order to avoid to carry the overlap matrix, used to orthogonalize the projections, throughout all calculations.[80, 84]

Another possible definition for the projection operator is the dual representation [82],

$$\hat{P}^{\sigma}_{Imm'}(\text{dual}) = \frac{1}{2}\left[|\tilde{\varphi}^{\sigma}_{Im'}\rangle \langle \varphi^{\sigma}_{Im}| + |\varphi^{\sigma}_{Im'}\rangle \langle \tilde{\varphi}^{\sigma}_{Im}| \right] \quad . \tag{2.23}$$

In that description the occupation numbers are determined in a similar fashion as in the Mulliken population analysis. The third variant is the so called full projection operator where one defines the projection as

$$\hat{P}^{\sigma}_{Imm'}(\text{full}) = |\varphi^{\sigma}_{Im'}\rangle \langle \varphi^{\sigma}_{Im}| \quad . \tag{2.24}$$

All have in common that they yield Hermitian effective potentials which are added to the DFT Hamiltonian. The on-site definition completely neglects the overlap to the surroundings, whereas

the full definitions accounts for the complete overlap with all other sites. The dual representation can be regarded as an intermediate form between on-site and full. It is also the only definition which yields the correct amount of electrons which are contained in the localized subspace.[82] From this perspective it seems to be clear that the dual representation should be the best definition. However, studies regarding the performance of the occupation matrices for various transition metal oxides have shown that there is no clear advantage of any specific representation. All occupation matrices showed nearly identical behavior.[85] This is easily explained that different counting of electrons can be compensated by simply adjusting the U parameter. For completeness, it should be noted that all these definitions are not fully tensorial-consistent. In other words products of the occupation matrices are not physically meaningful. Without going into detail, this would involve defining a covariant-contravariant formulation of the DFT+U occupation matrix. The interested reader is referred to reference [83].

In the special case if the Hubbard projectors are exclusively defined as basis functions, one can easily derive the following working equations for the occupation number matrix elements. For the on-site definition within the $(2l+1)$ manifold of a certain subset of the basis set one obtains

$$n^{\sigma}_{Imm'}(\text{on-site}) = D^{\sigma}_{Imm'} \quad , \tag{2.25}$$

for the full occupation matrix one yields

$$n^{\sigma}_{Imm'}(\text{full}) = \sum_{Jn,J'n'} S_{Im,Jn} D^{\sigma}_{Jn,J'n'} S_{J'n',Im'} \tag{2.26}$$

and finally for the dual representation the corresponding matrix elements are

$$n^{\sigma}_{Imm'}(\text{dual}) = \frac{1}{2} \sum_{Jn} \left[D^{\sigma}_{Im,Jn} S_{Jn,Im'} + S_{Im,Jn} D^{\sigma}_{Jn,Im'} \right] \quad . \tag{2.27}$$

Again, $D^{\sigma}_{Jn,J'n'} = \sum_{\gamma} f^{\sigma}_{\gamma} c^{\sigma}_{\gamma,Jn} c^{\sigma *}_{\gamma,J'n'}$ is the density matrix of the system with $c^{\sigma}_{\gamma,Jn}$ being the expansion coefficients in a linear combination of atomic orbitals approach. The index n then denotes a general basis functions located at an atom J of the system. At this point the author would like to highlight that, due to its simplicity, the on-site representation showed greater numerical stability as the other definitions during the calculations.

2.2.6 The DFT+U Matrix Control Approach

The Hubbard correction to the DFT Hamiltonian is an orbital dependent potential. It acts, as previously explained, as a penalty function on the occupation of the localized orbitals. This is problematic as depending on the initial orbital occupation one can get easily trapped in meta-stable states as they potentially can show a large energy barrier which can not be overcome during an self-consistent field (SCF) cycle.[41, 86] As a result, one can obtain a wrong ground state prediction. To overcome this drawback of DFT+U one can use the occupation matrix control approach.[10, 86] In this rather simple approach one fixes the occupation matrix of a system and modifies the diagonal entries of the occupation matrix. In other words, in order to obtain a certain orbital configuration, such as e.g. a polaronic state in a semiconductor, one would then specify the specific configuration at the beginning of a calculation. There are two possible options, one could either fix the occupation matrix for a certain number of SCF steps or for the entire run. For the latter, in order to obtain an SCF solution one would use the obtained density as an input for a second

calculation without fixing the occupation matrix. Fixing the occupation matrix, in principle acts like a bias potential analogous to the cDFT approach. The electron density will then adapt to the enforced orbital configuration. By this, one can screen different orbital configurations in order to clearly determine the global minimum of the system. Moreover, this approach can also be used to enforce a specific localization of excess charges. In order to illustrate how this simple approach works Figure 2.2a) schematically depicts an occupation matrix for a $3d$-shell of a Ti atom in bulk TiO_2. In Figure 2.2b) this occupation matrix has been modified by setting one of the diagonal elements to 1.00.

2.2.7 A last Comment on DFT+U Theory

So far, quite a lot of different aspects of DFT+U have been introduced. Despite its rather simple working equations, its impact on the electronic structure of the studied system can be quite large. The choice of the double-counting correction, the question which Hubbard projector is the best for the system, and the ambiguity in the definition of the occupation matrix can be quite confusing, rendering the DFT+U approach a method quite far away from being a black-box method. Nevertheless, its strength lies in its high efficiency. In fact if the studied quantity is mainly characterized by localized d- or f-electrons, DFT+U is able to describe the system with similar accuracy as a hybrid functional would do. However, DFT+U shows very little computational overhead compared to standard LDA or GGA calculations [75] enabling the study of large extended systems. Describing a system accurately requires a correct choice of U as observables can show large sensitivity regarding the applied U. Therefore, in practice, one should test how the observable is changing w.r.t. the applied U value.

a) Ti 3d

0.12	0.00	0.04	0.00	0.00
0.00	0.13	0.00	0.04	0.00
0.04	0.00	0.09	0.00	0.00
0.00	0.04	0.00	0.13	0.00
0.00	0.00	0.00	0.00	0.09

b) Ti 3d modified

0.12	0.00	0.04	0.00	0.00
0.00	0.13	0.00	0.04	0.00
0.04	0.00	1.00	0.00	0.00
0.00	0.04	0.00	0.13	0.00
0.00	0.00	0.00	0.00	0.09

Fig. 2.2: *Displayed in a) is the* 3*d occupation matrix of a Ti atom in* TiO_2*. In b) the same matrix is shown however one of the diagonal elements is set to 1.00. As the diagonal elements are related to the occupation numbers of a specific orbital, this can be used to localize an excess charge on this specific atom.*

3 Implementing DFT+U

In this chapter the reader will be introduced step by step to the program workflow of the DFT+U implementation in FHI-aims. The chapter will begin with a short introduction of the FHI-aims basis set and the basis set terminology, which can be rather confusing for users who are not familiar with FHI-aims in general. In the end we demonstrate in a small scaling test, that DFT+U shows in fact very little computational overhead. It should also be highlighted, that this chapter can also be viewed as a small introductory manual for using DFT+U in FHI-aims.

3.1 FHI-aims

The Fritz-Haber-Institut *ab initio* molecular simulations (FHI-aims) program package [19] is an all-electron full-potential electronic structure code designed for efficiency up to large scale atomic simulations. Its focus lies on DFT offering a various number of xc-functionals. However, methods beyond DFT such as second-order Møller-Plesset (MP2) perturbation theory, the random phase approximation (RPA), or self-consistent GW are also included in the package. Within FHI-aims KS-states are expanded using a numeric atom centered orbital orbital basis set, where a general basis function ϕ_i is defined as

$$\phi_i(\mathbf{r}) = \frac{u_i(r)}{r} Y_{lm}(\Omega) \quad . \tag{3.1}$$

Here, Y_{lm} are real-valued spherical harmonics. The radial part u_i is chosen to be a solution of a Schrödinger-like radial equation. It is numerically tabulated and therefore fully flexible. The basis set is arranged hierarchically. This means each element specific basis set consists of a so called minimal basis—these are free atom solutions of the corresponding element—followed by a set of preconstructed basis functions which are subdivided in so called *tiers* (*tier1*, *tier2*, ...). The latter mainly consists of hydrogen-like basis functions serving as polarization functions[1] for the minimal basis set. In general, the hierarchical arrangement is designed in such a way to yield systematic convergence from fast and qualitative to milli-electronvolt-level total energy convergence. Numerical integrations are performed on predefined logarithmic grids.[60, 87, 88] According to their accuracy, the grids are termed *light*, *tight* and *really tight*.

In general this terminology can be rather confusing for user not familiar with FHI-aims. Therefore, as a practical remark, the accuracy of a *light tier1* basis set is comparable with a triple-ζ valence polarized gaussian type basis set.[89]

3.2 General Program Workflow

In a DFT+U-corrected FHI-aims run, the program first selects—according to the specific input—the type of Hubbard projectors from which the occupation matrix later will be formed. Within FHI-

[1] Functions of higher angular momentum are usually added to the basis set for allowing polarization of lower angular momentum functions.

aims, two types of DFT+U runs are available, first one could simply calculate the DFT+U occupation matrix from a projection onto the (*2l+1*) manifold of the minimal basis set. As these basis functions are basically free atom solutions, one could expect them to be a first good approximation to the localized orbitals in question. This means if one requests the DFT+U correction for a 3*d* transition metal, the subspace of the five 3*d* basis functions of the minimal basis set are subject to the Hubbard correction. Second, as already explained in section 3.1, besides the minimal basis set there are also polarization functions usually present in a calculation. As a consequence one can end up having multiple sets of basis functions which belong to the same l channel, however, having a possible different radial extent. The influence of such a basis on the Hubbard correction is not entirely clear. Should these basis functions also be included for calculating the occupation numbers? This topic will be discussed in much more detail in the corresponding publication which is summarized in section 5.1. However, in this situation FHI-aims allows the construction of Hubbard projectors as a linear combination of all basis functions which show the same l. Thus, in principle, arbitrary basis-set representable Hubbard projectors could be used in FHI-aims. This gives a lot of flexibility in defining the localized subspace for which the Hubbard correction should account for. Up to now defining Hubbard projectors as explicit linear combination of basis functions is somehow unique in FHI-aims, however, there exist implementations where multiple sets of polarization functions are treated as a multiple set of angular momentum shells each with a unique U value.[82, 90] For more details according the choice of Hubbard projectors the reader is referred to reference [21]. As a next step the program checks if the matrix control approach has been requested. If not, the DFT+U occupation matrix is then constructed for the first time using the initial density matrix of the system. Afterwards, the code will build the effective on-site potentials for each atom for which the Hubbard correction should be applied. After the DFT Hamiltonian matrix is constructed the effective potential is applied. After diagonalization one then can evaluate the DFT+U energy functional. This will be repeated self-consistently within the standard KS-DFT routines until all convergence criteria are met. If DFT+U occupation matrix control is enabled, instead of calculating the occupation matrix, the occupation matrix will be taken from a file which can be customized according to the users needs. This procedure then continues in the same way as without applying matrix control. After evaluating the DFT+U energy description, the program checks if the total energy is converged within a predefined additional convergence criteria—it is usually not as strict as the standard convergence criteria for the total energy. If this convergence criteria is fulfilled the occupation matrix is then calculated self-consistently. With this procedure one can first ”preconverge" the density according to a predefined orbital configuration and use it afterwards as basically the starting point for a SCF solution. In Figure 3.1 the previously described steps are depicted in a program flow-chart for better overview.

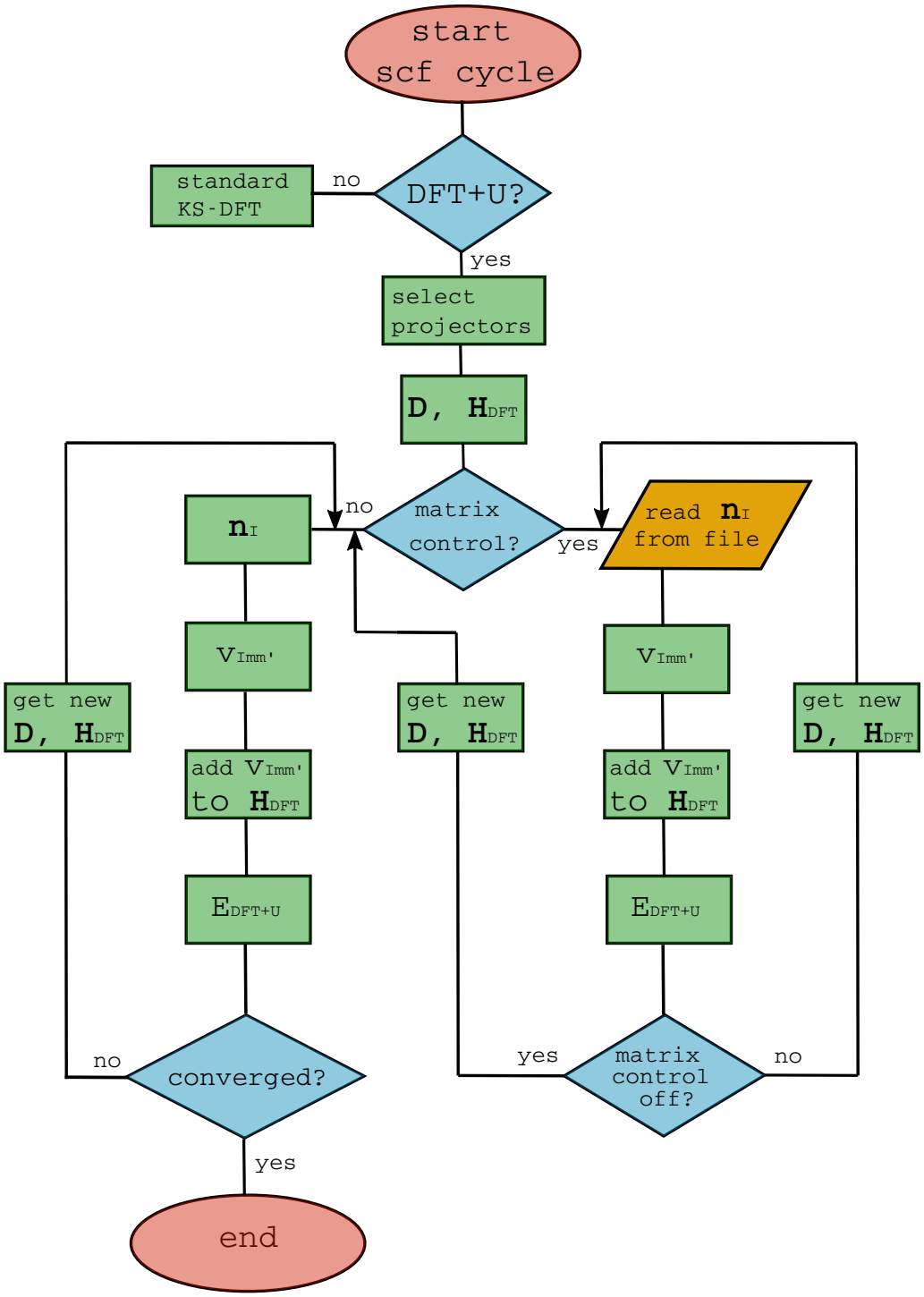

Fig. 3.1: *Schematic representation of how the DFT+U correction is applied during a SCF cycle. Also shown how it changes if the matrix control approach is applied.*

3.3 Full Feature Overview

In the previous section only the general workflow of DFT+U within the framework in FHI-aims has been introduced. In addition, the following list will provide an overview of all capabilities of the current DFT+U implementation in FHI-aims. However, this should not be regarded as a full keyword list. For a full specification how to use each feature the reader is referred to the FHI-aims manual.

`occupation_matrix`: The user can choose between `on-site`, `dual` and `full` representation. All representations are fully supported.

`hubbard_projectors`: A projection onto atomic basis functions of the minimal basis set is the default setting. Alternatively, one can specify a customized Hubbard projector as linear combination of basis functions.

`atomic_forces`: Atomic force correction terms are up to now only supported for the on-site representation.

`matrix_control`: DFT+U occupation matrix control is provided for all representations. The user has to provide a file containing the orbital configurations.

`dft+u_ramping`: Starting from zero the U value will be step-wise increased if a certain convergence criteria was met. Useful, if achieving a SCF solution is quite hard.

`double-counting`: The code offers FLL, AMF and a linear interpolation between both limits as double-counting correction.

`eigenvalues`: Allows the calculation of the specific eigenvalues of the DFT+U occupation matrix.

Besides the above mentioned features, the code also performs a check of the DFT+U occupation matrix in each SCF iteration. If not physically meaningful, the code issues a warning and stops the calculation. Furthermore, the code is designed in such a way, that a different +U treatment—different U value and different l shell—can be requested for each species.

3.4 Scaling Test

Bulk NiO can be considered a prototypical compound for testing and demonstrating the capabilities of DFT+U.[70, 82, 83, 85, 91, 92] It belongs to the class of highly correlated materials showing strong localization of Ni 3d electrons. Standard functionals based on LDA or GGA predict it to be a Mott-Hubbard type insulator[93] where the Ni 3d form the valance and conduction band edges.[94] On the other hand, experimental data shows evidence of having a charge-transfer type band gap where the O 2p states are dominating the top of the valance band.[95] As one of the

main effects of DFT+U is to shift the states up and down in energy according to their occupancy, the erroneous description of standard DFT functionals can easily be cured if the Ni 3*d* states are subject to the Hubbard correction.

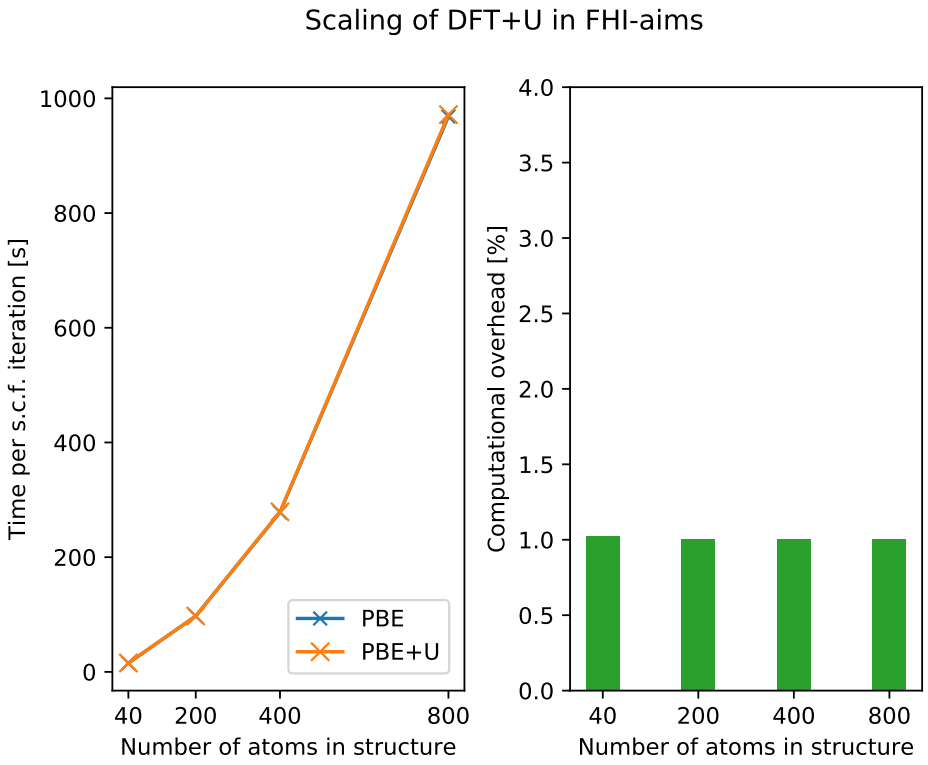

Fig. 3.2: *Scaling behavior of the DFT+U implementation within FHI-aims. The calculations have been carried out on an Intel Xeon on Platinum 8174 processor. The computational cost of DFT+U is only marginally higher compared to the PBE calculation.*

For the scaling test a preoptimized PBE [48] bulk NiO unit cell consisting of two Ni atoms and two O atoms served as a starting point. From that structure, supercells have been created containing up to several hundred atoms. Furthermore, a *tier1* basis set and *light* settings for the integration grid are employed. For the Hubbard correction, a U value of 3.0 eV and the FLL have been applied. The Ni 3*d* atomic basis functions of the minimal basis set serve as Hubbard projectors.

The calculations have been carried out on an Intel Xeon Platinum 8174 processor applying MPI parallelization only. Figure 3.2 compares the scaling behavior of the code with a standalone PBE calculation. Also shown is the percentage of the total computational overhead compared to a pure PBE calculation.

Not surprisingly, the scaling behavior of FHI-aims is not entirely linear w.r.t. system size. However, as one can clearly see, there is no significant overhead caused by the DFT+U routines. In fact, the additional overhead is in the range of 1%. This demonstrates how efficient DFT+U actually is and that a DFT+U calculation does not take significantly longer as a LDA or GGA calculation would do. However, for this calculation basis functions have been served as Hubbard projectors,

other methods without directly projecting onto basis functions can show larger computational overhead. In addition, the DFT+U routines themselves do not contain grid operation or diagonalization routines, which means that DFT+U settings are not affected by accuracy settings such as larger basis sets or denser integration grids. In other words, increasing the accuracy will lead to a significant decrease in the relative overhead. Timing and scaling will always be dominated by diagonalizing the Hamiltonian matrix of the system independent of the +U correction.

4 Localized Electrons—Small polarons

This chapter has the aim to briefly introduce the unfamiliar reader to the concept of small polarons as all publications within this thesis deal with the correct description of such phenomena.

4.1 The small Polaron Concept

A moving localized charge carrier such as an negatively charged electron or a positively charged hole will cause ionic displacement within a crystal. The charge carrier in combination with the lattice distortion can be described as a quasi particle called polaron (cf. Figure 4.1). In some materials—depending on the interaction strength—the lattice distortion can create a potential strong enough to cause self-trapping of the charge carrier. Is the induced lattice distortion locally confined this polaron is usually referred to as small polaron. These type of polaronic states are usually localized within one unit cell of the material.[20]

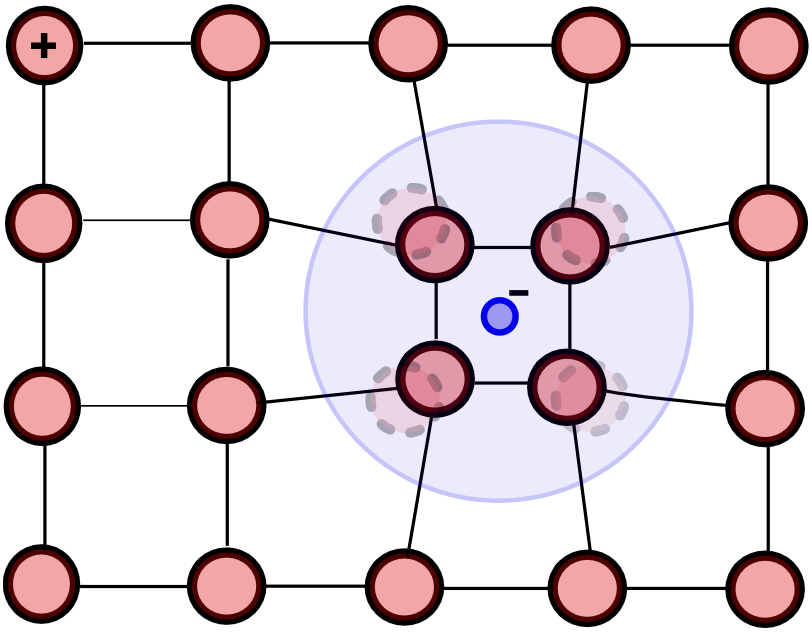

Fig. 4.1: *Schematic representation of a polaron. The negative charge carrier (blue) causes a distortion within the cationic lattice (red). Lattice distortion and charge carrier together can be described as a quasi particle, a polaron.*

An important feature of small polarons is their temperature dependent movement through the crystal. Is the temperature large enough, polarons can hop from one lattice site to a neighboring

one. This process is usually much more relevant than tunneling processes as the hopping on average occurs more often.[20] Without going into detail, the thermal activation of the polaron hopping can be described via an Arrhenius-like equation [20, 96],

$$\mu = \frac{e\alpha^2\omega_{\mathrm{LO}}}{6k_{\mathrm{B}}T} exp\left(-\frac{E_{\mathrm{A}}}{k_{\mathrm{B}}T}\right) \quad . \tag{4.1}$$

Here, μ describes the mobility of a small polaron with α being the hopping distance. e is the elementary charge. Among all electron phonon interactions it is to be considered that the long-wave longitudinal optical phonons with constant frequency ω_{LO} are the most relevant ones. Most important in eq. 4.1 is the hopping activation energy E_{A}. This activation energy or activation barrier is usually obtained using the Nudge Elastic Band approach [97, 98] or a linear interpolation of nuclear coordinates between initial polaron location and final polaron location. It should be noted that both approaches require having a well-defined transition state or in other words it is assumed that hopping is an adiabatic process.[50]

Polaron hopping has a significant part in the electronic conductivity in some certain materials, especially transition metal oxides.[20] Besides their contribution to the electronic conductivity, it is to be considered that polarons can also play a crucial role in chemical reactions. For example, photogenerated electrons and holes within TiO_2 can get self-trapped. Here, the electron polaron is located at a Ti atom whereas the "hole polaron" is forming on an oxygen atom. Furthermore, as the trapping energy is usually larger at the surface, polarons will move towards the surface and can drive a possible reaction.[99] The importance of polarons is also known from CO adsorption on TiO_2 as CO shows attractive coupling with surface polarons.[100] Overall, it is to be considered that polarons play a major role in understanding the properties of polar semiconductors, or transition metal oxides in general.[100]

4.1.1 A Comment on simulating Polarons

Simulating polarons is usually quite challenging. In the case of electrons, semi-local DFT is generally not able to describe them in an adequate fashion due to the large amount of self-interaction error inherent to such functionals. One has to apply at least DFT+U or hybrid functionals to account for the proper amount of charge localization. Even applying DFT+U or hybrid functionals does not yield a polaron *per se*. Symmetry breaking is required [75], which can be achieved by distorting the crystal lattice by hand or by introducing defects (cf. Figure 4.2). Moreover, the various possible localization sites within a unit cell show often more or less the same energy and are usually only separated by a small energy barrier which renders sampling of different localization patterns quite a hard task. A common strategy is to modify the bonding distance to neighboring atoms in order to pre-introduce the lattice distortion.[75, 101] Especially if DFT+U is employed, one can make use of the matrix control approach for sampling polarons.[21] Another common strategy is to use artificial high U values on the sites in order to enforce charge localization there.[74] Of course this only works if the charge carrier is an electron. Not to forget that if one wants to study a single polaron one has to ensure that the polaron does not interact with its periodic images. As a consequence, simulating polarons makes it necessary to employ rather large cell sizes [21, 74] or advanced embedding techniques (cf. section 5.2).

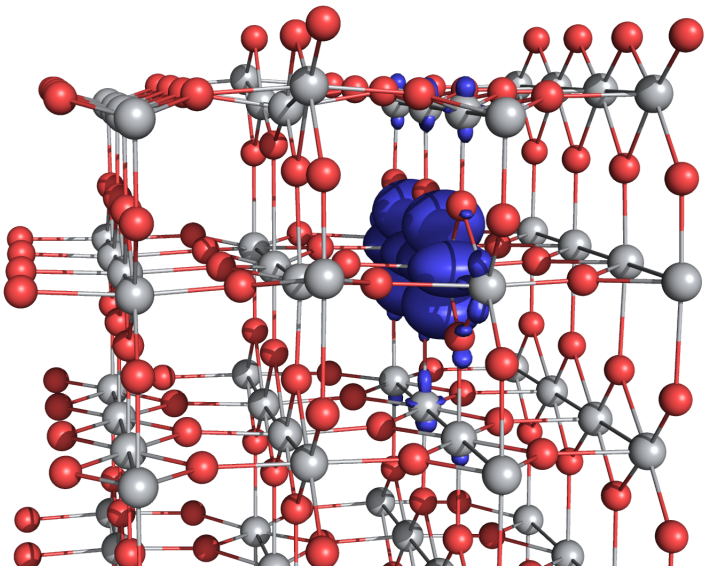

Fig. 4.2: *Shown is the spin density of two polarons (blue). The oxygen vacancy on top of the TiO_2 (110) surface causes symmetry breaking and hence polaron localization.[75] Isosurface level 0.05 eÅ^{-3}*

5 Publications

As this thesis is publication based, this chapter should give an overview of the relevant publications made during the PhD period. It also contains an overview of the detailed contributions of each individual author. The corresponding original articles and supporting information are included in the appendix of this work.

5.1 Intricacies of DFT+U, Not Only in a Numeric Atom Centered Orbital Framework

Matthias Kick, Karsten Reuter and Harald Oberhofer.
J. Chem. Theory. Comput. 15, 1705-1718 (2019).
DOI:10.1021/acs.jctc.8b01211

5.1.1 Content

This work forms the basis of all scientific papers who follow after it. In this work we present the details of our DFT+U infrastructure in FHI-aims. As already outlined in chapter 3 we give information about how the Hubbard projectors are defined in our implementation. In detail atomic basis functions or linear combinations of different basis functions can serve as Hubbard projectors which then determine the occupation matrix. We demonstrate the capability of our implementation by showing its ability to improve the description of the band gap in a NiO test system. Furthermore, we found that having a multiple set of polarization functions which belong to the same angular momentum channel can lead to wrong prediction of ground state properties. This is easily explained as if the +U correction is only applied to a subset of e.g. 3*d* basis functions, only this subset is subject to the penalty imposed by the correction term. In critical cases the electrons then tend to occupy other basis functions. These basis functions are often not as localized as the ones which are subject to the Hubbard correction. As a result, one ends up with changing the character of the localized states entirely. Therefore, building up the Hubbard projectors as a linear combination of all basis functions with same angular momentum is an elegant remedy to this problem.

We move on to a more stringent test case, the description of polarons at the Rutile TiO_2 (110) surface. In general, polarons can localize at various Ti atoms throughout the simulation cell. The fact that these various different localization patterns show only a little difference in their relative energies renders sampling a challenging task. However, by making use of the matrix control approach we are able find an elegant and efficient way to account for all relevant patterns. Comparing our results with other DFT related polaron studies, we find differences regarding the energetic ordering of the different possible localization patterns. By excluding other possibilities for these differences compared to other published results, we concluded that the use of pseudopotentials in other codes is the main source for these discrepancies. Within a pseudopotential code the core electrons are only approximated while FHI-aims is a full electron code. Furthermore, pseudopotentials are often constructed from a LDA or GGA reference. Yet, up to now it is unclear if this adds some error when used in DFT+U or hybrid DFT calculations.

Moreover, we investigate in detail how differently shaped Hubbard projectors influence the description of the polaronic states. Not surprisingly more diffuse functions lead to less localized states, however, this can be partly compensated by applying higher U values. This adds another ambiguity why in general U values are not comparable between different implementation of DFT+U

5.1.2 Individual Contributions

The idea to include DFT+U was already part of my master thesis. However, at the beginning of my PhD we discovered several problems regarding the basis set of FHI-aims which made a complete

rewrite of all the DFT+U infrastructure necessary. Harald Oberhofer was supervising the entire project and helped discussing the relevant working equations for the DFT+U implementation. He was also co-editing the manuscript. A significant part in editing the manuscript was also done by Karsten Reuter.

All implementation work and deriving the relevant working equations was done by me. I also performed all the necessary DFT+U and HSE06 simulations for all systems which are described in the publication. Finally, I also wrote the manuscript and created all figures using the matplotlib [102] and the PyMOL package [103].

5.2 Towards a Transferable Design of Solid-state Embedding Models on the Example of a Rutile TiO_2 (110) Surface

Matthias Kick and Harald Oberhofer.
J. Chem. Phys. 151, 184114 (2019).
DOI:10.1063/1.5125204

5.2.1 Content

For studying chemical reactions on non-metallic surfaces, there are in principle two different approaches one could choose in order to model the system in question. Within the slab approach one applies periodic boundary conditions (PBC) to account for all long range electrostatic effects. This is already achieved with the smallest possible repeating unit cell of the material, however, the PBC approach can suffer from so called finite-size effects.[104] In that case non-periodicities, such as defects or adsorbates, show spurious interaction with their own periodic images. Even worse, if localized charge carriers such as polarons are involved which makes it often necessary to use large unit cells in order to avoid unphysical interactions. This need of having large supercell sizes strongly limits the use of higher-rung functional techniques or even the use of wavefunctions methods. A PBC approach in that case is simply not tractable even with the use of modern computer hardware. A fact which is quite critical as the chemically most interesting materials often demand the use of more accurate methods beyond standard semi-local DFT.[105, 106]

A method to overcome these drawbacks is to use so called embedded cluster models. Within this approach a finite quantum-mechanically treated cluster is embedded into a point charge environment in order to capture the long range electrostatic interactions of a possible infinite crystal. By construction, such a model system does not suffer from spurious interactions as the slab approach does by imposing periodic boundary conditions.[107, 108] Usually, by applying an embedded cluster approach one needs to be careful regarding the choice of the cluster shape. The clusters stoichiometry has to be aligned with that of the underlying material which otherwise could lead to spurious charging of the entire system. Moreover, especially in ionic systems, the cluster should be symmetric to avoid low order multipole moments distorting the potential of the model.[25]

Confronted with these problems, this work critically addresses the accuracy of an embedded cluster approach w.r.t. to the applied cluster model shape and its size. We demonstrate that binding energies are in general quite robust regarding the chosen cluster model as they might benefit from a possible error cancellation. However, going to a more sensitive test case e.g. polaron formation at the TiO_2 (110) surface, we can show that the correct description of the ground state can be critically influenced by the shape of the cluster model. Based on our findings, we derive criteria for judging the quality of a certain cluster shape w.r.t. its ability in describing the system in question as accurately as possible. Moreover, we present a general design rule for cluster models allowing cluster model construction beyond trial and error. Overall, this work lines up with the previously mentioned publication on the implementation of DFT+U within FHI-aims by showing a detailed and systematic way to address the problem of polaron formation with DFT+U in a solid state embedding environment.

5.2.2 Individual Contributions

The idea to test the embedded cluster approach w.r.t. to its capabilities in describing polaron formation accurately arose during the work on the implementation of DFT+U. Right at the beginning we discovered that correct modeling of the ground state is not possible with the cluster models given by literature so far. A closer investigation using our own designed cluster models revealed that the shape of a cluster can critically influence its performance. Harald Oberhofer was supervising the entire project and was also co-editing the manuscript.

All tested cluster models, if not otherwise noted, have been created by me. I also performed all relevant calculations for all systems which are part of the publication. I wrote the manuscript and created all figures using the matplotlib [102] and the PyMOL package[103].

5.3 Mobile Small Polarons Explain Conductivity in Lithium Titanium Oxide Battery Electrodes

Matthias Kick, Cristina Grosu, Markus Schuderer, Christoph Scheurer and Harald Oberhofer.
Published on arXiv.org (2020).[1]
arXiv:2001.00263

5.3.1 Content

Not even since the Nobel Price in chemistry of 2019, which was awarded to three Li-ion battery researchers, it is clear Li-ion battery technology will play a major role in reducing the production of greenhouse gases in the mobility sector. However, up to now, battery capacities are still too low to provide a promising and competitive alternative to fossil fuel based engine technologies and thus electrically powered vehicles are still rare on the streets. Improving batteries is not only connected to improving their overall capacity but it also closely related to lowering the time which is required in order to charge the batteries. Moreover, in order to prevent capacity loss over the lifetime of a battery increasing their stability regarding charging and discharging is another desired goal. A promising material envisioned as a potential remedy for these problems is lithium titanium oxide (LTO). Zero strain insertion, high cycling stability and a stable charge/discharge plateau renders LTO an excellent anode material for long living batteries. However, its problem lies in its very low intrinsic electronic conductivity which limits its use. One way to overcome this drawback is to introduce oxygen vacancies resulting in significant improvement in electronic conductivity and Li-ion mobility. Yet up to now, the detailed mechanism causing this improvement is not fully understood. First experimental results indicate the formation of Ti^{3+} centers in an analogous way as observed for TiO_2.[30–33, 74] Apparently, Ti ions in LTO show a similar chemical environment as in TiO_2 with highly mobile polarons [109] which also cause a significant improvement in the electronic conductivity of TiO_2.

In this work we try to shed more light on the origin of the increased electronic conductivity. In detail we investigate if a possible polaron hopping mechanism is also responsible for the larger electronic conductivity. Indeed our results indicate that Ti^{3+} centers are the results of small polaron formation. Moreover, by calculating explicitly polaron hopping barriers in LTO we have been able to gauge their mobility. The obtained barrier heights show that already at room temperature the electrons are able to overcome the kinetic barrier strongly indicating that indeed a polaron hopping mechanism is the origin of the observed increase in electronic conductivity. In addition, by using a simple transition rate theory approach we have been able to calculate an upper bound for the value of electronic conductivity in blue LTO. Indeed, the electronic conductivity is several magnitudes above the ionic conductivity in LTO. This implies that it is theoretically possible to increase the electronic conductivity of LTO in such a way that it is not the limiting factor anymore regarding the overall conductivity of LTO.

Overall this work can be considered as a first step towards a deeper understanding of electron dynamics in LTO. Moreover, a deep understanding of these dynamics also regarding their interplay between Li-ion mobility could lead to development of further more advanced battery materials.

[1] By the end of this PhD thesis this paper has not yet been published in a peer reviewed journal. arXiv.org is an open access platform for pre prints of scientific papers.

5.3.2 Individual Contributions

Originally the idea arose during a discussion with Cristina Grosu about their attempts to synthesize blue colored LTO. The blue color of LTO is a result of the presence of oxygen vacancies similar to reduced TiO_2 which shows under the presence of oxygen vacancies the same blue color. First theoretical test simulations then immediately indicated the presence of small polarons.

The original idea came from Cristina Grosu and me. The pristine LTO bulk structures have been provided by Markus Schuderer. All further DFT+U related calculations have been performed by me. I also did all necessary modifications to the FHI-aims code. I wrote the manuscript and created the figures. Harald Oberhofer was supervising the entire project, was also co-editing the manuscript and helped creating the figures. Christoph Scheurer and Cristina Grosu also helped editing the manuscript. Christoph Scheurer was also the main advisor regarding the battery field.

6 Summary, Conclusions and Outlook

Central to this thesis is the DFT+U approach. Clearly its strength lies in its high efficiency. As demonstrated within this work, applying DFT+U causes only little computational overhead compared to standard LDA or GGA. Not only shown within this work but also in literature, its accuracy in describing polarons in transition metal oxides is definitely comparable with hybrid DFT approaches. Overall, its ability to cure, at least partly, for the SIE at a very little computational cost renders this method a very powerful workhorse addressing extended systems. However, as critically addressed during this work, the choice of the Hubbard U parameter and especially the choice of projector functions can critically influence the prediction of ground state properties. This might not be the case for rather robust systems such as bulk NiO, but more sensitive systems—such as polarons—can definitely suffer from a bad choice of input parameters. This is even more critical to see as the standard user is usually not aware of the pitfalls of this method. At a first glance, DFT+U working equations are easy to read but their effect on the electronic structure is not immediately clear. Written and derived for localized orbitals but usually implemented to act on basis functions, the effect on the localized states and on hybridization with surrounding orbitals is by far not trivial to see. This can be understood as the localized states are usually always a linear combination of all basis functions in the system, hence, applying the Hubbard correction just to a subset of these orbitals can lead (in the worst case) to a complete altering of the underlying electronic structure. In other words, as long as the localized states are mainly dominated by the subset of basis functions, DFT+U can be an excellent method to describe such a system. This is exactly the case for polarons occupying a 3*d* orbital on a transition metal atom. The polaron state shows almost pure 3*d* character. As demonstrated, this fact renders these kind of systems to an excellent test case for any kind of DFT+U implementation. In detail within our paper [21]—published in *The Journal of Chemical Theory and Computation*—we addressed the above mentioned pitfalls of DFT+U in the context of a localized orbital basis set. Critically, for the correct description of a polaron system are the applied Hubbard projectors. As we could show, altering the shape of the projector functions leads to different ground state predictions which can only be partly compensated by changing the U value. As a consequence, results between different DFT+U implementations are even less comparable. Even worse, as the amount of localization of the electrons is controlled by both the U value and the projector function shape, a too diffuse projector functions results overall in too delocalized polaronic states.

As it turns out, due to their sensitivity regarding the description of the electronic structure, polaronic states are also a quite useful test system for checking the accuracy of a solid state QM/MM embedding scheme. As we could demonstrate in the corresponding publication [110] within *The Journal of Chemical Physics*, the accuracy of such an approach does not only depend on how the different regions are connected but also on the employed shape of the QM-region. A fact which was not addressed so far in literature. By investigating several QM-region geometries differing in their size and shape we could derive simple guidelines for designing such QM clusters. Not only the density of states but also the shape of the frontier orbitals have to match with the periodic reference calculations. This in general enables to design QM-regions beyond the usual

trial and error approach.

Moving away from method development work to a more application-oriented research field we further used DFT+U to firstly describe the formation of polarons in LTO—a candidate for being an anode material in future solid state batteries.[30–33] Furthermore, by using the matrix control approach we have been able to gauge the polaron mobility. In fact, it turns out that a polaron hopping mechanism might be responsible for the experimentally observed increase in electronic conductivity if LTO was exposed to a reductive hydrogen atmosphere. Polaron hopping barrier heights are small enough for hopping to occur already at room temperature. Further, by using a simple transition state theory we are able to calculate an upper bound for the electronic conductivity in LTO. By this we can show that in principle it is possible—by e.g. defect engineering—to increase the electronic conductivity to be several magnitudes higher as LTO's ionic conductivity. An important fact if one considers that the overall conductivity of LTO is by this not longer limited by electron transport properties.

Acknowledgments / Danksagung

First of all, I would like to thank Prof. Karsten Reuter for giving me the opportunity to perform my PhD thesis in his group. For all the freedom I had to perform my research and for the unconditional support throughout the years.

Very special thanks also goes to Mitch and David. They not only have been great office mates but also dedicated members of our PhD self-help group. Without them I could never ever have mastered the dark arts of IT administration. Especially the weeks of setting up the local cluster with David have been a quite thrilling adventure. At that point I also would like to thank Cristina the most German Italian I ever met. She was also member of the self-help group and she taught me everything I needed to know about batteries.

Thank you Hendrik for the pumping iron experiences. It was always fun if you showed up in my office.

A big thanks also goes to my Captain Dr. Christoph Schober and to Dr. Simon Rittmeyer.

Also Dr. Christoph Scheurer deserves a big thank you, especially for his patience with me being IT admin.

I would like to thank Julia for the entire time since school. For her being patient with me, for the coffee breaks, for the beer, her open ears and for her efforts in keeping me away from insanity.

Further thanks goes to Dr. Daniel Berger for his great advise regarding *FHI-aims* and for his great assistance, not only for this thesis, but also for all of my project works during the last years. He was of more than only great support.

A very very special thanks goes to Harald. He was not only my direct supervisor he also became a close friend during my time being a PhD student. I guess Harald is the best supervisor one could have. Or in Klingon: *ghoS tIn qatlho' harald. Dev jup 'ej. ghaH nIvbogh DevwI'*

Also Ruth for sure deserves a quite big thank you. In addition I also would like to thank the first level support Christian an Xhristoph.

Last but not least, I would like to thank my parents for all their support ... and money :D.

Munich, May 18, 2020

Bibliography

[1] A. Janotti, J. B. Varley, P. Rinke, N. Umezawa, G. Kresse, and C. G. Van de Walle, Phys. Rev. B **81**, 085212 (2010) (cit. on p. 1).

[2] C. Di Valentin, G. Pacchioni, and A. Selloni, Phys. Rev. Lett. **97**, 166803 (2006) (cit. on p. 1).

[3] B. Magyari-Köpe, S. Park, H. Lee, and Y. Nishi, English, J. Mater. Sci. **47**, 7498 (2012) (cit. on p. 1).

[4] H. Sato, K. Ono, T. Sasaki, and A. Yamagishi, J. Phys. Chem. B **107**, 9824 (2003) (cit. on p. 1).

[5] C. Lun Pang, R. Lindsay, and G. Thornton, Chem. Soc. Rev. **37**, 2328 (2008) (cit. on p. 1).

[6] W. E. Pickett, S. C. Erwin, and E. C. Ethridge, Phys. Rev. B **58**, 1201 (1998) (cit. on p. 1).

[7] G. Pacchioni, J. Chem. Phys. **128**, 182505, 182505 (2008) (cit. on pp. 1, 4).

[8] E. Finazzi, C. Di Valentin, G. Pacchioni, and A. Selloni, J. Chem. Phys. **129**, 154113 (2008) (cit. on pp. 1, 4).

[9] J. T. Pegg, X. Aparicio-Anglès, M. Storr, and N. H. de Leeuw, J. Nucl. Mater. **492**, 269 (2017) (cit. on pp. 1, 4, 9).

[10] B. Dorado, B. Amadon, M. Freyss, and M. Bertolus, Phys. Rev. B **79**, 235125 (2009) (cit. on pp. 1, 14).

[11] B. Himmetoglu, A. Floris, S. de Gironcoli, and M. Cococcioni, Int. J. Quantum Chem. **114**, 14 (2014) (cit. on pp. 1, 4, 6–13).

[12] A. J. Cohen, P. Mori-Sánchez, and W. Yang, Chem. Rev. **112**, 289 (2011) (cit. on pp. 1, 4, 5).

[13] J. E. Moussa, P. A. Schultz, and J. R. Chelikowsky, J. Chem. Phys **136**, 204117, 204117 (2012) (cit. on pp. 1, 6).

[14] C. Adamo and V. Barone, J. Chem. Phys. **110**, 6158 (1999) (cit. on pp. 1, 6).

[15] V. Anisimov, J. Zaanen, and O. K. Andersen, Phys. Rev. B **44**, 943 (1991) (cit. on pp. 1, 7).

[16] A. I. Liechtenstein, V. I. Anisimov, and J. Zaanen, Phys. Rev. B **52**, R5467 (1995) (cit. on pp. 1, 8).

[17] S. L. Dudarev, G. A. Botton, S. Y. Savrasov, C. J. Humphreys, and A. P. Sutton, Phys. Rev. B **57**, 1505 (1998) (cit. on pp. 1, 9).

[18] J. Hubbard, Proc. R. Soc. A **276**, 238 (1963) (cit. on pp. 1, 6, 7).

[19] V. Blum, R. Gehrke, F. Hanke, P. Havu, V. Havu, X. Ren, K. Reuter, and M. Scheffler, Comput. Phys. Commun. **180**, 2175 (2009) (cit. on pp. 2, 12, 17).

[20] J. T. Devreese, "Polarons," in *Digital encyclopedia of applied physics* (American Cancer Society, 2003) (cit. on pp. 2, 23, 24).

[21] M. Kick, K. Reuter, and H. Oberhofer, J. Chem. Theor. Comput. **15**, 1705 (2019) (cit. on pp. 2, 12, 18, 24, 35).

[22] R. LeSar, *Introduction to computational materials science: fundamentals to applications* (Cambridge University Press, 2013) (cit. on p. 2).

[23] S. Lany and A. Zunger, Model. Simul. Mater. Sci. Eng. **17**, 084002 (2009) (cit. on p. 2).

[24] G. Makov and M. C. Payne, Phys. Rev. B **51**, 4014 (1995) (cit. on p. 2).

[25] N. Bernstein, J. R. Kermode, and G. Csányi, Rep. Prog. Phys. **72**, 026501 (2009) (cit. on pp. 2, 31).

[26] C. S. Ammal and A. Heyden, J. Chem. Phys. **133**, 164703 (2010) (cit. on p. 2).

[27] G. Pacchioni, in *Oxide surfaces*, Vol. 9, edited by D. Woodruff, The Chemical Physics of Solid Surfaces (Elsevier, 2001), pp. 94–135 (cit. on p. 2).

[28] S. Grimme and M. Steinmetz, Phys. Chem. Phys. **18**, 20926 (2016) (cit. on p. 2).

[29] D. Berger, A. J. Logsdail, H. Oberhofer, M. R. Farrow, C. R. A. Catlow, P. Sherwood, A. A. Sokol, V. Blum, and K. Reuter, J. Chem. Phys. **141**, 024105, 024105 (2014) (cit. on p. 2).

[30] P. Jakes, J. Granwehr, H. Kungl, and E. Rüdiger-A, Z. Phys. Chem. **229**, 1439 (2015) (cit. on pp. 2, 33, 36).

[31] J. Qiu, C. Lai, E. Gray, S. Li, S. Qiu, E. Strounina, C. Sun, H. Zhao, and S. Zhang, J. Mater. Chem. A **2**, 6353 (2014) (cit. on pp. 2, 33, 36).

[32] B. Yan, M. Li, X. Li, Z. Bai, J. Yang, D. Xiong, and D. Li, J. Mater. Chem. A **3**, 11773 (2015) (cit. on pp. 2, 33, 36).

[33] H. Kaftelen, M. Tuncer, S. Tu, S. Repp, H. Göçmez, R. Thomann, S. Weber, and E. Erdem, J. Mater. Chem. A **1**, 9973 (2013) (cit. on pp. 2, 33, 36).

[34] P. Hohenberg and W. Kohn, Phys. Rev. **136**, B864 (1964) (cit. on pp. 3, 5).

[35] W. Kohn and L. J. Sham, Phys. Rev. **140**, A1133 (1965) (cit. on p. 3).

[36] J. FRENKEL, Nature **125**, 235 (1930) (cit. on p. 4).

[37] R. Stowasser and R. Hoffmann, J. Am. Chem. Soc. **121**, 3414 (1999) (cit. on p. 4).

[38] P. Mori-Sánchez, A. J. Cohen, and W. Yang, J. Chem. Phys. **125**, 201102 (2006) (cit. on p. 4).

[39] P. Mori-Sánchez and A. J. Cohen, Phys. Chem. Chem. Phys. **16**, 14378 (2014) (cit. on pp. 4, 5, 9).

[40] J. L. Bao, L. Gagliardi, and D. G. Truhlar, J. Phys. Chem. Lett. **9**, 2353 (2018) (cit. on pp. 4, 5).

[41] B. Dorado, G. Jomard, M. Freyss, and M. Bertolus, Phys. Rev. B **82**, 035114, 035114 (2010) (cit. on pp. 4, 14).

[42] M. A. Mosquera and A. Wasserman, Mol. Phys. **112**, 2997 (2014) (cit. on p. 4).

[43] J. P. Perdew and A. Zunger, Phys. Rev. B **23**, 5048 (1981) (cit. on pp. 4, 5).

[44] G. E. Scuseria and V. N. Staroverov, in *Theory and applications of computational chemistry*, edited by C. E. Dykstra, G. Frenking, K. S. Kim, and G. E. Scuseria (Elsevier, Amsterdam, 2005), pp. 669–724 (cit. on p. 5).

[45] F. Jensen, *Introduction to computational chemistry* (John Wiley & Sons, 2006) (cit. on p. 5).

[46] Y. Zhang and W. Yang, J. Chem. Phys. **109**, 2604 (1998) (cit. on p. 5).

[47] I. Ciofini, C. Adamo, and H. Chermette, Chem. Phys. **309**, 67 (2005) (cit. on p. 5).

[48] J. P. Perdew, K. Burke, and M. Ernzerhof, Phys. Rev. Lett. **77**, 3865 (1996) (cit. on pp. 5, 21).

[49] M. Lundberg and P. E. M. Siegbahn, J. Chem. Phys. **122**, 224103 (2005) (cit. on p. 5).

[50] F. Wu and Y. Ping, J. Mater. Chem. A **6**, 20025 (2018) (cit. on pp. 5, 24).

[51] L. Goerigk, A. Hansen, C. Bauer, S. Ehrlich, A. Najibi, and S. Grimme, Phys. Chem. Chem. Phys. **19**, 32184 (2017) (cit. on p. 5).

[52] B. G. Johnson, C. A. Gonzales, P. M. Gill, and J. A. Pople, Chem. Phys. lett. **221**, 100 (1994) (cit. on p. 5).

[53] D.-y. Kao, K. Withanage, T. Hahn, J. Batool, J. Kortus, and K. Jackson, J. Chem. Phys. **147**, 164107 (2017) (cit. on pp. 5, 6).

[54] C. Shahi, P. Bhattarai, K. Wagle, B. Santra, S. Schwalbe, T. Hahn, J. Kortus, K. A. Jackson, J. E. Peralta, K. Trepte, S. Lehtola, N. K. Nepal, H. Myneni, B. Neupane, S. Adhikari, A. Ruzsinszky, Y. Yamamoto, T. Baruah, R. R. Zope, and J. P. Perdew, J. Chem. Phys. **150**, 174102 (2019) (cit. on p. 5).

[55] O. A. Vydrov and G. E. Scuseria, J. Chem. Phys. **121**, 8187 (2004) (cit. on p. 6).

[56] M. R. Pederson, A. Ruzsinszky, and J. P. Perdew, J. Chem. Phys. **140**, 121103 (2014) (cit. on p. 6).

[57] Z.-h. Yang, M. R. Pederson, and J. P. Perdew, Phys. Rev. A **95**, 052505 (2017) (cit. on p. 6).

[58] S. Schwalbe, T. Hahn, S. Liebing, K. Trepte, and J. Kortus, J. Comp. Chem. **39**, 2463 (2018) (cit. on p. 6).

[59] M. Marsman, J. Paier, A. Stroppa, and G. Kresse, J. Phys. Condens. Matter **20**, 64201 (2008) (cit. on p. 6).

[60] A. D. Becke, J. Chem. Phys. **88**, 2547 (1988) (cit. on pp. 6, 17).

[61] C. Lee, W. Yang, and R. G. Parr, Phys. Rev. B **37**, 785 (1988) (cit. on p. 6).

[62] D. D. O'Regan, N. D. M. Hine, M. C. Payne, and A. A. Mostofi, Phys. Rev. B **82**, 081102 (2010) (cit. on pp. 6, 12).

[63] Q. Wu and T. Van Voorhis, Phys. Rev. A **72**, 024502 (2005) (cit. on pp. 6, 10).

[64] B. Kaduk, T. Kowalczyk, and T. Van Voorhis, Chem. Rev. **112**, 321 (2012) (cit. on p. 6).

[65] J. Behler, B. Delley, K. Reuter, and M. Scheffler, Phys. Rev. B **75**, 115409 (2007) (cit. on p. 6).

[66] J. C. Slater and G. F. Koster, Phys. Rev. **94**, 1498 (1954) (cit. on p. 7).

[67] C. M. Goringe, D. R. Bowler, and E. Hernández, Rep. Prog. Phys **60**, 1447 (1997) (cit. on p. 7).

[68] F. H. L. Essler, H. Frahm, F. Göhmann, A. Klümper, and V. E. Korepin, *The one-dimensional hubbard model* (Cambridge University Press, 2005) (cit. on p. 7).

[69] S. A. Tolba, K. M. Gameel, B. A. Ali, H. A. Almossalami, and N. K. Allam, in *Density functional calculations*, edited by G. Yang (IntechOpen, Rijeka, 2018) Chap. 1 (cit. on p. 7).

[70] A. G. Petukhov, I. I. Mazin, L. Chioncel, and A. I. Lichtenstein, Phys. Rev. B **67**, 153106 (2003) (cit. on pp. 7, 11, 12, 20).

[71] K. P. O'Donnell and V. Dierolf, *Rare-Earth Doped III-Nitrides for Optoelectronic and Spintronic Applications*, Topics in Applied Physics (Springer Netherlands, 2010) (cit. on p. 7).

[72] V. Ivády, R. Armiento, K. Szász, E. Janzén, A. Gali, and I. A. Abrikosov, Phys. Rev. B **90**, 035146 (2014) (cit. on p. 9).

[73] J. P. Perdew, R. G. Parr, M. Levy, and J. L. Balduz, Phys. Rev. Lett. **49**, 1691 (1982) (cit. on p. 9).

[74] N. A. Deskins, R. Rousseau, and M. Dupuis, J. Phys. Chem. C **115**, 7562 (2011) (cit. on pp. 9, 24, 33).

[75] T. Shibuya, K. Yasuoka, S. Mirbt, and B. Sanyal, J. Phys. Condens. Matter **24**, 435504 (2012) (cit. on pp. 9, 15, 24, 25).

[76] Z. Wang, C. Brock, A. Matt, and K. H. Bevan, Phys. Rev. B **96**, 125150 (2017) (cit. on p. 9).

[77] M. Forti, P. Alonso, P. Gargano, and G. Rubiolo, Proc. Mater. Sci. **1**, 230 (2012) (cit. on p. 9).

[78] M. Cococcioni and S. de Gironcoli, Phys. Rev. B **71**, 035105 (2005) (cit. on p. 10).

[79] G. Moynihan, G. Teobaldi, and D. D. O'Regan, Phys. Rev. B **94**, 220104 (2016) (cit. on p. 10).

[80] R. S. Mulliken, J. Chem. Phys. **23**, 1833 (1955) (cit. on pp. 12, 13).

[81] P. Löwdin, J. Chem. Phys. **18**, 365 (1950) (cit. on p. 12).

[82] M. J. Han, T. Ozaki, and J. Yu, Phys. Rev. B **73**, 045110 (2006) (cit. on pp. 13, 14, 18, 20).

[83] D. D. O'Regan, M. C. Payne, and A. A. Mostofi, Phys. Rev. B **83**, 245124 (2011) (cit. on pp. 13, 14, 20).

[84] H. Eschrig, K. Koepernik, and I. Chaplygin, J. Solid State Chem. **176**, 482 (2003) (cit. on p. 13).

[85] C. Tablero, J. Phys. Condens. Matter **20**, 325205 (2008) (cit. on pp. 14, 20).

[86] J. P. Allen and G. W. Watson, Phys. Chem. Chem. Phys. **16**, 21016 (2014) (cit. on p. 14).

[87] V. Havu, V. Blum, P. Havu, and M. Scheffler, J. Comput. Phys. **228**, 8367 (2009) (cit. on p. 17).

[88] B. Delley, J. Chem. Phys. **92**, 508 (1990) (cit. on p. 17).

[89] O. Lamiel-Garcia, K. C. Ko, J. Y. Lee, S. T. Bromley, and F. Illas, J. Chem. Theor. Comput. **13**, 1785 (2017) (cit. on p. 17).

[90] J. Hutter, M. Iannuzzi, F. Schiffmann, and J. VandeVondele, WIREs Computat Mol Sci **4**, 15 (2014) (cit. on p. 18).

[91] H. Jiang, R. I. Gomez-Abal, P. Rinke, and M. Scheffler, Phys. Rev. B **82**, 045108 (2010) (cit. on p. 20).

[92] S. Y. Park and H. J. Choi, Phys. Rev. B **80**, 155122 (2009) (cit. on p. 20).

[93] N. F. Mott, Proceedings of the Physical Society. Section A **62**, 416 (1949) (cit. on p. 20).

[94] O. Bengone, M. Alouani, P. Blöchl, and J. Hugel, Phys. Rev. B **62**, 16392 (2000) (cit. on p. 20).

[95] G. A. Sawatzky and J. W. Allen, Phys. Rev. Lett. **53**, 2339 (1984) (cit. on p. 20).

[96] J. Devreese, A. S. I. on Fröhlich Polarons, and E. P. I. in Polar Semiconductors, *Polarons in ionic crystals and polar semiconductors*, NATO Advanced Study Institutes Series (North-Holland Publishing Company, 1972) (cit. on p. 24).

[97] H. Jónsson, G. Mills, and K. W. Jacobsen, *Nudged elastic band method for finding minimum energy paths of transitions*, 385 (cit. on p. 24).

[98] G. Henkelman, B. P. Uberuaga, and H. Jónsson, J. Chem. Phys. **113**, 9901 (2000) (cit. on p. 24).

[99] C. Di Valentin and A. Selloni, J. Phys. Chem. Lett. **17**, 2223 (2011) (cit. on p. 24).

[100] M. Reticcioli, I. Sokolovi ć, M. Schmid, U. Diebold, M. Setvin, and C. Franchini, Phys. Rev. Lett. **122**, 016805 (2019) (cit. on p. 24).

[101] S. Chrétien and H. Metiu, J. Phys. Chem. C **115**, 4696 (2011) (cit. on p. 24).

[102] J. D. Hunter, Comput. Sci. Eng. **9**, 90 (2007) (cit. on pp. 30, 32).

[103] Schrödinger, LLC, "The PyMOL molecular graphics system, version 1.8," Nov. 2015 (cit. on pp. 30, 32).

[104] C. W. M. Castleton, A. Höglund, and S. Mirbt, Model. Simul. Mater. Sci. Eng **17**, 084003 (2009) (cit. on p. 31).

[105] F. R. Manby, M. Stella, J. D. Goodpaster, and T. F. Miller III, J. Chem. Theory Comput. **8**, 2564 (2012) (cit. on p. 31).

[106] A. Kubas, D. Berger, H. Oberhofer, D. Maganas, K. Reuter, and F. Neese, J. Phys. Chem. Lett. **7**, 4207 (2016) (cit. on p. 31).

[107] P. Sherwood, A. H. de Vries, M. F. Guest, G. Schreckenbach, C. R. A. Catlow, S. A. French, A. A. Sokol, S. T. Bromley, W. Thiel, A. J. Turner, S. Billeter, F. Terstegen, S. Thiel, J. Kendrick, S. C. Rogers, J. Casci, M. Watson, F. King, E. Karlsen, M. Sjøvoll, A. Fahmi, A. Schäfer, and C. Lennartz, J. Mol. Struct. THEOCHEM **632**, 1 (2003) (cit. on p. 31).

[108] S. Metz, J. Kästner, A. A. Sokol, T. W. Keal, and P. Sherwood, Wiley Interdiscip. Rev. Comput. Mol. Sci. **4**, 101 (2014) (cit. on p. 31).

[109] M. Setvin, C. Franchini, X. Hao, M. Schmid, A. Janotti, M. Kaltak, C. G. Van de Walle, G. Kresse, and U. Diebold, Phys. Rev. Lett. **113**, 086402 (2014) (cit. on p. 33).

[110] M. Kick and H. Oberhofer, J. Chem. Phys. **151**, 184114 (2019) (cit. on p. 35).

Appendices

A Paper # 1

Intricacies of DFT+U, Not Only in a Numeric Atom Centered Orbital Framework

Matthias Kick, Karsten Reuter and Harald Oberhofer
J. Chem. Theory. Comput. 2019, 15, 1705-1718 (2019).
DOI:10.1021/acs.jctc.8b01211

Reprinted under the terms of American Chemical Society's Policy on Theses and Dissertations.
©2019 American Chemical Society

JCTC Journal of Chemical Theory and Computation

Article

Cite This: J. Chem. Theory Comput. 2019, 15, 1705−1718

pubs.acs.org/JCTC

Intricacies of DFT+U, Not Only in a Numeric Atom Centered Orbital Framework

Matthias Kick, Karsten Reuter, and Harald Oberhofer*

Chair for Theoretical Chemistry and Catalysis Research Center, Technical University of Munich, Lichtenbergstrasse 4, Garching 85747, Germany

ABSTRACT: We implemented the popular Hubbard density-functional theory + U (DFT+U) method in its spherically averaged form in the all-electron, full-potential DFT code FHI-aims. There, electronic states are expressed on a basis of highly localized numeric atomic orbitals (NAO), which straightforwardly lend themselves as projector functions for the DFT+U correction, yielding the necessary occupations of the correlated Hubbard subspace at no additional cost. We establish the efficacy of our implementation on the prototypical bulk NiO and obtain the well-known band gap opening effect of DFT+U. As a more stringent, real world test system, we then study polaron formation at the rutile TiO_2(110) surface, where our results are in line with both experimental data as well as hybrid functional calculations. At this TiO_2 test system, yet in the bulk, we analyze some of the intricacies of using the DFT+U correction in a localized, numeric atomic orbital basis set. Specifically, we find that multiple localized radial basis functions of the same angular momentum can lead to highly erroneous predictions of ground-state properties. We also demonstrate a number of remedies to this problem. Finally, we highlight the critical influence of the exact choice of projector functions on DFT+U results using a number of projector functions of different spatial extent and composed of linear combinations of NAO basis functions. All of our efforts serve to highlight that, contrary to its deceptive ease of use, the DFT+U is far from the "black-box" approach it is sometimes made out to be.

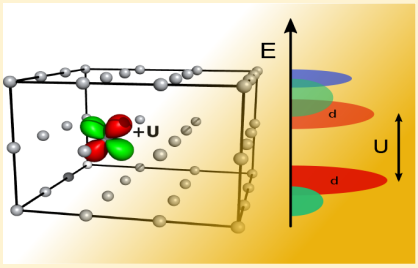

1. INTRODUCTION

Besides the tremendous success of local-density approximation (LDA)[1] or generalized-gradient approximation (GGA)[2] density-functional theory (DFT)[1,3] in describing metals or classical semiconductors,[4] corresponding standard Kohn−Sham DFT still lacks the ability of reliably describing systems characterized by localized electrons. Especially, transition metal oxides, lanthanoide or actinoide compounds with partially filled d- or f-shells, are often not described at a sufficient level of accuracy.[5−8] This failure can largely be attributed to the incomplete self-interaction error (SIE) cancellation inherent to these functional approximations, in general yielding an overestimation of Coulomb repulsion and therefore a bad description of localized electronic states.[9]

Prevalent routes to address this problem are hybrid functional DFT or the so-called Hubbard corrected DFT functional methods,[10,11] widely known as DFT+U. The latter adds a correction to the LDA or GGA Hamiltonian, which is inspired by the Hubbard model,[12] to cure parts of the SIE in these approximated DFT functionals. Although hybrid functional DFT calculations become increasingly affordable with current computer architectures, the great strength of DFT+U still lies in the simplicity of its corrective term and the concomitant low computational costs that are only marginally higher than standard LDA or GGA calculations. In addition, the +U correction is straightforwardly only applied to specific species. This renders DFT+U a most appealing tool to study larger systems or interfacial systems where only one of the component materials is not adequately described at the semilocal DFT level (e.g., metal/oxide interfaces). There are of course other, less approximate approaches to overcoming the SIE in DFT such as self-interaction corrected DFT (SIC-DFT).[13] However, suffering from high computational cost, this variant is not commonly used in the literature. On the other hand, recent developments in size extensive alternatives using Fermi−Löwdin orbitals (FLO-SIC) showed promising results, overcoming some of the pitfalls in DFT while at the same time being computational competitive.[14−17] In this work, though, we focus with the DFT+U method on the currently most widely used SIE correction schemes.

Here, we present a new implementation of the DFT+U method in the full-potential, all-electron, numeric atomic orbital (NAO)-based FHI-aims code. While currently +U corrections are widely available in most plane-wave DFT codes, all of these rely on some form of pseudopotential to describe core states. For most materials and chemical applications, pseudoization of core electrons does not noticeably influence the results. Yet, there are exceptions to this as we will show on the highly sensitive example of polaron localization in oxygen-deficient TiO_2. Furthermore, a localized basis set code like FHI-aims also allows the use of solid-state embedding techniques[18−20] to circumvent finite size effects when dealing with, for example, locally charged semiconductor surfaces, which is not easily achievable in standard plane-wave codes.

Received: December 3, 2018
Published: February 8, 2019

Downloaded via TU MUENCHEN on July 11, 2019 at 11:21:23 (UTC).
See https://pubs.acs.org/sharingguidelines for options on how to legitimately share published articles.

© 2019 American Chemical Society

DOI: 10.1021/acs.jctc.8b01211
J. Chem. Theory Comput. 2019, 15, 1705−1718

Unfortunately, a lot of studies found in the literature outside of the core circle of DFT+U developers tend to treat the method like a black-box approach, where only the *U* parameter needs to be determined, sometimes even simply taken from the literature. In this work, we will thoroughly demonstrate this not to be the case at all. Being an effective correction to some of the failings of semilocal DFT, the +U approach relies on so-called projector functions based on a set of reference states to determine to which electrons the correction applies. There is no unique way to determine such reference states; yet the literature shows that most localized orbitals of the correct angular momentum can be employed as references. Thus, the exact details of the projector functions vary between codes. As we will show in this work, this not only has a profound influence on the actual values of the *U* parameter to be applied (which by itself invalidates the simple use of literature *U* values possibly originating from other codes). Moreover, it can also, especially in systems with strong hybridization between frontier orbitals, lead to large deviations in the convergence behavior of the self-consistent field (SCF) cycle, and even to widely differing orbital characters.

This work is organized as follows. First, to set the stage for our implementation, we give a brief review of the theory and background of the DFT+U approach, where we especially emphasize the role of the projector functions and reference states. We then highlight implementation details specific to DFT+U in FHI-aims and discuss possible pitfalls due to the nature of the employed NAO basis. We demonstrate the efficacy of our implementation on a bulk NiO model system, which constitutes one of the standard tests of the DFT+U approach. As a much more exacting test-case, we next consider the relative stabilities of polaronic configurations pinned to an oxygen vacancy on a rutile TiO_2 (110) surface. Because of the relatively large amount of orbital hybridization in TiO_2 and the strong d-character of the polarons, these prove to be highly sensitive to both the choice of the *U* parameter as well as the nature of the projector function. Therefore, we end this work with a discussion of the influence of the projectors on the applicable values of *U*, the SCF convergence, and the nature of the resulting frontier orbitals, as well as the interaction of projector functions with an NAO basis.

2. THEORY

2.1. General DFT+U Background. The DFT+U approximation to (strongly) correlated electronic systems draws its inspiration from the Hubbard[12] and Anderson lattice models,[21] originally formulated to describe magnetic impurities within certain materials. Common to both models is the assumption that strongly localized d- and f-electrons are subject to an on-site electron−electron repulsion. Typically, the strength of this repulsion is determined by an effective parameter, the so-called Hubbard U.

Considering one of the most vexing failures of approximate density functionals, the description of localized electrons,[22] Anisimov et al.[10] suggested a Hubbard-like description of strongly correlated electronic states. The remaining electronic states, on the other hand, are considered to be satisfactorily treated on the level of standard, semilocal DFT functionals and thus left unaugmented. In the DFT+U nomenclature, the collection of states to which the correction is applied is often called the correlated or localized subspace. At first glance, simply treating a subset of electrons with an effective model may seem like a hard to justify, ad hoc interference with otherwise theoretically rigorous semilocal density functionals. Yet, modern interpretations of DFT+U showed the method to rest on much more solid theoretical foundations.[23]

Specifically, the failure of semilocal DFT to correctly render localized states can be traced back to an erroneous description of the total energy with respect to fractional changes to the number of electrons (or spins) in the system.[9] While the exact energy functional should show derivative discontinuities at integer numbers of electrons and piece-wise linear behavior in between, semilocal functionals are nonlinear and continuous. It can be shown[23,24] that the main improvement of augmented DFT+U functionals over standard, semilocal DFT is the introduction of a derivative discontinuity into the exchange-correlation (xc) potential. Regarding the band structure of nonmetallic solids, the effect of this correction is to restore the correct fundamental band gap of the material.[24] On top of that, DFT+U can also be regarded as the replacement of the mean-field density−density interactions with a Hartree−Fock (HF)-like Hamiltonian[25] for d- and f-like states, which are affected most strongly by the electron delocalization error. Such a replacement of parts of the DFT functional also forms the basis of the popular hybrid DFT functionals,[26,27] where a part of the orbital-dependent exact exchange from HF is added to the xc-functional. In this interpretation, DFT+U, in its simplest but most common formulation, replaces the computationally highly expensive nonlocal exchange integrals of hybrid functionals with just a single effective parameter, *U*. This greatly reduces the necessary computational effort, generally making DFT+U applicable to larger time and length-scale problems than hybrids. However, in contrast to hybrid DFT, the DFT+U correction only acts on the subset of states most strongly affected by the delocalization error. All other states, as well as interactions between them and DFT+U corrected states, are expected to be treated properly already on the semilocal level of DFT. Applying DFT+U to these states would therefore lead to an erroneous overcorrection.

The first task of a DFT+U implementation is thus to filter those states that need to be corrected, generally frontier d- or f-states, out of the whole spectrum of Kohn−Sham (KS) states. This is generally not straightforwardly possible, due to hybridization of orbitals and mixing of states. The correction thus needs to be applied to all KS-orbitals that contribute to the correlated frontier d- and f-states. Ideally, this correction should be proportional to the strengths of their contribution, that is, the coefficients or occupation numbers of the KS-orbitals in the correlated states. The problem of finding the right portion of the KS-spectrum to correct is thus analogous to the problem of finding the angular momentum character of an orbital or its contribution to the partial charge of an atom, and unfortunately equally ill-defined. As in the case of partial charge attribution, there are a number of approximations to count the contribution of a KS-orbital to a state, such as the method of Mulliken[28] or Löwdin population analysis.[29] In all cases, the contribution of a KS-orbital to a correlated state is ultimately determined by a projection of the orbital onto a reference representation of that state $|\Phi\rangle$, generally called the projector function. Thus, next to the choice of the correction strength parameter *U*, the projector functions are the most important factors determining the efficacy of any DFT+U implementation.

2.2. Projector Functions. Considering that the character of the correlated states may differ from system to system, each new system in principle demands a unique set of optimized

DOI: 10.1021/acs.jctc.8b01211
J. Chem. Theory Comput. 2019, 15, 1705−1718

projector functions. In practice, though, most DFT+U implementations commonly use a set of predefined, sometimes also called Hubbard, projector functions. These are generally specific to the respective elements but independent of the environment, to ensure transferable results.

Because of the effective nature of the DFT+U correction, it is not strictly necessary for the projector functions to mimic actual physical orbitals, both in shape and in number. Indeed, one of the main aims of this work is to study the effect of the choice of projector functions on observables calculated with DFT+U. Yet, given that the DFT+U correction demands a projection of the KS-orbitals $\{|\psi\rangle\}$ on the reference states $\{|\Phi\rangle\}$ at each iteration of the self-consistent field (SCF) cycle, the choice of projector function also greatly influences the computational efficiency of the implementation.

To avoid excessive computational overhead in determining the DFT+U contributions, it is thus convenient to define the projector functions as a superposition of basis functions of the underlying DFT code.[4,30] The necessary projections $\langle\psi|\Phi\rangle$ are then simply given by the respective basis function coefficients of $|\psi\rangle$ and, in the case of nonorthogonal basis functions, the basis set overlap matrix. As these are quantities already central to the plain DFT cycle, the only computational overhead associated with the DFT+U correction is thus the cost of determining the coefficients of the basis set expansion of the projector functions themselves. The popular choice of using projector functions based on maximally localized Wannier orbitals,[30] for example, would add the cost of determining the Wannier orbitals to each SCF step.

Another popular choice, especially in DFT codes based on localized basis functions, is therefore to directly use the basis functions, or predetermined combinations thereof, as projector functions, for a minimal computational overhead. To this end, we here introduce the projector functions for an atomic site I and of magnetic quantum number m and spin σ as an explicit linear combination of numeric atomic orbital (NAO) basis functions φ^{σ}_{Im} at this site and of this angular momentum and spin:

$$|\Phi^{\sigma}_{Im}\rangle = \sum_{p} c_{Imp}|\varphi^{\sigma}_{Imp}\rangle \tag{1a}$$

with c_{Imp} denoting the corresponding expansion coefficient and the index p labeling the different radial basis functions related to their specific angular momentum quantum number. Furthermore, we here also define for completeness the dual projector functions:

$$|\tilde{\Phi}^{\sigma}_{Im}\rangle = \sum_{p} c_{Imp}|\tilde{\varphi}^{\sigma}_{Imp}\rangle \tag{1b}$$

$$|\tilde{\varphi}^{\sigma}_{Imp}\rangle = \sum_{m',p'} S^{-1}_{Imp,m'p'}|\varphi^{\sigma}_{Im'p'}\rangle \tag{1c}$$

where $\mathbf{S}^{-1}$ is the inverse overlap matrix of the basis functions. The dual projector functions serve as an important notational short-cut to avoid having to carry the overlap matrix, used to orthogonalize the projections, through all necessary calculations.[28,31]

As compared to, for example, Gaussians, the NAO basis functions employed here have the advantage that they are DFT solutions of nonspin polarized free atoms[32] and can thus be expected to reflect the character of localized correlated states very well. Using a linear combination of NAOs additionally awards us a great flexibility in the choice of projector functions. In principle, we could use any function as long as they can be represented by the NAO basis functions present in the simulation cell. All basis functions thus included in the DFT+U correction span the correlated subspace and, in our implementation, are subjected to the same U parameter only modulated by their expansion coefficient c_{Imp}. Note that this stands, for instance, in contrast to Han et al.,[33] where basis functions can further be grouped into subshells with their own U values. While their approach allows more flexibility for the DFT+U correction and serves to avoid some of the problems due to multiple basis functions of the same angular momentum participating in the correction (cf., section 5.1), it may also limit comparability between systems. In our current approach, we thus decided against subshell grouping.

Finally, it should be noted that all basis functions in FHI-aims[32] are Gram−Schmid orthogonalized to all other basis functions on the same atom. This means that in our case the dual projector functions are actually identical to the direct projector functions.

2.3. Projection Operator and Occupation Matrix. The contribution of a given KS-orbital to the correlated subspace could simply be determined just by calculating the overlap of the orbital with each projector function, individually localized on each relevant atom. Yet, such an approach would neglect all direct contributions from neighboring atoms. As a remedy, and again in direct analogy to, for example, the Mulliken analysis, a number of different ways to combine the projector functions have been proposed in the literature,[4] as there is again no single general recipe.[24,33,34] Apart from the different projector functions, most of the differences between existing DFT+U implementations are due to these differences in the way the occupancies of the correlated subspace are calculated.

These differences are best discussed on the example of the occupation matrix $n^{\sigma}_{Imm'}$ at atomic site I and spin σ, which is the central quantity in the DFT+U correction to the Kohn−Sham Hamiltonian. The index m thereby enumerates the corresponding projector function, eq 1a. Mathematically, the DFT+U occupation matrix is expressed in terms of a local projection operator, $\hat{P}^{\sigma}_{Imm'}$.[34]

$$n^{\sigma}_{Imm'} = \sum_{\gamma} f_{\gamma}\langle\psi^{\sigma}_{\gamma}|\hat{P}^{\sigma}_{Imm'}|\psi^{\sigma}_{\gamma}\rangle \tag{2}$$

where f_{γ} represents the occupation of the γth Kohn−Sham (KS) state ψ^{σ}_{γ}.

Of the many possible choices for the projection operator, we restrict the discussion here to two of the most common ones, the so-called on-site and dual-representations:[33]

$$\hat{P}^{\sigma}_{Imm'}(\text{on-site}) = |\tilde{\Phi}^{\sigma}_{Im'}\rangle\langle\tilde{\Phi}^{\sigma}_{Im}| \tag{3a}$$

and

$$\hat{P}^{\sigma}_{Imm'}(\text{dual}) = \frac{1}{2}[|\tilde{\Phi}^{\sigma}_{Im'}\rangle\langle\Phi^{\sigma}_{Im}| + |\Phi^{\sigma}_{Im'}\rangle\langle\tilde{\Phi}^{\sigma}_{Im}|] \tag{3b}$$

respectively.

Both representations, if used in a DFT+U correction, were shown to successfully compensate for some of the shortcomings of semilocal DFT, widening band gaps and producing more localized states.[33,35] The significant difference between them is the treatment of the overlap of the projector functions with their surroundings. The dual approach, thereby, accounts for this overlap analogously to the popular Mulliken

DOI: 10.1021/acs.jctc.8b01211
J. Chem. Theory Comput. 2019, 15, 1705−1718

population analysis.[28] In contrast, the on-site representation only accounts for the overlaps within the localized subspace of the given site and neglects the overlaps to other atoms.

Because of this different treatment of overlaps, there is an even greater distinction between $\hat{P}^{\sigma}_{Imm'}$ (on-site) and $\hat{P}^{\sigma}_{Imm'}$ (dual). Considering that the occupation matrices essentially represent the density matrix of electrons contained in the correlated subspace, the trace of the occupation matrix should yield the number of electrons contained in the subspace, which is known as the sum rule. In ignoring the overlap with neighboring atoms, the on-site occupation matrix indeed does not fulfill the sum rule, while the dual representation does.[33,34] While this would seem like a clear argument for the dual representation, earlier detailed studies regarding the performance of the occupation matrices for various transition metal oxides showed no clear advantage of using one representation over the other.[35] This can be explained by the simple fact, that the miscounting of electrons in the on-site case is straightforwardly compensated by simply applying a different strength of the DFT+U correction using a different value of U. This is indeed another strong case against simply using published values of U, as they might not be transferable between different implementations using different representations of the occupation matrix.

Finally, putting all parts together, eqs 2, 3a, and 1a yield the following on-site occupation matrix:

$$n^{\sigma}_{Imm'} = \sum_{p,p'} c^{\sigma}_{Imp} c^{\sigma,*}_{Im'p'} \rho^{\sigma}_{Imp,Im'p'} \tag{4a}$$

where $\rho^{\sigma}_{Imp,Im'p'}$ denotes the contracted density matrix of the system, $\rho^{\sigma}_{Imp,Im'p'} = \langle \tilde{\varphi}^{\sigma}_{Imp} | \hat{\rho} | \tilde{\varphi}^{\sigma}_{Im'p'} \rangle$ with $\hat{\rho}$ being the density operator. Along the same lines, the dual occupation matrix can be simplified to

$$n^{\sigma}_{Imm'} = \frac{1}{2} \sum_{\alpha} \sum_{p,p'} c^{\sigma}_{Imp} c^{\sigma,*}_{Im'p'} [S_{\mathrm{Imp},\alpha} \rho^{\sigma}_{\alpha,\mathrm{Im}'p'} + \rho^{\sigma}_{\mathrm{Imp},\alpha} S_{\alpha,\mathrm{Im}'p'}] \tag{4b}$$

Here, α denotes a compound index over all NAO basis function at all sites, of all angular momenta and magnetic quantum numbers. It thus denotes a superspace to the correlated subspace, enumerated through the indices I,m, and p. $S_{Imp,\alpha}$ finally is a nonrectangular submatrix of the basis function overlap matrix.

2.4. DFT+U Energy Functional. The DFT+U occupation matrices (eq 4a) serve to determine how much each component of the NAO basis set representation of each KS-state contributes to the correlated states. On the basis of this, the DFT+U correction to the DFT energy functional can then be formulated as[10,36]

$$E_{\mathrm{DFT+U}}[\rho(\mathbf{r})] = E_{\mathrm{DFT}}[\rho(\mathbf{r})] + E^{0}_{\mathrm{U}}[\mathbf{n}_I] - E_{\mathrm{dc}}[\mathbf{n}_I] \tag{5}$$

where ρ denotes the electron density and E_{DFT} the density functional of choice. E_{U} represents the DFT+U energy correction derived from the Hubbard model, which depends only indirectly on the electron density via the occupation number matrix of a correlated state associated with a specific atom at site I.

Simply adding E^{0}_{U} to E_{DFT} would lead to a double-counting of Coulomb interaction, because all electron−electron interactions are already included in the standard DFT functional. Equation 5 therefore also contains a double-counting (DC) correction functional E_{dc}. This DC-functional can not be uniquely defined because the DFT energy is a functional of the charge density, while the Hubbard contribution depends explicitly on orbital occupations.[37] In any application of the DFT+U approach, E_{dc} therefore has to be approximated, with common choices being the around mean-field (AMF) and the fully localized limit (FLL).[24] In the AMF approximation, one assumes a uniform occupation of each orbital in the correlated subspace. In this limit, an energy penalty is imposed on fluctuations of occupations differing from their expected mean value. Within the FLL, on the other hand, one assumes that the occupations are either 0 or 1; that is, the electrons are fully represented by a subspace orbital or not at all.[38] Thus, FLL favors the integer occupation of localized states.[37] Therefore, one can consider FLL to be the adequate correction for systems with strongly localized electrons and AMF to be most suited for systems with quasi-homogeneous electron distribution across the whole correlated subspace.[24] A third alternative was later proposed by Pethukov et al.,[37] where E_{dc} is linearly interpolated between the limits of FLL and AMF. In our implementation, we consider all three choices. Yet, for the sake of brevity and without loss of generality, all further formulations, if not otherwise noted, are written in terms of the fully localized limit.

Following the de facto standard of all DFT+U applications, our implementation is based on the rotationally invariant, spherically averaged form of DFT+U, first proposed by Dudarev and co-workers.[11] In this simplified formulation, the effective DFT+U corrections are spherical averaged, justified by the fact that the localized correlated states largely retain atomic character and, hence, spherical symmetry. The respective DFT+U functional with FLL double-counting correction reads:

$$E^{\mathrm{FLL}}_{\mathrm{U}} = E^{0}_{\mathrm{U}} - E^{\mathrm{FLL}}_{\mathrm{dc}} = \frac{1}{2} \sum_{\sigma,I} U^{I} [Tr(\mathbf{n}^{\sigma}_{I}) - Tr(\mathbf{n}^{\sigma}_{I}\mathbf{n}^{\sigma}_{I})] \tag{6}$$

In this formulation, the strength of the DFT+U correction is controlled by the effective parameter U, which can, in principle, be chosen independently for each site I.

2.5. Effective Parameter *U*. Unfortunately, by virtue of it being an effective parameter, there is no unique way to determine the value of U.[24] Most commonly, the value of U is thus adjusted until some observable agrees with higher-rung DFT or experimental references. This value can then be used to make predictions on other material properties.[24,39] Next to this semiempirical approach, there also exist approaches to calculate the value from first principles. For example, in the linear response approach by Cococcioni et al.,[40] the DFT ground-state energy is calculated for a number of different electron occupations, and U is calculated from the spurious curvature of the total energy with respect to fractional occupations (recall the above-mentioned interpretation of DFT+U as a correction to restore piece-wise linearity of the energy functional).

Whichever way the U value is determined, all properties calculated with DFT+U sensitively depend on it. At the same time, the calculated or fitted value of U not only depends on the atoms included in the DFT+U correction, but also on their surroundings, the lattice parameters, and other physical properties.[24,39,41] Furthermore, it depends on the basis sets used to resolve the wave functions in the underlying DFT code and on the projection of the KS-states to determine the

DOI: 10.1021/acs.jctc.8b01211
J. Chem. Theory Comput. 2019, 15, 1705−1718

occupation numbers that enter the +U correction. All of these factors strongly limit the comparability of different U values between systems and DFT+U implementations. In general, for each new system and code, one should redetermine U.

2.6. DFT+U Hamiltonian and Effective Potential. Finally, for a self-consistent calculation of the DFT+U energy, it is necessary to derive the DFT+U correction Hamiltonian. This Hamiltonian enters the usual DFT routines as an additive matrix on top of the Kohn−Sham Hamiltonian matrix:

$$\mathbf{h}^{\sigma}_{\mathrm{DFT+U}} = \mathbf{h}^{\sigma}_{\mathrm{DFT}} + \mathbf{h}^{\sigma}_{\mathrm{U}} \tag{7}$$

The Hamiltonian correction matrix can be computed by taking the derivative of the energy (eq 6) with respect to the density matrix elements.[33]

$$\mathbf{h}^{\sigma}_{\mathrm{U}} = \frac{\partial E_{\mathrm{U}}}{\partial \rho^{\sigma}_{\alpha\alpha'}} \tag{8}$$

The exact form of the DFT+U Hamiltonian correction matrix thus again depends on the choice of projector representation. For the on-site representation, the correction matrix simply reads:

$$h^{\sigma}_{Imp,m'p'} = c^{\sigma}_{Imp} c^{\sigma,*}_{Im'p} v^{\sigma}_{Imm'} \tag{9a}$$

while the dual representation yields a more complicated Hamiltonian:

$$h^{\sigma}_{\alpha,\alpha'} = \frac{1}{2} \sum_{m,m'} \sum_{p,p'} c^{\sigma}_{Imp} c^{\sigma,*}_{Im'p} v^{\sigma}_{Imm'} [\delta_{\alpha,m'p} S_{mp,\alpha'} + S_{\alpha,m'p} \delta_{mp,\alpha}] \tag{9b}$$

Here, $v^{\sigma}_{Imm'} = -U_I\left(n^{\sigma}_{Imm'} - \frac{1}{2}\right)$ is the effective potential. It only depends on the definition of the double-counting correction. Both correction matrices here are given for the FLL limit of the double counting correction. For other limits, we refer the reader to ref 37.

3. IMPLEMENTATION DETAILS SPECIFIC TO FHI-AIMS

FHI-aims is an all-electron electronic structure code.[32] Its main focus lies on DFT; however, beyond-DFT methods such as second-order Møller−Plesset (MP2) perturbation theory, the random phase approximation (RPA), or self-consistent GW are supported as well.[42] In the following, we discuss aspects of DFT+U specific to our implementation in FHI-aims, as well as brief basic validation on the standard test case bulk NiO.

3.1. Hubbard Projector Functions in FHI-Aims. In FHI-aims, KS states are expanded in real-valued NAO basis functions of the general form:

$$\varphi_{\alpha}(\mathbf{r}) = \frac{u_{\alpha}(r)}{r} Y_{lm}(\Omega) \tag{10}$$

where $u_{\alpha}(r)$ are radial functions, which are numerically tabulated and therefore fully flexible, while $Y_{lm}(\Omega)$ are the real valued spherical harmonics. $u_{\alpha}(r)$ is usually chosen to be a solution to a Schrödinger-like radial equation of atomic, ionic, or hydrogen type with an effective nuclear charge Z_{eff}.[43] Strict localization and thus computational efficiency even for large systems is ensured through an additional confinement potential, limiting the spread of all radial basis functions. The basis set is divided into a minimal basis, which only includes atomic core and valence functions, and further into preconstructed basis set levels (called *tier1*, *tier2*, ...for use with semilocal DFT). These sets are hierarchically arranged for systematic convergence from fast and qualitative to milli-electronvolt-level total energy convergence. Especially the hydrogen-like basis functions serve as polarization functions for the free atom solutions of the minimal basis set. Adding additional, higher angular momentum quantum number (l) basis functions to the overall basis set, they allow polarization of lower l functions. Furthermore, all radial functions are subject to an on-site Gram−Schmid orthogonalization. The three-dimensional integrations are performed on overlapping atom-centered grids.[44,45] These grids are predefined and divided into so-called *light*, *tight*, and *really tight* settings with increasing numerical accuracy. This terminology might be rather confusing to non FHI-aims users, for clarity.

In constructing our projector functions as a superposition of NAOs (cf., section 2.2), it is not clear per se if polarization functions of higher basis set tiers should also be included or how the presence of these functions will affect the DFT+U calculation. Note that this problem is not only specific to FHI-aims but in general occurs in any DFT+U implementation with localized basis sets.[33] This issue, together with the wider question of how to choose projector functions for DFT+U, will be discussed in more detail in section 5.

3.2. NiO. In the literature, NiO, belonging to the class of strongly correlated materials, has been extensively used as a prototype material for testing and demonstrating the effects of DFT+U.[33−35,37,46,47] In fact, LDA- or GGA-based functional approximations predict Ni3d states to dominate both the valence and the conduction band edges,[48] rendering NiO as a Mott Hubbard-type[49] insulator. Contrary to this, experimental data show that the band gap is of charge transfer type with an O2p character at the edge of the valence band.[50] Several studies, including our work, show that the DFT+U method can in fact correct for these shortcomings of plain DFT,[4,40,48,51] simply by shifting the erroneous Ni3d valence band past the O2p levels. Furthermore, we found that the results for NiO show little dependence on the choice of the projector functions (vide infra), especially with regard to polarization functions present in the standard NAO basis. Overall, this renders NiO an excellent first test case to validate our implementation.

We start with a bulk NiO structure, optimized at the PBE GGA-functional level[2] using a *tier1* basis and *tight* settings for integration grid. Not surprisingly, as we increase the U value acting on the Ni3d-states, the band gap increases almost linearly up to around U = 4 eV as depicted in Figure 1. This clearly demonstrates the typical downward and upward shift of occupied and unoccupied 3d states, respectively.[24] As only 3d-states are affected by the Hubbard correction, the deviation from linear behavior for higher U values is due to two effects. At the valence band maximum (VBM) Ni3d states shift past the O2p states, restoring the correct O2p to Ni3d character of the band gap.[40] At the conduction band minimum (CBM), higher values of U show a crossing of the 4s- with the 3d-band.[46] As the 4s-band is not influenced by the DFT+U correction, higher values of U show little to no influence on the gap beyond U = 4 eV. The DFT+U method thus can only reproduce the correct band gap character in a narrow window. To nevertheless demonstrate the efficacy of our implementation, we show in Figure 1 the gap between d-bands only. Here, one can see a linear increase over the whole plotted range of U values. Finally, Figure 1 shows slight deviations from the linear behavior even for the d-band gap. These are found to be due to

DOI: 10.1021/acs.jctc.8b01211
J. Chem. Theory Comput. 2019, 15, 1705−1718

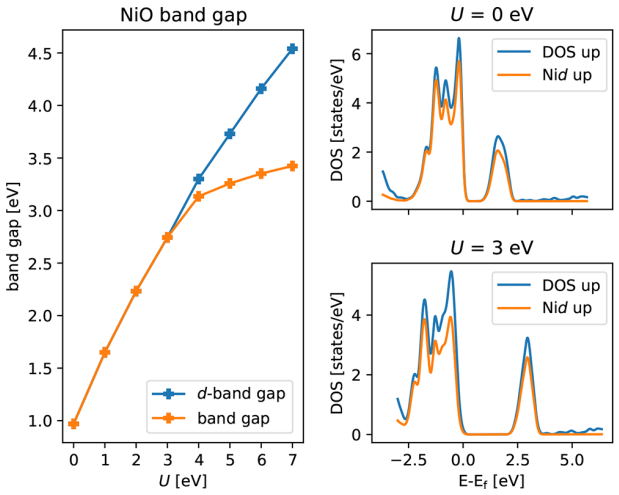

Figure 1. (Left panel) Band gap (orange) and gap between d bands (blue) of bulk NiO for increasing U values. The DFT+U correction has been applied to the Ni3d-states as described by the respective basis functions in the FHI-aims NAO basis. To rule out structural effects, all calculations have been performed for a PBE optimized structure (i.e., corresponding to U = 0). (Right panels) Density of states (DOS) and DOS projected onto the Ni3d-states for values of U = 0 eV (upper panel) and U = 3 eV (lower panel). For the sake of brevity, only up-spin DOS is shown.

changes in the amount of Nid and Op orbital hybridization as the U values increase, slightly counteracting the effect of the DFT+U correction.

4. A REAL WORLD EXAMPLE: POLARONS IN TiO_2

So far, we demonstrated the validity of our implementation on the comparatively simple example of opening the band gap in NiO. As a more realistic application example, we now further analyze its reliability by investigating the formation of polarons at the TiO_2 (110) surface, which constitutes a frequently studied showcase[52,53] where, although insensitive to the choice of U value, the results still depend most sensitively on details of the DFT+U implementation and the employed computational settings.

The physics of the problem is as follows: Removing one bridging oxygen atom from the TiO_2 (110) surface results in two excess electrons. These can be localized at varying Ti centers around or at the defect site resulting in the formation of two small trapped polarons. Furthermore, depending on the electronic spin state, the overall system is either in a triplet or in an open-shell singlet configuration. Modeling such polarons in the context of DFT+U has been extensively discussed by Deskins et al.[52] as well as Shibuya et al.[53] In general, difficulties arise from the fact that standard semilocal DFT fails in localizing the excess electrons. Moreover, different polaron localization patterns show only little difference in total energy, making it hard to isolate specific configurations in simulations. In total, this renders this system a very sensitive test case for our DFT+U implementation. Focusing on the correct description of the polaronic states, in the following we will carefully compare our results with hybrid functional (HSE06[26]) and other literature values.

4.1. Computational Details. All structure relaxations have been performed using our DFT+U variant of the PBE exchange correlation functional.[2] The Ti3d atomic basis functions were chosen as Hubbard projectors. Furthermore, all calculations were performed with the above-described rotationally invariant +U form with the double-counting correction in the fully localized limit. In fact, FLL-based double counting corrections are the standard form of DFT+U used to describe TiO_2.[52,54,55] In addition, we always employ the on-site version of the occupation matrix, if not noted otherwise. Numerical convergence was reached with default *tight tier1* basis sets for oxygen and titanium, respectively. For comparison, it has been shown that for TiO_2 systems, such a basis is equivalent in accuracy to a polarized triple-ζ split valence Gaussian-type orbital basis set.[56] However, due to mixing of the correlated Ti3d-state with the O2p-states, discussed in detail in section 5.1, we replace the *tier1* 3d-basis function with a basis function of the same kind but more localized, with a modified effective charge of Z_{eff} = 4.4e. Apart from ensuring the convergence of the DFT+U SCF cycle, this has little to no effect on the outcome of our calculations, as shown in section 4.2.1.

We use a periodic (4 × 2 × 5) slab to model the TiO_2 (110) surface, sampling reciprocal space with a (4 × 4 × 1) Monkhorst−Pack k-point grid.[57] The slab was initially cut from a bulk-optimized geometry calculated with an (8 × 8 × 8) k-grid. The first three layers of the slab were then fully relaxed until residual forces fell below 10^{-3} eV/Å. If not noted otherwise, all surface slabs have been constructed from the corresponding optimized bulk unit cells applying the same value of U.

Furthermore, we conduct a number of reference calculations with the HSE06[26] hybrid functional, which has been shown to yield excellent descriptions of the electronic structure of TiO_2.[58] Especially, the experimental band alignment of TiO_2 is reproduced within reasonable accuracy using HSE06.[59] Moreover, Shibuya et al.[53] could demonstrate that both HSE06 and DFT+U yield similar results regarding the description of polarons. Therefore, we conclude that in fact HSE06 calculations can serve here as a very good benchmark for our implemented DFT+U routines. Nevertheless, for other, less well-tested systems, one has to keep in mind that HSE06 belongs to the class of range-separated hybrid functionals incorporating two adjustable parameters for controlling the amount of exact exchange and the range-separation, both of which can significantly influence the results.[60]

As a trade-off between accuracy and computational cost, all geometry relaxations for the HSE06 reference have been performed using a standard *tier1* basis set and applying *light* integration grids. There, forces were relaxed to below 0.01 eV/Å. Finally, total energies were recalculated using the same settings as applied for the PBE+U case.

4.1.1. Localization of Polarons. Generally, the excess electrons can localize at different Ti atoms throughout the simulation cell. Different localization patterns thereby represent different local minima of the system, differing only very slightly in total energy. This renders the sampling of all configurations a difficult task. To address this problem and to ensure electron localization at the correct atomic site, we make use of the occupation matrix control approach.[61,62] There, we fix the occupation matrices of the given atoms to those obtained from a pure PBE calculation yet with modified occupations of the target orbitals for the excess electrons. This means that we simply set the corresponding diagonal entry of the associated occupation matrix to one. This effectively acts as a bias potential similar to the constrained DFT approach[63−65]

DOI: 10.1021/acs.jctc.8b01211
J. Chem. Theory Comput. 2019, 15, 1705−1718

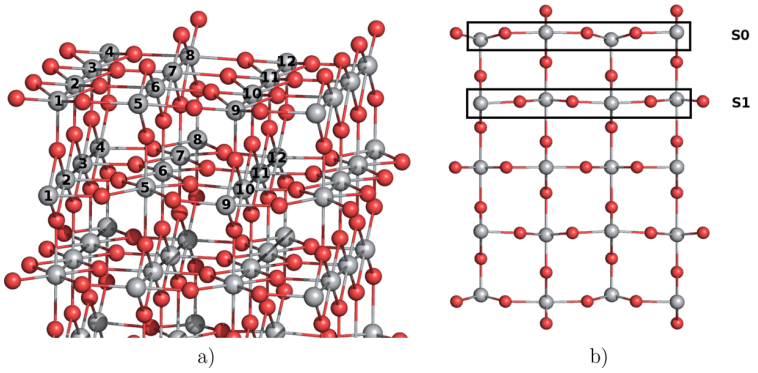

Figure 2. Depiction of the site naming convention used in this work. (a) Ti atoms are labeled within the surface layers by numbers, (b) while the topmost surface layers themselves are labeled S0 and S1. Labeling is only shown for the sites relevant to this study.

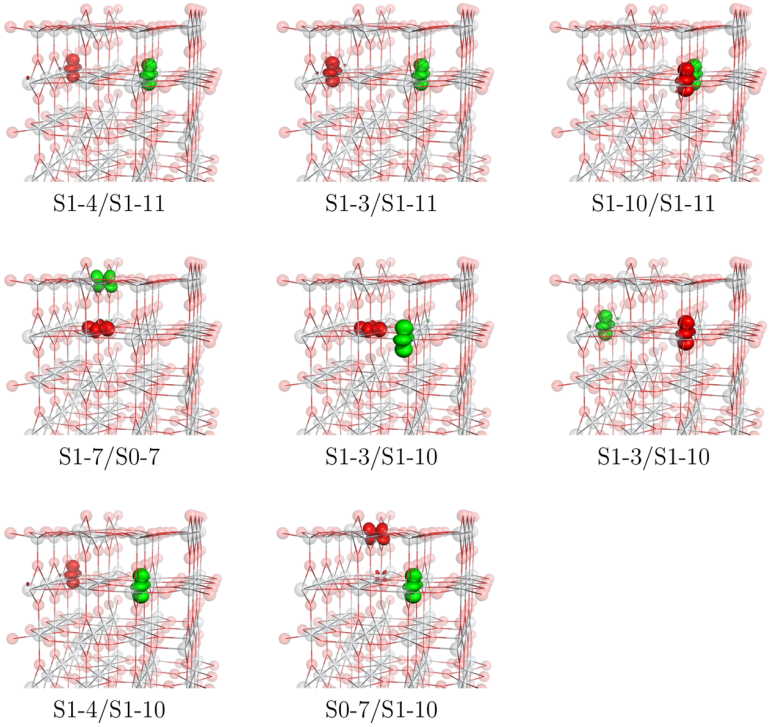

Figure 3. Spin densities of the calculated polaronic configurations (at isosurface level 0.1 e Å^{-3}). Spin up density is shown in red, while spin down density is in green.

drawing the polarons toward the intended configuration. We then perform a structure relaxation with fixed occupation matrices to appropriately polarize the environment. To achieve full self-consistency, we use the obtained geometry and wave function information as an input to perform further structural relaxations without constraining the occupation matrix. This procedure allows us to sample a large number of possible polaron configurations while yielding, at the final stage, completely unconstrained electronic structures.[62,63]

4.2. Results and Discussion. *4.2.1. Relative Formation Energies.* The stabilities of different polaronic configurations with regard to each other are determined by their relative formation energies:

$$E_{\text{formation},i} = E_{\text{tot},i} - E_{\text{tot},0} \tag{11}$$

where $E_{\text{tot},i}$ is the total DFT (or DFT+U) energy of a configuration i and $E_{\text{tot},0}$ is the total energy of the most stable polaronic configuration. In this convention, the configuration lowest in energy has a stabilization of 0.0 eV, while all other, less stable solutions have positive stabilization energies. Contrary to ref 66, we specifically do not give absolute formation energies referenced to the unoptimized, delocalized state to avoid offsets between hybrid functional calculations and DFT+U solely due to the different description of the reference state.

Although the use of the occupation matrix control approach allows us to localize the electrons at any Ti atom, for the sake of brevity we restricted ourselves to the most representative localization patterns of the excess charges. Furthermore, in line with current literature,[52,53] we only consider open-shell singlet configurations, which are considered to be more stable cas ompared to triplet configurations. In accordance with the literature,[52] the term open-shell singlet here denotes a broken symmetry DFT configuration where the number of electrons

DOI: 10.1021/acs.jctc.8b01211
J. Chem. Theory Comput. 2019, 15, 1705−1718

Table 1. Relative Stabilities of Polaronic Configurations at U = 2.65 eV (This Work) and Reference Values from Literature[a]

Ti^{3+}-centers	PBE+U (this work)	HSE06@PBE+U (this work)	HSE06 (this work)	PBE+U[52]	PBE+U[53]	HSE06[53]
S1-4/S1-11	0.00	0.00	0.00	0.00	0.00	0.00
S1-3/S1-11	6×10^{-3}	0.01	0.01	0.02		
S1-10/S1-11	0.23	0.26	0.26	0.06	0.28	0.28
S1-7/S1-9	0.40	0.47	0.45	0.23	0.23	0.27
S1-7/S0-7	1.22	1.34		0.96		0.90
S1-3/S1-10	1×10^{-3}	-2×10^{-3}		0.15		
S1-4/S1-10	-5×10^{-3}	-6×10^{-3}				
S0-7/S1-10	0.86	0.90		0.63		

[a]The relative stabilities are given in eV. The terminology HSE06@PBE+U denotes results where the geometry optimization is done with PBE+U and total energies are obtained by single point calculations using HSE06.

for spin up and spin down density is fixed so that the number of electrons is the same in both spin channels. To distinguish the polaron configurations, we rely on a nomenclature based on a numbering of atomic sites shown in Figure 2: With Sx-m/Sy-n we specify that one excess electron localizes in surface layer Sx on atom m and the second excess electron localizes in surface layer Sy on atom n.

The employed values of U were chosen to reproduce the location of the oxygen vacancy defect level within the band gap. Specifically, experimental photoemission data show that the defect state is located at around 1 eV below the conduction band.[67] We thus selected U values of 2.25, 2.5, and 2.65 eV yielding gap states between 1.0 and 1.40 eV below the conduction band for the configurations considered here (cf., Figure 3, states S1-4/S1-11). To highlight our warning that U values should not be compared between different codes, and especially not between different projectors, we note that these U values are significantly lower than those used for this kind of system so far.[52,53,68] Mainly, this can be attributed to the strongly localized character of our atomic NAO Hubbard projectors, which will be discussed in more detail in section 5. In analogy to the results of Deskins and co-workers,[52] we also find that relative stabilization energies of polaron formation remain unaffected by the exact choice of the U value. Hence, we will mainly focus on results obtained with U = 2.65 eV. As was already mentioned above, we then compare our DFT+U results to those obtained with the range-separated hybrid HSE06 functional. To rule out any further structural effects, though, the hybrid calculations were performed on the relaxed DFT+U geometries. In Table 1 we list our calculated results and compare them to literature values.

Our PBE+U results show that configurations S1-4/S1-11, S1-3/S1-11, S1-3/S1-10, and S1-4/S1-10 have almost degenerate total energies, with deviations in the range of only a few millielectronvolts. Given the intrinsic inaccuracies of DFT+U, this means that we can not identify a most stable polaronic configuration. These findings stand in direct contrast to the work of Deskins et al. and Shibuya et al., who both identified configuration S1-4/S1-11 to be the most stable singlet configuration. Interestingly, we find that configuration S1-3/S1-10 is only 1 meV higher in energy than configuration S1-4/S1-11, whereas Deskins et al. predict it to be 0.15 eV higher. Nevertheless, our DFT+U results do agree very well with our HSE06 references (both at DFT+U geometry and fully relaxed, see below), thereby demonstrating the validity of our implementation. Possible sources of the discrepancies between our results and the literature will be discussed in section 4.3.

Common to all of our energetically low-lying solutions is that all have polaron configurations located under a 5-fold coordinated Ti surface atom. This is in perfect agreement with previous theoretical and experimental studies.[69] For example, Krüger et al.[70] showed with resonant photoelectron diffraction measurements that the excess charge is dominantly located in the second layer Ti atoms located under a 5-fold coordinated surface Ti. In addition, a combined scanning tunneling microscopy/spectroscopy study by Setvin and co-workers[68] shows identical behavior for the excess charge. Even though our values do not exactly match with other theoretical studies, we thus point out that our results are perfectly in line with experimental data, which show that most of the excess charge is located below the Ti5c row. We confirm these findings by showing that polarons with this localization pattern have basically the same total energies. All other combinations show less favorable relative stabilities.

4.3. Discrepancies As Compared to Literature. While internally consistent within FHI-aims, our DFT+U and HSE06 results do show a number of discrepancies to earlier published results. To understand these, we here systematically examine potential reasons based on the differences between FHI-aims and other DFT+U capable programs.

For configuration S1-10/S1-11 with both Ti^{3+}-ions adjacent to each other, Deskins et al.[52] report a relative stabilization energy of 0.06 eV as compared to our finding of 0.23 eV and that of Shibuya and co-workers[53] of 0.28 eV, respectively. As was already discussed in ref 53, this difference in the work by Deskins et al. can be attributed to the characteristics of the underlying basis set used in the different simulations.

We also see discrepancies for polaronic configurations S1-7/S1-9 and S1-7/S0-7, which our calculation predict to be less stable. In contrast, here the findings of Deskins et al. and Shibuya et al. are in good agreement with each other. To shed more light on the these discrepancies, we performed HSE06 calculations on fixed PBE+U structures (HSE06@PBE+U). On top of that, we carry out full HSE06 calculations including relaxations for some selected systems. These results are also compiled in Table 1 and clearly show that the hybrid calculations reproduce our PBE+U energetics reasonably well. At least within the framework of our underlying electronic structure code, HSE06 and DFT+U give highly consistent results. This is also supported by the comparison of the on-site occupation matrices of the Ti^{3+} centers between PBE+U and HSE06. Even though HSE06 does not include any DFT+U corrections, we there calculate the on-site occupation in the same way as with PBE+U. We obtain essentially identical orbital localization patterns at both levels of theory, confirming to one end that PBE+U and HSE06 describe the polaron states

DOI: 10.1021/acs.jctc.8b01211
J. Chem. Theory Comput. 2019, 15, 1705−1718

in the same way and to the other end the reliability of our DFT +U implementation. This similarity at both levels of theory also rules out that the different NAO projector functions used in our work stand behind the discrepancies, because the HSE06 calculations are completely independent of any sort of projector functions and serve as an unbiased reference.

An alternative explanation for the discrepancies between our results and those from Shibuya et al. and Deskins and co-workers could be that the differences in the energetics arise from electrons occupying different orbitals on the Ti^{3+} centers, thus effectively yielding different states. However, for configurations S1-4/S1-11, S1-10/S1-11, S1-7/S1-9, and S1-7/S0-7, we obtain charge densities identical to those reported by Shibuya et al. (cf., Figure 3). For configuration S1-3/S1-11, which is also depicted in ref 69, our orbital localization pattern also perfectly agrees with the literature results. Another possibility could be that our modification of the standard NAO basis (cf., section 4.1) induces the described discrepancies. To rule this out, we conducted additional HSE06 calculations on the S1-3/S1-11 system and including this basis function. However, this did not affect the results reported in Table 1 in any significant way.

Having thus exhausted all other possible reasons for the systematic discrepancies between FHI-aims and the literature, we point out that there is one last difference between FHI-aims and the program packages used in the works of Shibuya and co-workers and Deskins et al. in that the latter employ pseudopotentials to approximate core electrons, while FHI-aims is a full potential code. Pseudopotentials are commonly constructed from LDA or GGA reference calculations and therefore are, in principle, not necessarily transferable to hybrid DFT or DFT+U applications. Note that the literature shows that hybrid DFT or DFT+U works remarkably well with pseudopotentials.[66] Yet, it is unclear if this holds true for such ultrasensitive systems like polarons, and clearly further studies are needed to shed more light on this issue.

5. CHOICE OF PROJECTOR FUNCTIONS AND OCCUPATION MATRIX DEFINITION

We already highlighted that our implementation of the DFT +U method needs much lower values of U to achieve results similar to other codes. This is, in part, due to our choice of projector functions. In this section, we therefore further explore the influence of the exact shape of the Hubbard projectors and the occupation matrix definition on our results. To this end, we use two different kinds of functions for the projectors. First we use atomic-type basis functions, which are in fact the default choice for Hubbard projectors of a given element. In addition, we use hydrogen-like radial projector functions characterized by different effective core charges (Z_{eff} = 4.4e and 7.0e). We thus generate a series of different projector functions, which differ in their radial extent, ranging from a very compact, localized shape to a more diffuse radial function (Z_{eff} = 4.4e). For comparison, the radial parts of all three projector functions are depicted Figure 4. However, as all basis functions of FHI-aims are subject to an on-site orthogonalization, one can not directly use them as projector functions. Thus, so as not to add spurious nodes to our projector functions due to the orthogonalization, we express each not orthogonalized basis function serving as a Hubbard projector (cf., Figure 4) in terms of the orthogonalized basis set.

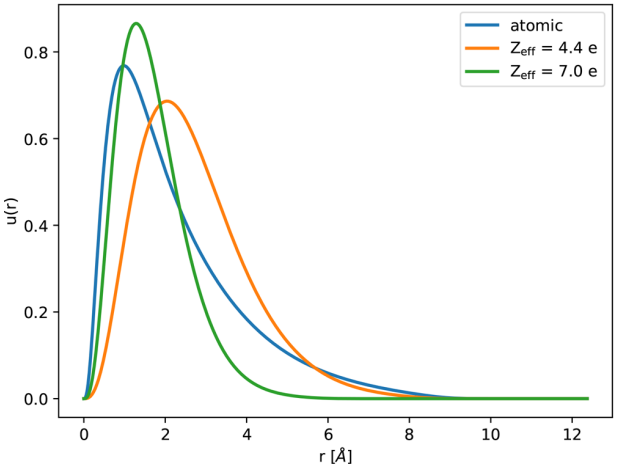

Figure 4. Radial functions of an atomic type (blue) and of two hydrogen-like Hubbard projectors (orange, green). The hydrogen-like Hubbard projectors are characterized by their effective core charge Z_{eff}.

For our analysis, we choose the TiO_2 defect level location with respect to the conduction band edge and the highest eigenvalue of the occupation matrix as observables. For the sake of brevity and without loss of generality, we only show this for configuration S1-4/S1-11 and for a single Ti^{3+} center.

First, for both the highest eigenvalue and the defect level location, we see an almost linear dependence with respect to the applied U value (cf., Figure 5). Although we used a small range of U values (from U = 2.25 eV to U = 2.65 eV), representative for the values used in realistic simulations, we see a large increase in the shift of the defect state away from the conduction band edge, at least for the on-site representation in connection with atomic-like Hubbard

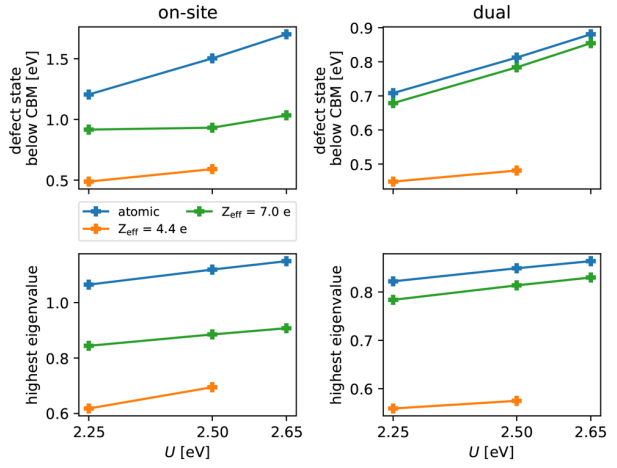

Figure 5. Defect level location within the band gap (upper panels) and highest eigenvalue of the occupation matrix (lower panels) with respect to the applied U value and different Hubbard projector functions. Also shown is the dependence on the occupation matrix representation (left and right panels). For all calculations, the S1-4/S1-11 structure obtained from a PBE+U (=2.65 eV) calculation, applying the on-site definition for the occupation matrix, has been used. No self-consistent field solution for Z_{eff} = 4.4 at U = 2.65 eV or higher could be found, indicating that there is no stable solution for such a diffuse projector.

DOI: 10.1021/acs.jctc.8b01211
J. Chem. Theory Comput. 2019, 15, 1705−1718

projectors. Overall, this effect is less pronounced the more diffuse the projector function becomes. In general, more diffuse Hubbard projectors yield a higher defect level position within the band gap for a given U value. This also holds true for the charge localization within the correlated subspace, reflected by smaller eigenvalues of the occupation matrix for the more diffuse projector functions. We attribute this tendency to a preference of the excess electrons in occupying the 3d atomic basis functions. Both effects are also very much in line with our observation that in production calculations with our strongly localized NAO projector, we generally need much lower U values to achieve the same correction as other implementations. We therefore conclude that within our given framework the atomic-like projectors are in fact the most suitable ones for this kind of problem.

For projector functions with Z_{eff} = 4.4e, we do not find a converged self-consistent field solution for U = 2.65 eV or higher. This indicates that there is no stable solution for such a diffuse projector, which effectively tries to shift the charge away from the Ti atom center to the neighboring atoms, as depicted for the S1-4/S1-11 configuration in Figure 6. Not surprisingly,

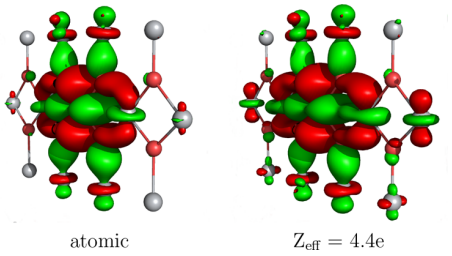

Figure 6. Electron density of the polaron state in configuration S1-4/S1-11 calculated with atomic (left) and hydrogen-like Hubbard projectors with an effective charge of Z_{eff} = 4.4e (right). The Ti^{3+} atom is located in the center. Densities are obtained with PBE+U (=2.5 eV) and the on-site representation for the occupation matrix. Isosurface level 0.05 e $Å^{-3}$.

this shows that the degree of charge localization can also be tuned by choosing localized or less localized projector functions. In general, this can be compensated by choosing higher U values, but only up to a certain degree. Beyond that, the corrective Hubbard potential tries to enforce the target ground state to match with the shape of the applied projectors spanning the correlated subspace.

Regarding the dependence on the occupation matrix definition, we see the same tendencies for the dual representation; however, higher U values are needed to match the on-site representation results. Such behavior has been already observed by Han et al. in the context of the band gap width.[33]

In summary, the Hubbard projector shape directly influences the degree of localization of the excess charge in the system. To a certain degree, this can be compensated by choosing a higher U value, which again demonstrates that U values are not directly comparable between different electronic structure codes.

5.1. Multiple Polarization Functions in an NAO Basis.

Finally, we investigated the impact of having basis sets with multiple basis functions belonging to the same angular momentum channel, which are thus potentially associated with same correlated subspace. This is a problem unique to DFT codes with localized basis sets, although it could be less pronounced for programs with less specialized basis functions than the NAOs used in FHI-aims. As a test case, we focus on a bulk rutile TiO_2 unit cell applying a standard *tight*, *tier1* basis set for oxygen and titanium, respectively. As before, we apply the PBE+U method with on-site representation in the fully localized limit for the Titanium 3d-states. As projector functions, only the atomic-type basis functions are used. Yet, to check the influence of a present polarization function, we vary the effective core charge (Z_{eff}) of the present 3d *tier1* basis function, specifically not included in the DFT+U projector, from 1.5e to 4.0e. This demonstrates the interaction of additional 3d-orbitals of different radial shape with the DFT+U projector.

Our findings regarding the average occupation of the different correlated subspaces are compiled in Table 2 for a

Table 2. Average Occupation of the Correlated Subspace at Different U Values and with Different *tier1* 3d-Polarization Functions or without (Single Shell)[a]

	Z_{eff}			
U [eV]	1.5	2.7[b]	4.0	single shell
0.00	0.14	0.15	0.14	0.14
2.25	0.05	0.09	0.12	0.13
3.00	0.04	0.08	0.12	0.11
4.00	0.03	0.07	0.11	0.12
HSE06	0.13	0.12	0.13	0.12

[a]As a comparison, we also list the average occupations resulting from hybrid HSE06 DFT calculations, yet with U = 0 eV, calculated with the on-site occupation matrix. [b]Hydrogen-like 3d-polarization function, which is part of the standard default settings for titanium.

number of increasing U values. Thereby, the average occupation is calculated as the sum of eigenvalues of the occupation matrix divided by the angular multiplicity of the correlated subspace, $\sum_m \frac{n_{mm}}{2l+1}$. TiO_2 is characterized by a strong mixing of Ti3d- and O2p-states, which leads to a significantly covalent character of the Ti−O bonds.[39] Hence, the use of a pure 3d atomic-like Hubbard projector is less valid, resulting in the low average occupation numbers listed in Table 2. On applying the corrective U potential, the main effect is to push the spatial character of the Ti3d-states closer to the free-atom reference, thereby causing less overlap with the O2p-states. This results in an even more strongly pronounced oxygen p-character of the valence states, explaining the slight decrease in average occupation at higher U values.

At the plain PBE level (U = 0 eV), the presence of additional polarization functions has no significant impact on the average occupation as compared to the single shell case. This indicates that the states are in fact dominated by atomic-type 3d basis functions instead of polarization functions. If the U value is increased, a change in the average occupation can be observed in all cases. However, this change is even stronger for Z_{eff} = 1.5e and 2.7e. This is partly a real effect as higher U values will alter the hybridization between Ti3d- and O2p-orbitals, yielding less d character of the valence states.

Yet, another effect of higher U values is the system's tendency to occupy the additional polarization function instead of the more localized atomic basis. As can be seen in Table 2, this trend increases, the more diffuse the basis function becomes. To gauge the physically correct occupation of the correlated subspace, we again performed calculations with the

DOI: 10.1021/acs.jctc.8b01211
J. Chem. Theory Comput. 2019, 15, 1705−1718

HSE06 functional. The hybrid DFT reference shows that the average occupation of the correlated subspace is not significantly affected by the presence of additional 3d basis functions (see Table 2). Moreover, it should be pointed out that these results indicate a physically incorrect description of rutile TiO_2 by PBE+U, at least for Z_{eff} = 1.5e and 2.7e. In pure PBE (U = 0 eV) and HSE06, the atomic-type 3d basis functions dominate in the mixing with O2p-states. If the U value is increased in the presence of an additional, more diffuse polarization function, the situation changes, and the diffuse 3d basis functions start more and more to mix with the O2p-states. It should be noted that this effect is independent of the choice of representation for the occupation matrix and also occurs for the dual representation.

We attribute this failing of DFT+U to the problem of defining proper Hubbard projectors and hence the correct identification of the localized subspace in question, a well-known general drawback of DFT+U.[30] As compared to DFT+U, in hybrid functionals all interactions among electrons are treated in the same way involving one mixing factor and explicit calculations of the Fock-integrals. This makes hybrid DFT results much more robust with regard to basis set choices. These findings are particularly relevant for studies with FHI-aims, where the default basis set for titanium includes the 3d basis function with an effective core charge of 2.7e. This means that a simple and straightforward application of the DFT+U method to TiO_2 with an unmodified NAO basis is likely to fail. One possible way to circumvent this would be to simply exclude the offending basis function from a simulation. This, however, requires a careful analysis if any other physical properties are negatively affected by the thus reduced basis set. Nevertheless, we here emphasize that this is a very element-specific and system-dependent problem of the underlying basis set in FHI-aims and may not cause any concerns in other simulations at all, especially for system with less covalent character.

As another, more systematic, remedy, our implementation also allows the use of Hubbard projectors of arbitrary shape as long as they can be represented as a linear combination of basis functions (cf., eq 1b). In the following, we use a free-ion-like 3d titanium radial function and express this function in terms of basis functions present in the default *tier1* set (Figure 7). This results in expansion coefficients of the atomic and polarization function (Z_{eff} = 2.7e) of c_1 = 0.982 and c_2 = −0.209, respectively. Using this projector, all present 3d basis functions contribute to the correlated subspace, suppressing the aforementioned problems of low subspace occupation.

As Table 3 shows, applying the DFT+U correction also for the 3d polarization functions improves the average occupation numbers. Thus, the physical correct description of subspace occupancies is restored by suppressing the nonphysical strong mixing of the *tier1* polarization function with the O2p-states. A similar effect could have been achieved instead by treating the polarization functions as a separate 3d-shell.[33] Yet, this would involve using a second U parameter, which needs to be determined separately, rendering such an approach less general.

In summary, our findings demonstrate that additional polarization functions can affect the DFT+U calculation especially for materials with strong hybridization between different species. Although we here illustrated this effect for the FHI-aims NAO basis set and for Ti, it should also be present in other localized basis sets. Obviously, for some cases, it can be necessary to include polarization functions in the Hubbard correction; however, it is not known a priori how this will affect the accuracy of other predicted physical quantities. Thus, one should generally be well aware of these issues resulting from the ambiguity of DFT+U with regard to the Hubbard projectors and their interplay with localized basis sets.

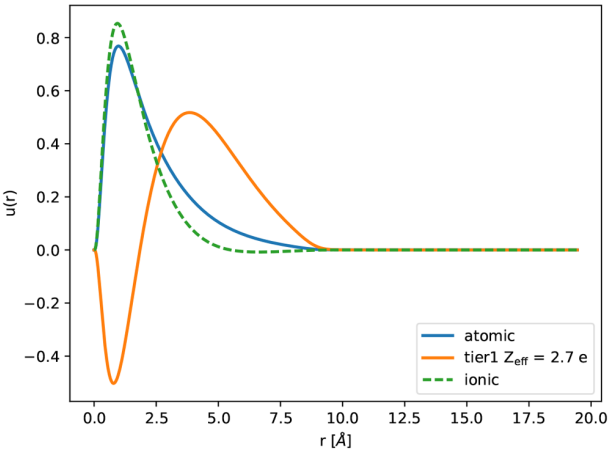

Figure 7. Free-ion-like Ti3d radial function (red dashed line) expressed as a linear combination of an atomic and *tier1* Ti3d radial basis function, both part of the standard *tight* Ti basis set in FHI-aims. The *tier1* radial basis function is subject to a Gram−Schmidt orthogonalization with respect to the atomic function.

Table 3. Average Occupation of the Correlated Subspace at Different U Values for the Default *tier1* Titanium Basis Set of FHI-Aims Using a Hubbard Projector Derived from a Free-Ion-Like Solution

U [eV]	0.00	2.25	3.00	4.00
$\sum \frac{n_{mm}}{2l+1}$	0.14	0.12	0.11	0.10

6. CONCLUSION

We presented our implementation of the Hubbard corrected DFT+U method within the full-potential all-electron code FHI-aims. The efficacy of the DFT+U approach thereby rests in no small part on an appropriate choice of projector functions defining the correlated subspace to which the correction needs to be applied. Our implementation allows the use of arbitrary radial shapes of the Hubbard projectors as long these projector functions can be represented by a linear combination of the NAO basis functions of FHI-aims. The default choice for the projector functions, which serve to gauge the contributions of each KS-orbital to the correlated states, are highly localized NAO basis functions derived from free atom solutions. Besides needing significantly lower values of U to achieve results similar to those of other DFT+U implementations, our NAO-based projectors additionally allow for a computationally highly efficient determination of the DFT+U correction terms at basically no overhead as compared to standard semilocal DFT.

As a first example showing the accuracy and efficacy of our implementation, we calculated the band gap opening of the often employed NiO test-system with respect to increased values of U. Our NAO-based projector functions achieve results very similar to those found in the literature, yet also at lower U values due to the highly localized reference states.

DOI: 10.1021/acs.jctc.8b01211
J. Chem. Theory Comput. 2019, 15, 1705−1718

Further, we investigated the presence of multiple polarization functions belonging to the angular momentum channel of the correlated subspace but not included in the projector function itself. Considering that FHI-aims employs an on-site orthogonalization of basis functions, this can lead to electron leakage out of the correlated subspace into the other present basis functions and thereby leading to an erroneous prediction of the electronic ground state and related physical properties. As we demonstrated for bulk TiO_2, this effect can be suppressed by expanding the correlated subspace over the whole angular momentum channel in question, for example, by using a numeric ionic reference orbital. We emphasize that this effect is element- and system-specific and will strongly depend on the basis functions used in the simulation.

As a more stringent and applied test case for our implementation, we also studied the surface polaron formation due to an oxygen vacancy in rutile TiO_2(110). Comparing our DFT+U results with hybrid functional (HSE06) calculations, we showed that our code yields almost identical ground-state properties. Nevertheless, for both DFT+U and HSE06, we could not find one single most stable polaronic configuration, which stands in contrast to previous theoretical studies.[52,53,68] Instead, we identified several localization patterns essentially degenerate in energy. All of these are characterized by Ti^{3+} located under a 5-fold coordinated surface Ti atom. We showed that our obtained charge density distributions are identical to those obtained from the literature, thereby ruling out the possibility of missing the correct ground-state orbital occupation of the polaron state. Exhausting all other possibilities, this difference can likely be explained by the pseudo potentials applied in earlier studies. Moreover, it should be pointed out that our results are also in line with experimental data,[69,70] providing additional support for our findings.

Finally, we then analyzed the influence of the Hubbard projector shape on the polaronic states. Not surprisingly, more diffuse projectors lead to less localized excess charge. This is partly compensated by higher U values, demonstrating again the incomparability of U values throughout different electronic structure codes. All in all, our extensive study highlights the dangers of an uncritical use of DFT+U, in particular in localized basis set codes, while at the same time emphasizing the versatility and usefulness of this effective approach, if used properly.

AUTHOR INFORMATION

Corresponding Author

*E-mail: harald.oberhofer@ch.tum.de.

ORCID

Karsten Reuter: 0000-0001-8473-8659

Harald Oberhofer: 0000-0002-5791-6736

Funding

We gratefully acknowledge support from the Solar Technologies Go Hybrid Initiative of the State of Bavaria and the German Science Foundation DFG (Grant OB425/4-1).

Notes

The authors declare no competing financial interest.

REFERENCES

(1) Hohenberg, P.; Kohn, W. "Inhomogeneous Electron Gas. *Phys. Rev.* **1964**, *136*, B864−B871.

(2) Perdew, J. P.; Burke, K.; Ernzerhof, M. Generalized Gradient Approximation Made Simple. *Phys. Rev. Lett.* **1996**, *77*, 3865−3868.

(3) Kohn, W.; Sham, L. J. Self-Consistent Equations Including Exchange and Correlation Effects. *Phys. Rev.* **1965**, *140*, A1133−A1138.

(4) Pickett, W. E.; Erwin, S. C.; Ethridge, E. C. Reformulation of the LDA+U method for a local-orbital basis. *Phys. Rev. B: Condens. Matter Mater. Phys.* **1998**, *58*, 1201−1209.

(5) Pacchioni, G. Modeling doped and defective oxides in catalysis with density functional theory methods: Room for improvements. *J. Chem. Phys.* **2008**, *128*, 182505.

(6) Finazzi, E.; Di Valentin, C.; Pacchioni, G.; Selloni, A. Excess electron states in reduced bulk anatase TiO2: Comparison of standard GGA, GGA+U, and hybrid DFT calculations. *J. Chem. Phys.* **2008**, *129*, 154113.

(7) Pegg, J. T.; Aparicio-Anglès, X.; Storr, M.; de Leeuw, N. H. DFT +U study of the structures and properties of the actinide dioxides. *J. Nucl. Mater.* **2017**, *492*, 269−278.

(8) Dorado, B.; Jomard, G.; Freyss, M.; Bertolus, M. Stability of oxygen point defects in UO_2 by first-principles DFT+U calculations: Occupation matrix control and Jahn-Teller distortion. *Phys. Rev. B: Condens. Matter Mater. Phys.* **2010**, *82*, 035114.

(9) Cohen, A. J.; Mori-Sánchez, P.; Yang, W. Insights into current limitations of density functional theory. *Science* **2008**, *321*, 792−794.

(10) Anisimov, V.; Zaanen, J.; Andersen, O. K. Band theory and Mott insulators: Hubbard *U* instead of Stoner *I*. *Phys. Rev. B: Condens. Matter Mater. Phys.* **1991**, *44*, 943−954.

(11) Dudarev, S. L.; Botton, G. A.; Savrasov, S. Y.; Humphreys, C. J.; Sutton, A. P. Electron-energy-loss spectra and the structural stability of nickel oxide: An LSDA+U study. *Phys. Rev. B: Condens. Matter Mater. Phys.* **1998**, *57*, 1505−1509.

(12) Hubbard, J. Electron Correlations in Narrow Energy Bands. *Proc. R. Soc. A* **1963**, *276*, 238−257.

(13) Perdew, J. P.; Zunger, A. Self-interaction correction to density-functional approximations for many-electron systems. *Phys. Rev. B: Condens. Matter Mater. Phys.* **1981**, *23*, 5048−5079.

(14) Kao, D.-y.; Withanage, K.; Hahn, T.; Batool, J.; Kortus, J.; Jackson, K. Self-consistent self-interaction corrected density functional theory calculations for atoms using Fermi-Löwdin orbitals: Optimized Fermi-orbital descriptors for Li-Kr. *J. Chem. Phys.* **2017**, *147*, 164107.

(15) Schwalbe, S.; Hahn, T.; Liebing, S.; Trepte, K.; Kortus, J. Fermi-Löwdin orbital self-interaction corrected density functional theory: Ionization potentials and enthalpies of formation. *J. Comput. Chem.* **2018**, *39*, 2463−2471.

(16) Yang, Z.-h.; Pederson, M. R.; Perdew, J. P. Full self-consistency in the Fermi-orbital self-interaction correction. *Phys. Rev. A: At., Mol., Opt. Phys.* **2017**, *95*, 052505.

(17) Pederson, M. R.; Ruzsinszky, A.; Perdew, J. P. Communication: Self-interaction correction with unitary invariance in density functional theory. *J. Chem. Phys.* **2014**, *140*, 121103.

(18) Berger, D.; Logsdail, A. J.; Oberhofer, H.; Farrow, M. R.; Catlow, C. R. A.; Sherwood, P.; Sokol, A. A.; Blum, V.; Reuter, K. Embedded-cluster calculations in a numeric atomic orbital density-functional theory framework. *J. Chem. Phys.* **2014**, *141*, 024105.

(19) Berger, D.; Oberhofer, H.; Reuter, K. First-principles embedded-cluster calculations of the neutral and charged oxygen vacancy at the rutile TiO_2(110) surface. *Phys. Rev. B: Condens. Matter Mater. Phys.* **2015**, *92*, 075308.

(20) Kubas, A.; Berger, D.; Oberhofer, H.; Maganas, D.; Reuter, K.; Neese, F. Surface Adsorption Energetics Studied with "Gold Standard" Wave-Function-Based Ab Initio Methods: Small-Molecule Binding to TiO2(110). *J. Phys. Chem. Lett.* **2016**, *7*, 4207−4212.

(21) Anderson, P. W. Localized Magnetic States in Metals. *Phys. Rev.* **1961**, *124*, 41−53.

(22) Mori-Sánchez, P.; Cohen, A. J.; Yang, W. Many-electron self-interaction error in approximate density functionals. *J. Chem. Phys.* **2006**, *125*, 201102.

(23) Moynihan, G.; Teobaldi, G.; O'Regan, D. D. Inapplicability of exact constraints and a minimal two-parameter generalization to the

DOI: 10.1021/acs.jctc.8b01211
J. Chem. Theory Comput. 2019, 15, 1705−1718

DFT+*U* based correction of self-interaction error. *Phys. Rev. B: Condens. Matter Mater. Phys.* **2016**, *94*, 220104.
(24) Himmetoglu, B.; Floris, A.; de Gironcoli, S.; Cococcioni, M. "Hubbard-corrected DFT energy functionals: The LDA+U description of correlated systems. *Int. J. Quantum Chem.* **2014**, *114*, 14−49.
(25) Agapito, L. A.; Curtarolo, S.; Buongiorno Nardelli, M. Reformulation of DFT + *U* as a Pseudohybrid Hubbard Density Functional for Accelerated Materials Discovery. *Phys. Rev. X* **2015**, *5*, 011006.
(26) Moussa, J. E.; Schultz, P. A.; Chelikowsky, J. R. "Analysis of the Heyd-Scuseria-Ernzerhof density functional parameter space. *J. Chem. Phys.* **2012**, *136*, 204117.
(27) Adamo, C.; Barone, V. Toward reliable density functional methods without adjustable parameters: The PBE0 model. *J. Chem. Phys.* **1999**, *110*, 6158−6170.
(28) Mulliken, R. S. Electronic Population Analysis on LCAO-MO Molecular Wave Functions. I. *J. Chem. Phys.* **1955**, *23*, 1833−1840.
(29) Löwdin, P. On the Non Orthogonality Problem Connected with the Use of Atomic Wave Functions in the Theory of Molecules and Crystals. *J. Chem. Phys.* **1950**, *18*, 365−375.
(30) O'Regan, D. D.; Hine, N. D. M.; Payne, M. C.; Mostofi, A. A. Projector self-consistent DFT + *U* using nonorthogonal generalized Wannier functions. *Phys. Rev. B: Condens. Matter Mater. Phys.* **2010**, *82*, 081102.
(31) Eschrig, H.; Koepernik, K.; Chaplygin, I. Density functional application to strongly correlated electron systems. *J. Solid State Chem.* **2003**, *176*, 482−495.
(32) Blum, V.; Gehrke, R.; Hanke, F.; Havu, P.; Havu, V.; Ren, X.; Reuter, K.; Scheffler, M. Ab initio molecular simulations with numeric atom-centered orbitals. *Comput. Phys. Commun.* **2009**, *180*, 2175−2196.
(33) Han, M. J.; Ozaki, T.; Yu, J. O(N) LDA+U electronic structure calculation method based on the nonorthogonal pseudoatomic orbital basis. *Phys. Rev. B: Condens. Matter Mater. Phys.* **2006**, *73*, 045110.
(34) O'Regan, D. D.; Payne, M. C.; Mostofi, A. A. Subspace representations in *ab initio* methods for strongly correlated systems. *Phys. Rev. B: Condens. Matter Mater. Phys.* **2011**, *83*, 245124.
(35) Tablero, C. Representations of the occupation number matrix on the LDA/GGA+ U method. *J. Phys.: Condens. Matter* **2008**, *20*, 325205.
(36) Liechtenstein, A. I.; Anisimov, V. I.; Zaanen, J. Density-functional theory and strong interactions: Orbital ordering in Mott-Hubbard insulators. *Phys. Rev. B: Condens. Matter Mater. Phys.* **1995**, *52*, R5467−R5470.
(37) Petukhov, A. G.; Mazin, I. I.; Chioncel, L.; Lichtenstein, A. I. Correlated metals and the LDA+U method. *Phys. Rev. B: Condens. Matter Mater. Phys.* **2003**, *67*, 153106.
(38) O'Donnell, K. P.; Dierolf, V. *Rare-Earth Doped III-Nitrides for Optoelectronic and Spintronic Applications*; Topics in Applied Physics; Springer: Netherlands, 2010.
(39) Arroyo-de Dompablo, M. E.; Morales-García, A.; Taravillo, M. DFT+U calculations of crystal lattice, electronic structure, and phase stability under pressure of TiO2 polymorphs. *J. Chem. Phys.* **2011**, *135*, 054503.
(40) Cococcioni, M.; de Gironcoli, S. Linear response approach to the calculation of the effective interaction parameters in the LDA+U method. *Phys. Rev. B: Condens. Matter Mater. Phys.* **2005**, *71*, 035105.
(41) Santana, J. A.; Kim, J.; Kent, P. R. C.; Reboredo, F. A. Successes and failures of Hubbard-corrected density functional theory: The case of Mg doped LiCoO2. *J. Chem. Phys.* **2014**, *141*, 164706.
(42) Ren, X.; Rinke, P.; Blum, V.; Wieferink, J.; Tkatchenko, A.; Sanfilippo, A.; Reuter, K.; Scheffler, M. Resolution-of-identity approach to Hartree-Fock, hybrid density functionals, RPA, MP2 and GW with numeric atom-centered orbital basis functions. *New J. Phys.* **2012**, *14*, 053020.
(43) Havu, V.; Blum, V.; Havu, P.; Scheffler, M. Efficient integration for all-electron electronic structure calculation using numeric basis functions. *J. Comput. Phys.* **2009**, *228*, 8367−8379.
(44) Becke, A. D. A multicenter numerical integration scheme for polyatomic molecules. *J. Chem. Phys.* **1988**, *88*, 2547−2553.
(45) Delley, B. An all-electron numerical method for solving the local density functional for polyatomic molecules. *J. Chem. Phys.* **1990**, *92*, 508−517.
(46) Jiang, H.; Gomez-Abal, R. I.; Rinke, P.; Scheffler, M. First-principles modeling of localized d states with the *GW*@LDA + *U* approach. *Phys. Rev. B: Condens. Matter Mater. Phys.* **2010**, *82*, 045108.
(47) Park, S. Y.; Choi, H. J. First-principles calculation of atomic force in the LSDA+U formalism. *Phys. Rev. B: Condens. Matter Mater. Phys.* **2009**, *80*, 155122.
(48) Bengone, O.; Alouani, M.; Blöchl, P.; Hugel, J. Implementation of the projector augmented-wave LDA+U method: Application to the electronic structure of NiO. *Phys. Rev. B: Condens. Matter Mater. Phys.* **2000**, *62*, 16392−16401.
(49) Mott, N. F. The Basis of the Electron Theory of Metals, with Special Reference to the Transition Metals. *Proc. Phys. Soc., London, Sect. A* **1949**, *62*, 416−422.
(50) Sawatzky, G. A.; Allen, J. W. Magnitude and Origin of the Band Gap in NiO. *Phys. Rev. Lett.* **1984**, *53*, 2339−2342.
(51) Anisimov, V. I.; Solovyev, I. V.; Korotin, M. A.; Czyżyk, M. T.; Sawatzky, G. A. Density-functional theory and NiO photoemission spectra. *Phys. Rev. B: Condens. Matter Mater. Phys.* **1993**, *48*, 16929−16934.
(52) Deskins, N. A.; Rousseau, R.; Dupuis, M. Distribution of Ti^{3+} Surface Sites in Reduced TiO_2. *J. Phys. Chem. C* **2011**, *115*, 7562−7572.
(53) Shibuya, T.; Yasuoka, K.; Mirbt, S.; Sanyal, B. A systematic study of polarons due to oxygen vacancy formation at the rutile TiO 2 (110) surface by GGA + U and HSE06 methods. *J. Phys.: Condens. Matter* **2012**, *24*, 435504.
(54) Morgan, B. J.; Watson, G. W. A DFT+U description of oxygen vacancies at the TiO2 rutile (110) surface. *Surf. Sci.* **2007**, *601*, 5034−5041.
(55) Magyari-Köpe, B.; Park, S.; Lee, H.; Nishi, Y. First principles calculations of oxygen vacancy-ordering effects in resistance change memory materials incorporating binary transition metal oxides. *J. Mater. Sci.* **2012**, *47*, 7498−7514.
(56) Lamiel-Garcia, O.; Ko, K. C.; Lee, J. Y.; Bromley, S. T.; Illas, F. When Anatase Nanoparticles Become Bulklike: Properties of Realistic TiO2 Nanoparticles in the 1−6 nm Size Range from All Electron Relativistic Density Functional Theory Based Calculations. *J. Chem. Theory Comput.* **2017**, *13*, 1785−1793. PMID: 28230983.
(57) Monkhorst, H. J.; Pack, J. D. Special points for Brillouin-zone integrations. *Phys. Rev. B* **1976**, *13*, 5188−5192.
(58) Viñes, F.; Lamiel-García, O.; Chul Ko, K.; Yong Lee, J.; Illas, F. Systematic study of the effect of HSE functional internal parameters on the electronic structure and band gap of a representative set of metal oxides. *J. Comput. Chem.* **2017**, *38*, 781−789.
(59) Cheng, J.; Sprik, M. Alignment of electronic energy levels at electrochemical interfaces. *Phys. Chem. Chem. Phys.* **2012**, *14*, 11245−11267.
(60) Krukau, A. V.; Vydrov, O. A.; Izmaylov, A. F.; Scuseria, G. E. Influence of the exchange screening parameter on the performance of screened hybrid functionals. *J. Chem. Phys.* **2006**, *125*, 224106.
(61) Dorado, B.; Amadon, B.; Freyss, M.; Bertolus, M. DFT + U. *Phys. Rev. B: Condens. Matter Mater. Phys.* **2009**, *79*, 235125.
(62) Allen, J. P.; Watson, G. W. Occupation matrix control of d- and f-electron localisations using DFT + U. *Phys. Chem. Chem. Phys.* **2014**, *16*, 21016−21031.
(63) Wu, Q.; Van Voorhis, T. Direct optimization method to study constrained systems within density-functional theory. *Phys. Rev. A: At., Mol., Opt. Phys.* **2005**, *72*, 024502.
(64) Kaduk, B.; Kowalczyk, T.; Van Voorhis, T. Constrained Density Functional Theory. *Chem. Rev.* **2012**, *112*, 321−370.
(65) Behler, J.; Delley, B.; Reuter, K.; Scheffler, M. Nonadiabatic potential-energy surfaces by constrained density-functional theory. *Phys. Rev. B: Condens. Matter Mater. Phys.* **2007**, *75*, 115409.

DOI: 10.1021/acs.jctc.8b01211
J. Chem. Theory Comput. 2019, 15, 1705−1718

(66) Wang, Z.; Brock, C.; Matt, A.; Bevan, K. H. Implications of the DFT + *U* method on polaron properties in energy materials. *Phys. Rev. B: Condens. Matter Mater. Phys.* **2017**, *96*, 125150.
(67) Yim, C. M.; Pang, C. L.; Thornton, G. Oxygen Vacancy Origin of the Surface Band-Gap State of TiO_2(110). *Phys. Rev. Lett.* **2010**, *104*, 036806.
(68) Kowalski, P. M.; Camellone, M. F.; Nair, N. N.; Meyer, B.; Marx, D. Charge Localization Dynamics Induced by Oxygen Vacancies on the TiO_2(110) Surface. *Phys. Rev. Lett.* **2010**, *105*, 146405.
(69) Setvin, M.; Franchini, C.; Hao, X.; Schmid, M.; Janotti, A.; Kaltak, M.; Van de Walle, C. G.; Kresse, G.; Diebold, U. Direct View at Excess Electrons in TiO_2 Rutile and Anatase. *Phys. Rev. Lett.* **2014**, *113*, 086402.
(70) Krüger, P.; Bourgeois, S.; Domenichini, B.; Magnan, H.; Chandesris, D.; Le Fèvre, P.; Flank, A. M.; Jupille, J.; Floreano, L.; Cossaro, A.; Verdini, A.; Morgante, A. Defect States at the TiO_2(110) Surface Probed by Resonant Photoelectron Diffraction. *Phys. Rev. Lett.* **2008**, *100*, 055501.

DOI: 10.1021/acs.jctc.8b01211
J. Chem. Theory Comput. 2019, 15, 1705−1718

B Paper # 2

Towards a Transferable Design of Solid-state Embedding Models on the Example of a Rutile TiO_2 (110) Surface

Matthias Kick and Harald Oberhofer
J. Chem. Phys. 151, 184114 (2019).
DOI:10.1063/1.5125204
Reproduced from [J. Chem. Phys. 151, 184114 (2019)], with the permission of AIP Publishing.

The Journal of Chemical Physics ARTICLE scitation.org/journal/jcp

Towards a transferable design of solid-state embedding models on the example of a rutile TiO_2 (110) surface

Cite as: J. Chem. Phys. 151, 184114 (2019); doi: 10.1063/1.5125204
Submitted: 22 August 2019 • Accepted: 24 October 2019 •
Published Online: 14 November 2019

View Online Export Citation CrossMark

M. Kick and H. Oberhofer[a)]

AFFILIATIONS

Chair for Theoretical Chemistry and Catalysis Research Center, Technical University of Munich, Lichtenbergstr. 4, 85747 Garching, Germany

[a)]Electronic mail: harald.oberhofer@tum.de

ABSTRACT

In this work, we present general and robust transferable principles for the construction of quantum-mechanically treated clusters in a solid-state embedding (SSE) approach, beyond the still prevalent trial and error approach. Thereby, we probe the quality of different cluster shapes on the accuracy of chemisorption energies of small molecules and small polaron formation energies at the rutile TiO_2 (110) surface as test cases. Our analyses show that at least the binding energies and electronic structures in the form of the density of states tend to be quite robust already for small, nonoptimal cluster shapes. In contrast to that, the description of polaron formation can be dramatically influenced by the employed cluster geometry possibly leading to an erroneous energetic ordering or even to a wrong prediction of the polaronic states themselves. Our findings show that this is mainly caused by an inaccurate description of the Hartree potential at boundary and surrounding atoms, which are insufficiently compensated by the embedding environment. This stresses the importance of the cluster size and shape for the accuracy of general-purpose SSE models that do not have to be refitted for each new chemical question. Based on these observations, we derive some general design criteria for solid state embedded clusters.

Published under license by AIP Publishing. https://doi.org/10.1063/1.5125204

I. INTRODUCTION

Studying chemical reactions on nonmetallic surfaces, the theoretical toolbox essentially offers two distinct approaches, the slab approach based on periodic boundary conditions (PBCs)[1] and the family of nonperiodic cluster models of the surface.[2,3] Thereby, the former naturally captures all long-range effects of, e.g., the electrostatic potential, in efficiently small unit-cells. At the same time, though, it suffers from considerable finite-size effects due to spurious interactions of nonperiodicities such as defects or possibly even just adsorbates.[4] This problem is exacerbated for charged nonperiodicities, such as localized charge carriers in the form of small polarons, where sometimes exceedingly large unit-cells are necessary in order to compensate for these errors.[5,6] Yet, it is precisely these nonperiodicities that often critically define a material's surface chemistry.[7] At the same time, many of the chemically most interesting materials demand the use of more accurate methods than simple semilocal density functional theory (DFT). Right now, most of these modern higher-rung techniques such as (double-) hybrid functionals tend to either be very costly[8–10] or—like most wave-function based techniques such as coupled cluster—nearly impossible to apply in PBCs.[11,12]

For these reasons, surface cluster models have remained a popular approach to simulating surface reactions.[3,13–21] The obvious drawback there is the lack of long-range interactions beyond the quantum mechanically (QM) treated cluster. Borrowing ideas from the field of theoretical biochemistry,[14] the cluster is therefore often surrounded by a—potentially very large—shell of molecular mechanical (MM) point charges restoring the long range electrostatics in an approach known as solid-state embedding (SSE).[22,23] Being a nonperiodic surface model, SSE does not suffer from spurious interactions by construction but, compared to the elegant

Published under license by AIP Publishing

simplicity of PBC approaches, shows considerable ambiguity due to the shape of the cluster and generally the interface between QM and MM regions.[2]

In the literature, one can find unqualified successes of both approaches, regarding, e.g., binding energies of adsorbates or even stabilities of (charged) defects.[3,9,24–32] Nevertheless, all SSE models so far always needed to be carefully tuned to a specific problem.[9] This means that for each material, surface termination, and even each specific chemical question—such as surface adsorption or surface defect formation—a new cluster model needed to be constructed[3] in order to yield useful results. Depending on the respective material, this could be more or less straightforward.[20] Usually, one needs to keep the cluster stoichiometry aligned with that of the underlying material to avoid spurious charging of the model and resulting offsets of the electrostatic potential. Furthermore, in more strongly ionic systems, the cluster should be symmetric to avoid low order multipole moments distorting the potential of the model. Scientists thereby mostly relied on highly simplified design paradigms such as round, hemispherical shapes to minimize the cluster's surface area,[3,33] paired with a lot of trial and error. The quality of a cluster is thereby often compared to periodic references,[12,16] which are not necessarily always available for the respective system.

Focusing on the chemistry of a rutile TiO_2 (110) surface, in this work, we first derive robust design rules for general-purpose SSE cluster models. On the one hand, we show that binding energies and electronic structures in the form of densities of states (DOSs) seem to be quite benign and easily reproduced already with small cluster sizes and nonoptimal cluster shapes. Yet, turning toward photoelectrochemistry, one of the most thoroughly studied use-cases of TiO_2, we find the reaction defining energetics of surface and subsurface polarons, forming due to a surface oxygen vacancy, to be a much harder problem for the SSE approach. Given that polarons crucially depend on not only a correct description of the material's electronic structure and local electrostatic potential but also the response of the surroundings of the material,[34] results strongly depend on both the cluster size and shape. We analyze in detail the reasons why some cluster shapes fail to reproduce periodic references in order to extract robust design criteria, allowing future SSE model construction beyond trial and error.

II. METHODOLOGY

A. QM/MM setup

All our calculations are based on the solid-state QM/MM approach developed by Berger and co-workers,[9,16] based on earlier work by Metz and co-workers.[22,23] Here, a small region of interest is treated fully quantum mechanically (QM) on the level of DFT. This QM-region is then embedded into a much larger polarizable molecular mechanics (MM) region. While the QM-region is only large enough to describe all relevant local contributions to the physical and chemical properties of interest, the MM region needs to account for all remaining long-range influences onto the local region. In the TiO_2 (110) surface models studied here, these influences are mostly comprised of electrostatic contributions, such as the long-range electrostatic potential and any dielectric responses of the environment to changes in the charge distribution of the QM-region. Regarding the crucial interface between QM- and MM-regions, in this approach, all positively charged Ti-ions in the vicinity of the QM-region are replaced by norm-conserving pseudopotentials (PPs) to avoid electron leakage to the otherwise bare coulomb singularities present in the MM-region. Finally, point charges are placed at the outer boundary of the MM-region. The values of these charges are fitted to reproduce the electrostatic potential of the infinite surface.[22,23] Following this approach, we achieve rms errors in the electrostatic potential between 10^{-4} and 10^{-5} V.

In order to achieve a most seamless transition between QM-region and MM-region, the applied interatomic MM potential should match the dielectric properties of the QM-region to avoid spurious dielectric interfaces within the material. Furthermore, the force-field description in the MM-region should largely match the QM lattice constants to avoid erroneous confinement stresses during geometry relaxation of the QM-region.[9] In the QM-region, both of these properties heavily depend on the applied exchange-correlation (XC) functional, which means that, in principle, one specifically needs to adapt the force-field to every functional.

Finally, the fact that the oxygen ions in TiO_2 are highly polarizable provides another challenge to the employed force-field. A simple rigid ion model would not be able to capture the dielectric properties of the material. Instead, one has to employ polarizable models—in our case, in the form of the popular core-shell force-field[35]—for the description of the MM-region.[16] Self-consistent polarization of the MM-region is then achieved by a series of micro-iterations,[9,22,23] guaranteeing a correct response to changes in the QM-region.

1. Periodic reference calculations for finite cluster models

To obtain the finite cluster models, we closely follow the strategy proposed by Berger and co-workers.[9,16] Based on optimized bulk unit cells, a surface slab is generated for every relevant DFT functional. In detail, c(1 × 1) supercell (110) surface slabs are created, consisting of five O-Ti_2O_2-O trilayers. For all calculations, the slabs are separated by 50 Å vacuum to avoid spurious interactions between periodic images. Furthermore, the periodic slabs are electronically decoupled by a dipole correction.

Numerical convergence is achieved with standard *tight* settings for atom-centered integration grids and the basis set, within the FHI-aims[36] program package. These settings were found to be comparable to or even more accurate than triple-ζ valence polarized gaussian type basis sets.[37] The k-space is sampled using an 8 × 8 × 8 Monkhorst-Pack grid for bulk geometries and an 8 × 8 × 1 grid for surfaces.[38] The top and bottom trilayers are fully relaxed until residual forces are below 10^{-3} eV/Å. The thus obtained surface structures then define the positions of the Ti and O atoms in the later embedded cluster calculations.

2. DFT and DFT+U calculations

All DFT calculations within this work have been carried out using the all electron code FHI-aims.[36] Calculations, such as the localization of excess charges as polarons, that demanded an improved treatment of the electronic structure were performed with the DFT+U variant[39,40] of Perdew-Burke-Ernzerhof (PBE) exchange-correlation functional. Following our earlier work,[34] the

Published under license by AIP Publishing

+U correction is thereby applied to the Ti atomic like 3*d* basis functions, while double counting of electron-electron interactions was corrected in the—*de-facto* standard[25,41–43]—fully localized-limit (FLL).[44] For all DFT+U related calculations, the on-site definition of the occupation matrix is used.[45] To ensure a better comparability with our earlier work on periodic TiO_2 slabs,[34] all DFT+U calculations here have been conducted with a *U* value of 2.65 eV. This *U* value has been fitted to reproduce the experimentally observed defect state, which lies about 1 eV below the conduction band minimum.[46]

For all studies of adsorption behavior in our SSE models, we used the revised Perdew-Burke-Ernzerhof (RPBE) exchange-correlation functional, considered to yield much more accurate adsorbtion energies for TiO_2 compared to standard PBE.[47] However, we also checked our results with the above described DFT+U setup to find the same trends among different clusters.

B. Interatomic potential for cluster geometries

Polarizability of the MM region is modeled using a core-shell type additive pair-potential. Thereby, oxygen ions are represented by two point charges with opposite signs, connected by a spring, where one point charge represents the nucleus and the other represents the ion's valence electron density. In order to avoid inconsistencies with the PPs saturating the QM-region, the total charges of both oxygen, that is, the sum of core and shell particles, and titanium atoms are constrained to the formal charges of $-2e$ and $+4e$, respectively. Finally, nonelectrostatic interactions between oxygen shells and between oxygen shells and Ti cores are modeled by Buckingham pair-potentials,[48]

$$V_{x-x} = A \exp\left(-\frac{d_{x-x}}{\rho}\right) - \frac{C}{d_{x-x}^6}. \quad (1)$$

Here, *d* is the distance between the interacting species and *A*, *ρ*, and *C* are the potential parameters. Overall, this leads to nine parameters, i.e., the strength of the core-shell spring, the respective Buckingham parameters for O and Ti, and the charge on the oxygen shells, which need to be adapted to the given description of the QM-region. In our earlier work, we provided force-field parameters fitted to comply with generalized-gradient-approximation (GGA) and hybrid functional descriptions of rutile TiO_2.[9,12] Given that these are not necessarily appropriate for use with the PBE+U-corrected functional applied in this study, we here performed a refit of the force-field parameters following the procedures outlined in earlier work.[9]

Unfortunately, the FHI-aims code does not provide access to dielectric tensor components for bulk materials. Also, no reference values for PBE+U could be found in the literature. However, one can expect the dielectric tensor components—which in TiO_2 show considerable anisotropy—to show values comparable to those obtained for PBE or hybrid functionals. Therefore, we chose the high-frequency components of the PBE dielectric tensor and the periodic PBE+U lattice constants as target values for the force-field fitting procedure. All target properties are listed in Table I, while the optimized parameters of the resulting MM-potential are given in Table II.

TABLE I. Bulk rutile TiO_2 lattice constants a and c, as well as the corresponding high frequency dielectric tensor components ε_∞^a and ε_∞^c. Shown are both the target DFT values for force-field parametrization and the obtained MM values.

	a (Å)	c (Å)	ε_∞^a	ε_∞^c
PBE+U	4.626	2.971	6.94[49]	8.22[49]
MM	4.6296	2.977	6.94	8.22

TABLE II. Optimized force-field parameters for the Buckingham potentials and the core-shell model. Here, *k* and *r* are describing the shape of the spring potential. *q* is the charge of the oxygen shells. *A*, *ρ*, and *C* are denoting the Buckingham potential parameters for shell-shell (s-s) and shell Ti-core (s-Ti) interactions. For more details on the specific fitting procedure, the reader is referred to Ref. 9.

	k	*r*	*q*
	9.26	0.089	−2.8319
	A	*ρ*	*C*
s-s	24 890	0.1742	50.92
s-Ti	1 975	0.3195	22.27

It should be highlighted that, in principle, a refit of the force-field parameters has to be done for each applied DFT functional. This is due to different DFT functionals yielding slightly different lattice parameters, leading to potential mismatches with the MM region which should, in general, be avoided whenever possible. This means for RPBE geometries, one has to apply different force-field parameters and also has to repeat the procedure for obtaining the cluster models. We therefore used the same force-field parameters for RPBE as applied in a previous study of our group.[12] The force-field parameters therein have been constructed in exactly the same way as described before. All newly generated cluster geometries have been fully relaxed with these optimized parameters.

III. RESULTS AND DISCUSSION

In order to gauge the quality of the solid state embedding approach with a specific view on the influence of the cluster shape, we perform two distinct types of tests. First, we assess the suitability of embedded cluster models for molecular adsorption studies by comparing PBC and cluster results of the adsorption energy of an OOH-radical, OH-radical, and H_2O, which are important species in the photoelectrocatalytic water oxidation reaction.[50,51] As this example turned out to be rather insensitive to the details of the embedding, we then move on to a much more stringent test for the embedded cluster approach in the form of polaron formation near a surface oxygen vacancy. Being charge carriers localized through the polarization of their surroundings, polarons are highly sensitive both to the employed electronic structure method and the description of the environment.[34] Their formation energies thus represent good descriptors for the qualities of the embedded cluster models. Based on this quality measure, we then analyze the reasons for the success or failure of a given cluster model. To this end, we compare their respective electrostatic potentials, densities of states, and frontier orbital geometries to periodic references. This insight, finally, allows us to formulate general design criteria for embedded cluster shapes.

Published under license by AIP Publishing

A. Cluster models for molecule adsorption

On rutile TiO_2 (110), most small, chemisorbed adsorbate molecules bind to five-fold coordinated surface Ti atoms.[12,28,29,52] Embedded clusters targeted at adsorption studies are thus best centered on such a Ti atom, centering the adsorbate in the QM region and keeping boundary effects due to imperfect embedding at a minimum. Furthermore, the QM regions have to show the correct stoichiometry of TiO_2. None of stoichiometric clusters would then lead to an artificial creation of Ti^{3+} centers differing clearly from the situation of pristine TiO_2. This consideration already determines, up to a certain degree, how a cluster model, in principle, has to be designed. Obviously, the cluster termination is those mainly dominated by oxygen atoms as otherwise the right stoichiometry cannot be achieved.

In Fig. 1, we present six such models which mainly differ in their size and shape, ranging from a rather small cluster consisting of 17 titanium and 34 oxygen atoms up to a cluster with a total of 168 atoms ($Ti_{58}O_{116}$), where the $Ti_{17}O_{34}$ and $Ti_{29}O_{58}$ cluster models have been taken from Ref. 3. The clusters thus not only increase in their size but also vary in their shapes—$Ti_{17}O_{34}$ and $Ti_{29}O_{58}$ are spherically shaped compared to the other four cluster models which show a more cubic structure.

Our earlier study of physisorption of closed-shell molecules (such as NH_3, CH_3, and H_2O) on TiO_2 SSE models[12] showed that these adsorbates are largely insensitive to the size and shape of the embedded cluster for a wide range of DFT functionals and even highly accurate embedded CCSD(T) quantum-chemical reference calculations. This is not at all surprising, given that such molecules tend to be bind only weakly to the surface in the first place. While this insensitivity is definitely a good first sign for the accuracy of our embedding model, the physisorption of small molecules on TiO_2 is not the most pressing of computational problems. With an eye on the catalytic activity of the material, we thus turn to much more strongly chemisorbed species, relevant for water oxidation and photo-oxidation reactions.[28] Specifically, we calculate the adsorption energies of OH, OOH, and H_2O, compared to the relevant periodic references. The adsorbates' binding energies are thereby calculated according to

$$E_{\mathrm{ads}} = E_{\mathrm{tot}}(\mathrm{TiO_2}(110) + \mathrm{ads}) - E_{\mathrm{tot}}(\mathrm{ads}) - E_{\mathrm{tot}}(\mathrm{TiO_2}(110)), \quad (2)$$

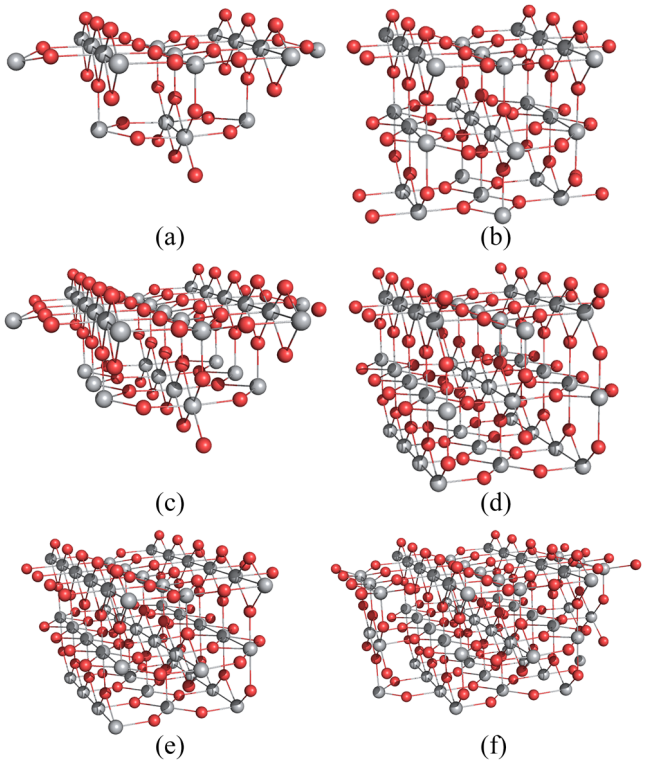

FIG. 1. Differently sized Ti-centered cluster models for adsorption studies: (a) $Ti_{17}O_{34}$, (b) $Ti_{28}O_{56}$, (c) $Ti_{29}O_{58}$, (d) $Ti_{38}O_{76}$, (e) $Ti_{44}O_{88}$, and (f) $Ti_{56}O_{112}$.

where $E_{\mathrm{tot}}(\mathrm{TiO_2}(110) + \mathrm{ads})$ denotes the total energy of the surface with adsorbed species, $E_{\mathrm{tot}}(\mathrm{ads})$ is the total energy of the gas phase molecule, and $E_{\mathrm{tot}}(\mathrm{TiO_2}(110))$ is the energy of the pristine surface. At this stage, all energies are calculated with the RPBE exchange correlation functional.[47] For the gas phase reference, we considered the corresponding stand alone neutral adsorbate molecule. Enabling surface relaxation could lead to errors due a possible wrong relaxation behavior of the boundary atoms as this might be more influenced by a possible embedding error. Especially for smaller clusters,

TABLE III. Adsorption energies for OOH, OH, and H_2O chemisorbed on a rutile TiO_2 (110) surface with (scf-pol) and without (no scf-pol) self-consistent shell polarization. Also shown are the results for a periodic reference calculation using a 5 × 2 surface supercell.

	E_{ads}^{OOH} (eV)		E_{ads}^{OH} (eV)		$E_{ads}^{H_2O}$ (eV)	
System	scf-pol	no scf-pol	scf-pol	no scf-pol	scf-pol	no scf-pol
$Ti_{17}O_{34}$	−0.24	−0.25	−0.69	−0.70	−1.78	−1.81
$Ti_{28}O_{56}$	−0.28	−0.24	−0.75	−0.72	−1.85	−1.80
$Ti_{29}O_{58}$	−0.25	−0.23	−0.71	−0.70	−1.83	−1.80
$Ti_{38}O_{76}$	−0.25	−0.23	−0.73	−0.71	−1.84	−1.80
$Ti_{44}O_{88}$	−0.24	−0.22	−0.72	−0.70	−1.82	−1.78
$Ti_{56}O_{116}$	−0.24	−0.23	−0.72	−0.70	−1.84	−1.81
c(5 × 2) PBC	−0.21		−0.71		−1.76	

Published under license by AIP Publishing

this can be critical. Therefore, focusing on the influence of the SSE approach on the electronic properties of the embedded system, we here neglect surface relaxation due to adsorption of the molecules.

The results of this procedure, compared to the respective results of a PBC calculation using a 5 × 2 supercell, are shown in Table III. Furthermore, we also show results without self-consistent polarization of the oxygen shells in the MM-region, that is, with shells fixed at the equilibrium position of the pristine MM surface.

We find very little dependence on the cluster size. Already the smallest of our cluster models quite faithfully reproduces the adsorption energetics of the periodic reference, well within the error of the underlying DFT functional. Furthermore, for each cluster, we found self-consistent polarization to contribute little to the adsorption energies. Overall, we thus find adsorption energetics even of a radical to still be a rather insensitive test of cluster suitability. While this seems to show that any cluster size or shape could be used in a QM/MM calculation, we find this not to be the case as we will demonstrate on the more stringent example of polaron formation in Sec. III B.

We note, however, that we here restricted ourselves to the adsorbtion of single molecules at the center of the cluster. This way, potential boundary effects of the cluster are largely minimized. It is therefore easily possible that more complicated adsorption geometries involving, e.g., larger molecules or dissociative adsorption could show a stronger dependence on embedded cluster shape

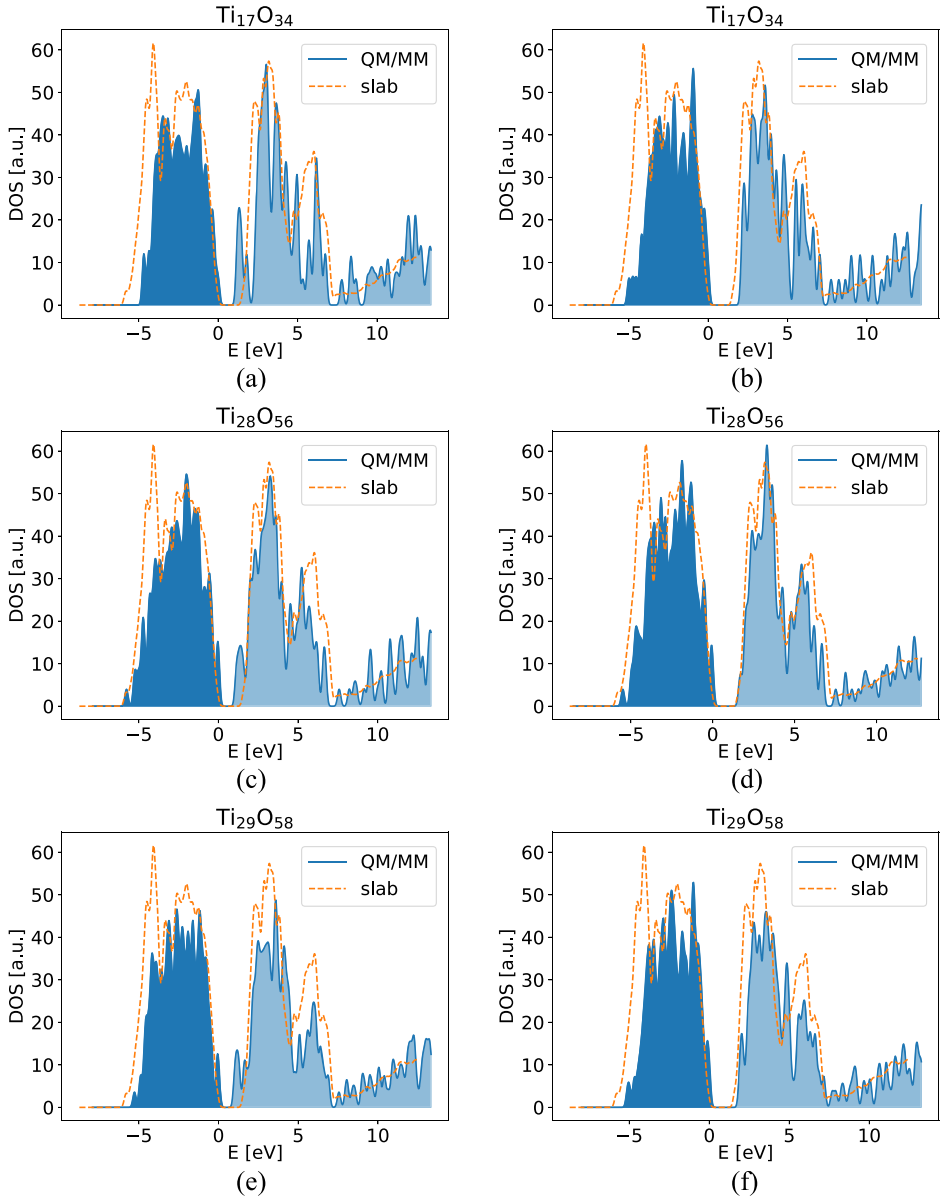

FIG. 2. DOS plots for the three smallest suggested Ti-centered cluster models: $Ti_{17}O_{34}$ [(a) and (b)], $Ti_{28}O_{56}$ [(c) and (d)], and $Ti_{29}O_{58}$ [(e) and (f)]. Shown are the DOS with [left column: (a), (c), and (e)] and without [right column: (b), (d), and (f)] self-consistent polarization of the oxygen shells. For comparison, the DOS of a slab reference calculation is shown in orange in each plot. For all calculations, the RPBE functional has been used. To align periodic and cluster calculations, the VBM serves as zero of the energy scale. The DOS plots of the remaining Ti-centered cluster models are shown in Fig. 3.

Published under license by AIP Publishing

and size. Such cases are likely going to demand larger clusters. Furthermore, as we do not consider surface relaxation and due to the fact that we are using a GGA functional, we are not able to capture the entire physics of even the single molecule adsorption process. Using functionals which aim to correct for the self-interaction error and allowing the surface to adapt to the adsorbed radical might yield a higher sensitivity of the adsorption energy regarding the general cluster shape.

1. The role of MM polarizability

Before going on to a more stringent test-case, the next important point to clarify is the role of the polarizable force-field in the MM region. While our results showed only minor influences of the surrounding polarization response onto adsorption energies, one would assume polar adsorbates to be stabilized by shell polarization.[16]

We thus systematically examine the influence of shell polarizability on a cluster's electronic structure by plotting the density of states of all six of our cluster models with and without self-consistent MM polarization in Figs. 2 and 3. We compare them to the DOS of a periodic reference calculation depicted in orange in Fig. 2 and in Fig. 3, respectively. Clearly, the DOS of the embedded clusters qualitatively resembles the periodic reference very well. Except for the smallest clusters ($Ti_{17}O_{34}$, $Ti_{28}O_{56}$, $Ti_{29}O_{58}$), where self-consistent polarization does play a significant role, the chemically important band edges are reproduced with remarkable accuracy. In the larger

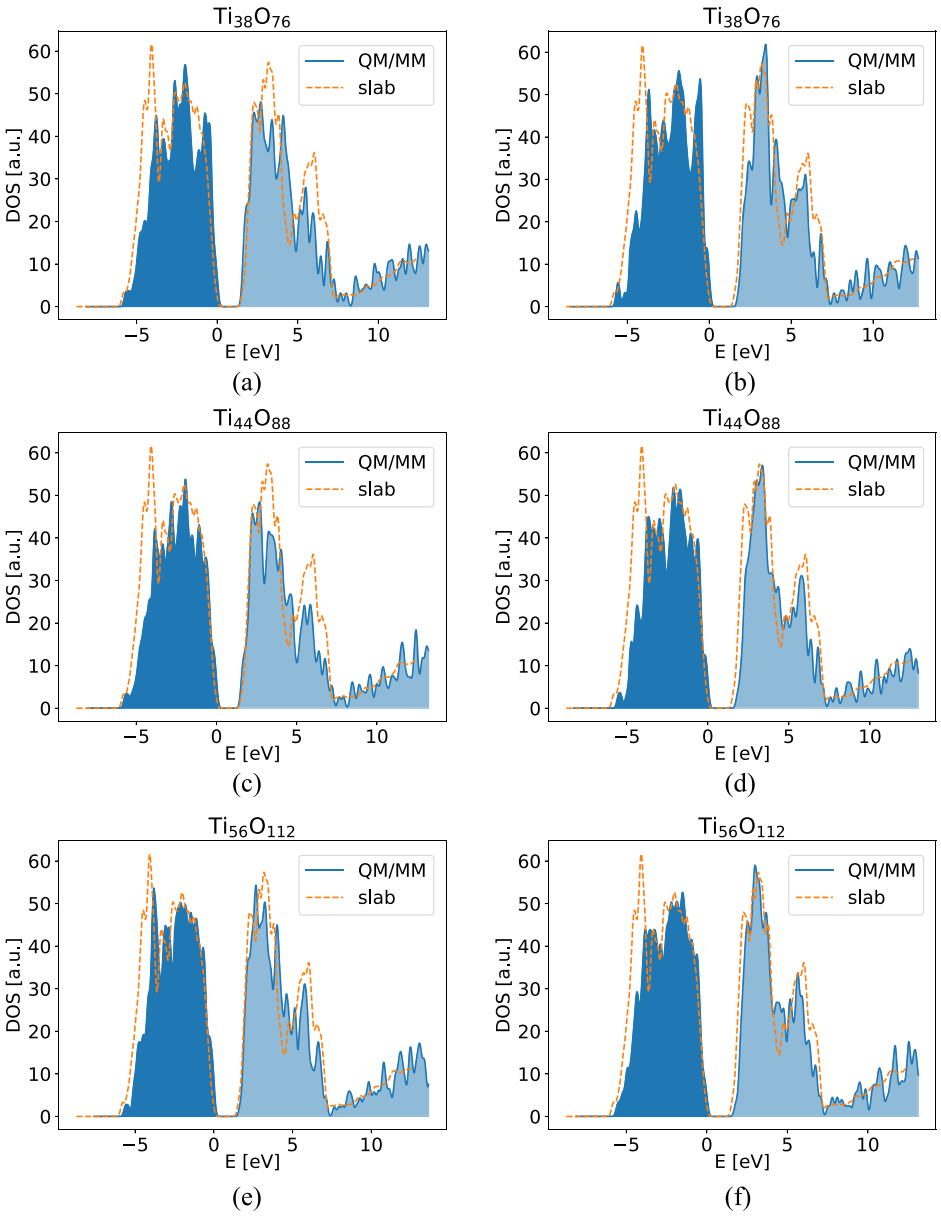

FIG. 3. DOS plots for $Ti_{38}O_{76}$ [(a) and (b)], $Ti_{44}O_{88}$ [(c) and (d)], and $Ti_{56}O_{112}$ [(e) and (f)]. Shown are the DOS with [left column: (a), (c), and (e)] and without [right column: (b), (d), and (f)] self-consistent polarization of the oxygen shells. For comparison, the DOS of a slab reference calculation is shown in orange in each plot. For all calculations, the RPBE functional has been used. To align periodic and cluster calculations, the VBM serves as zero of the energy scale. The DOS plots of the three smallest Ti-centered clusters are depicted in Fig. 2.

Published under license by AIP Publishing

clusters, self-consistent shell relaxation does further improve the agreement between embedded cluster and PBC results. Here, shell relaxation thus seems to compensate for some of the shortcomings of the embedded cluster approach. The smallest clusters do not seem to benefit from this compensation, showing a much worse DOS for self-consistent shells than otherwise. Due to the relatively large ratio of atoms at the QM/MM edge compared to interior atoms, $Ti_{17}O_{34}$, $Ti_{28}O_{56}$, and $Ti_{29}O_{58}$ do not seem to yield the correct QM charge distribution. The shoulders appearing near band edges are a result of energy shifts of the states that are mainly localized on cluster boundary atoms. They are caused by an erroneous description of the potential at the cluster boundary. In this case, shell polarization seems to lead to an enhancement of the error. This also explains why earlier studies on small embedded clusters showed a non-self-consistent approach to be optimal for the reproduction of the electronic structure.[9,12] A deeper investigation of the errors in the electrostatic potential will be presented in Sec. III B 1.

Nevertheless, Table III shows that even for the smallest clusters, E_{ads} was very close to the periodic reference. This is either a sign of fortuitous error cancellation or of the forgiving nature of our chosen observable. Instead of calculating other adsorption energies, we thus go on to a much more stringent test case in Sec. III B.

B. Vacancy induced polaron formation

In the literature, a number of studies highlight the complexities involved in modeling polaron formation induced by oxygen vacancies at the rutile TiO_2 (110) surface.[25,41,42] First, semilocal generalized gradient functionals were shown to not yield the necessary degree of electron localization due to the large amount of self-interaction error inherent to them. Second, even with hybrid functionals or DFT+U, the correct energetic ordering of different polaron configurations relative to the vacancy is highly sensitive to other factors such as the employed pseudopotentials or the projector functions used for the Hubbard U correction.[34,53,54] Finally, polarons are stabilized through the polarization response of their surroundings, which makes them an ideal test-case for the accuracy of our embedding approach.

In order to achieve symmetry with respect the position of the oxygen vacancy and thus minimize erroneous multipole moments of the cluster itself, embedded clusters suitable for the study of polaron formation are optimally centered on the oxygen vacancy. This corresponds to studying the defects in the dilute limit. Therefore, instead of the adsorption clusters introduced in Fig. 1, we here use two different clusters, presented in Fig. 4. Moreover, as known from the literature,[25] the most stable polaron configurations are located at the subsurface layer. In order to capture the correct physics, it is therefore necessary to have clusters with an appropriately sized subsurface structure.

From these pristine clusters, we then remove the central bridging oxygen atom, while leaving the surface overall charge neutral. Compared to the stoichiometric surface, this leaves two excess electrons which, after structure relaxation, form two small polarons, trapped around the defect site. These polarons can either be in a triplet state or open-shell singlet configuration.[25] More precisely, in the commonly applied nomenclature, an open-shell singlet configuration corresponds to a configuration where the amounts of electrons for spin up and spin down density are equal, yet spatial distributions differ. A triplet state, on the other hand, corresponds to a configuration where one of the spin channels contains two electrons more than the other.

Although trapped near the defect, these polarons can, in principle, localize at different Ti atoms throughout the system, giving rise to a large number of distinct polaron configurations. Yet, in general, most configurations show very similar energetics. On top of that, barriers between different polaronic configurations are generally small.[25] Both these properties tend to make an accurate sampling of polarons, a technically challenging task. As a remedy, we make use of the so-called matrix control approach,[55,56] where the DFT+U occupation matrix is kept fixed for all Ti atoms during the geometry optimization of a given polaron configuration. For Ti atoms where the excess charges should be localized, we simply set one of the diagonal entries of the corresponding matrix to one. This way, the corrective Hubbard potential in DFT+U acts like a bias potential, not unlike the constrained DFT approach,[57,58] ensuring localization of the electron at the desired site. In a second run, we then use the obtained structures and restart information to perform further relaxations without constraining the occupation matrix. This way we achieve full self-consistency of our results.

We adopt the same systematic nomenclature of polaron configurations as used in Ref. 34. In this convention, the surface layers are marked with the letter "S" followed by the atom number on which the excess electron is located. We illustrate this nomenclature, adapted to our cluster models, in Fig. 5. Due to the finite sizes of our clusters, we are not able to sample the entire range of different localization patterns, especially for the smaller $Ti_{46}O_{92}$. Instead, we choose four representative polaron configurations for the rutile TiO_2 (110) surface. This way we can capture two different subsurface configuration (S1-4/S1-11, S1-3/S1-11), two polarons located directly at the surface (S0-3/S0-6), and a configuration where one polaron is directly centered at the defect site and one directly below the defect

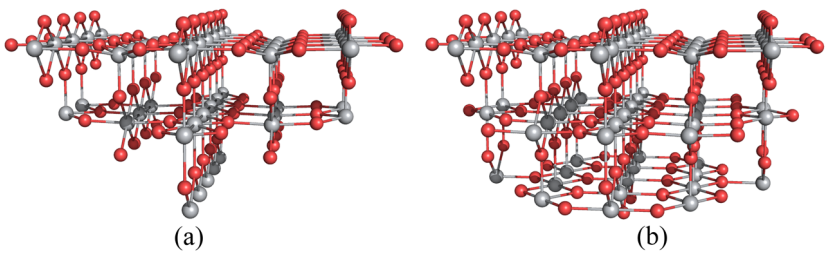

FIG. 4. Defect-free TiO_2 (110) surface cluster models [(a) $Ti_{46}O_{92}$, (b) $Ti_{60}O_{120}$] for vacancy and polaron formation studies. Ti atoms are shown as gray spheres, and oxygen atoms are shown as red spheres. The surface oxygen vacancies were created by removing one of the bridging oxygen atoms in the cluster center. The $Ti_{46}O_{92}$ cluster model was initially suggested in Ref. 3.

Published under license by AIP Publishing

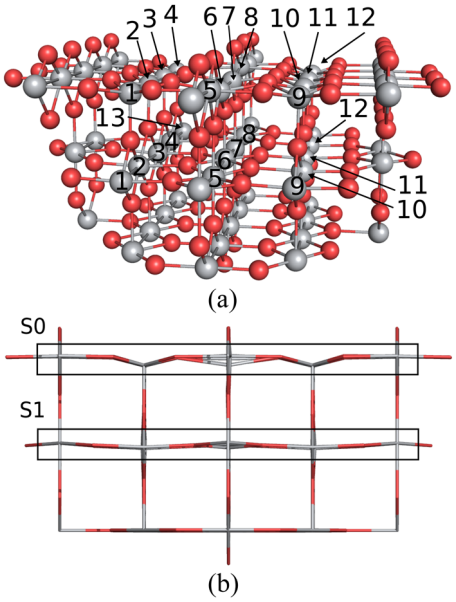

FIG. 5. Illustration of the site naming convention for polaron configurations in the $Ti_{60}O_{120}$ model. In (a), the Ti atoms are numbered within a surface layer. In (b), the relevant surface layers are labeled by S0 for the first layer and by S1 for the second layer. The same numbering scheme also applies to the $Ti_{46}O_{92}$ cluster model and the periodic slab reference.

site in the center of the QM-region (S0-7/S1-7). We start our analysis by calculating the relative stabilities of the different configurations, given by

$$E_{\mathrm{rel}} = E^{i}_{\mathrm{QM/MM}} - E^{0}_{\mathrm{QM/MM}}. \tag{3}$$

Here, $E^{i}_{\mathrm{QM/MM}}$ is the total energy (QM and MM contributions) of a given configuration i and $E^{0}_{\mathrm{QM/MM}}$ is the total energy of the most stable configuration, which—again following common convention[25,41]—serves as our energy zero. This allows us to compare our results not only between different cluster models but also between the used QM/MM setup and periodic calculations. It should be pointed out that no long-range electrostatic correction has been

TABLE IV. Relative polaron stabilities in eV. They have been calculated according to Eq. (3) for the two embedded cluster models ($Ti_{46}O_{92}$ and $Ti_{60}O_{120}$) and a periodic reference (PBC). The most stable configuration is taken as the energy zero. Other, less stable polaron configurations thus show positive relative energies. σ denotes the spin state of the system, which can be either a triplet (t) or an open-shell singlet (s) configuration. The convention and naming of the different polaronic configurations were taken from Ref. 34.

System	Ti_{46}	Ti_{60}	PBC	σ
S1-4/S1-11	...	0.0	0.0[a]	s
S1-3/S1-11	...	−0.19	6×10^{-3}[a]	s
S0-7/S1-7	...	1.29	1.22[a]	s
S0-3/S0-6	0.00	1.23	1.14	s
S0-3/S0-6	0.00	1.23	1.14	t

[a]Results marked with "superscript a" were taken from Ref. 34.

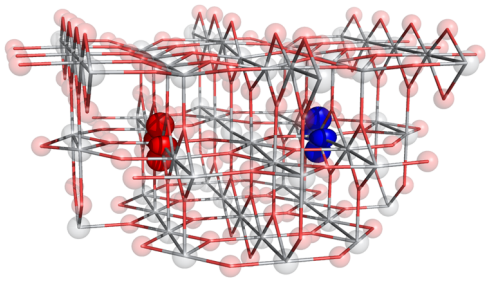

FIG. 6. Spin up (red) and spin down density (blue) of S1-3/S1-11 within the $Ti_{60}O_{119}$ embedded cluster model. Isosurface value 0.015 eÅ^{-3}.

applied, as earlier work[9] showed that results are already well converged with the self-consistent polarization response, at least for neutral defect systems.

Earlier works on polaron localization in TiO_2[25,41] showed the open-shell singlet configuration to be the energetically most stable one. Therefore, we concentrate most of our efforts here on the energetics of open-shell singlet spin polarons. In contrast, however, earlier embedded cluster calculations by Berger *et al.*[9] reported the

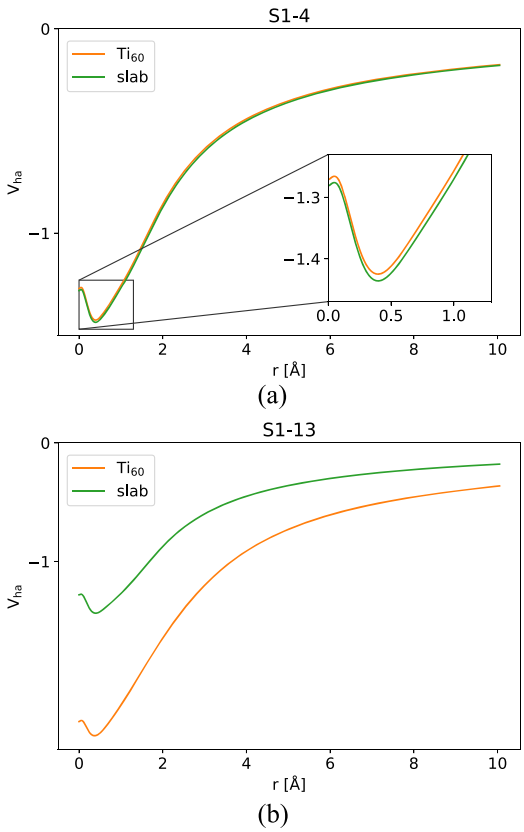

FIG. 7. Monopole ($l = 0$) component of the Hartree potentials of Ti atoms at S1-4 (a) and S1-13 (b) in the $Ti_{60}O_{120}$ cluster model (orange). The corresponding potentials from a periodic reference calculation are reproduced in green. Here, r is uniform in all directions.

Published under license by AIP Publishing

(S0-3/S0-6) triplet configuration to be even more stable. While this could have been a size effect of the employed cluster models, we do not rule out this possibility and also include this configuration's triplet state into our analysis. The relative stabilities calculated in both cluster models are given in Table IV.

1. Results compared to PBC references

In the $Ti_{46}O_{92}$ cluster, we were not able to find any other polaronic configuration besides S0-3/S0-6. Even taking the self-consistent DFT+U correction from the larger $Ti_{60}O_{120}$ as a constraint, none of the other target configurations were found. While this is somewhat consistent with earlier embedded cluster results,[9] $Ti_{46}O_{92}$ is clearly not suitable for quantitative studies of polaron stabilities. This is easily arguable, as $Ti_{46}O_{92}$ does not yield the polaron configurations as one yields using a PBC approach. We will address the mechanisms for the failure of this cluster in Sec. III B 2 in order to extract the design criteria behind successful embedded cluster models.

In the $Ti_{60}O_{120}$ cluster, all five polaron configurations were found to be stable. As a showcase, Fig. 6 shows the obtained spin density of S1-3/S-11. In contrary to conventional PBC, though, where the configurations S1-3/S1-11 and S1-4/S1-11 were degenerate, the cluster model showed S1-3/S1-11 to be more stable by roughly 0.2 eV. This discrepancy can be explained by observing that single polarons in TiO_2 are not entirely located at single Ti atoms but are slightly delocalized toward neighboring Ti and O atoms.[41] In a cluster approach, these neighboring atoms might already be located at the edge of the QM region, which—due to an imperfect embedding—can suffer from a degraded description of the local electronic structure, compared to the cluster interior. In order to shed more light on this error, we depict in Fig. 7 the monopole component of the Hartree potential for the Ti atoms located at the off center S1-4 position [Fig. 7(a)] and the S1-13 boundary position [Fig. 7(b)] of the $Ti_{60}O_{120}$ model. Note that in FHI-aims, the full electrostatic potential is treated as a multipole moment expansion, yet with radial dependencies splined on a logarithmic grid for improved accuracy. The monopole components plotted in Fig. 7 are these radial functions for $l = 0$, with l being the angular momentum quantum number. Given that the energy of a localized charge is to a large degree determined by the local electrostatic potential, polarons represent a very sensitive probe to the accuracy of the reproduction of the Hartree potential in an embedded cluster. Ideally, the Hartree potential of an embedded cluster should exactly match that from a PBC calculation. However, this only holds true for the atoms within the cluster, such as, e.g., the Ti atom at S1-4. On the contrary, the Hartree potential at the edge (S1-13) differs quite a lot from the corresponding potential of a PBC reference calculation. This explains the energetic discrepancies of polaron configuration S1-4/S1-11 compared to PBC as the polaron at S1-4 shows a partial delocalization toward S1-5. Of course, an erroneous description of the S1-4/S1-11 configuration will cause an offset in all other relative stabilities and limits the comparability with the PBC approach. However, even with pinning the energy scale to the S1-3/S1-11 configuration, we still obtain a small offset of around 0.1 eV between $Ti_{60}O_{120}$ and the supercell calculation. It should be

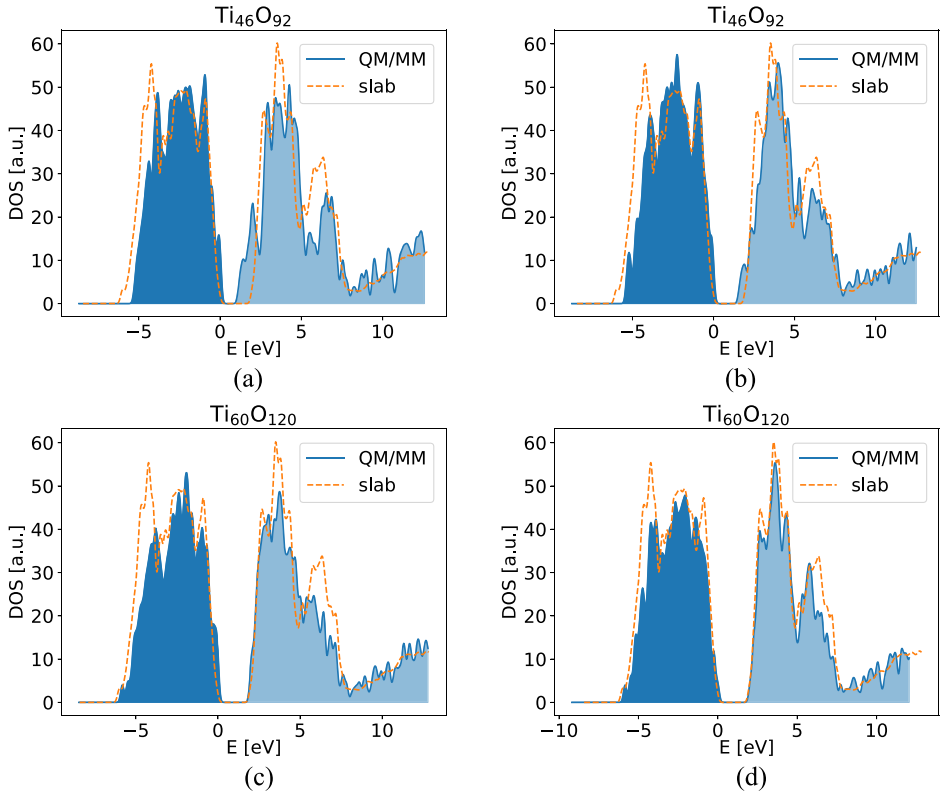

FIG. 8. Density of states of $Ti_{46}O_{92}$ [(a) and (b)] and $Ti_{60}O_{120}$ [(c) and (d)] with [on the left, (a) and (c)] and without [on the right, (b) and (d)] self-consistent polarization of the oxygen shells. Displayed are both the DOS of the embedded cluster calculation (blue) and the DOS of the periodic slab reference (dashed orange line). For both embedded cluster and slab reference calculation, a U value of 2.65 eV was employed. The VBM serves as zero for the energy scale.

Published under license by AIP Publishing

pointed out that this difference is not caused by differing orbital configurations of the polarons as both PBC and embedded cluster results show identical orbital occupations. One possible reason for the remaining difference could result from possible finite size effects in the QM/MM setup. Especially for the subsurface polaron configuration, an even larger cluster model might be necessary to capture the entire reorganization energy. Nevertheless, given that the energy discrepancies are quite small, we conclude that our QM/MM setup is, in fact, capable of describing even ultrasensitive systems such as polarons, at least for large enough cluster models and if the polarons in question are located far enough from the cluster boundary.

2. Difference between the cluster models

The question now remains, why the two cluster models studied here show such a difference in performance with respect to polaron localization. At first glance, it would seem that the $Ti_{46}O_{92}$ cluster model is simply too small. Earlier studies[41] showed that each polaron state also has contributions from neighboring basis functions, which for the more peripherally localized polarons, such as S1-4/S1-11, could pose a serious problem. If this were the only reason, however, one should be able to localize the electrons in pattern S1-3/S1-11 or in pattern S0-7/S-7, as both electrons reside on Ti atoms well within the center of the cluster.

a. Density of states. We start our analysis by comparing the DOS of both bridging oxygen-centered cluster models with the corresponding slab reference in Fig. 8. For completeness, we again include both the DOS before and after self-consistent polarization of the oxygen shells. In the larger $Ti_{60}O_{120}$ cluster, the DOS quite accurately reproduces the periodic reference, both with and without self-consistent shell polarization. The $Ti_{46}O_{92}$ model, on the other hand, shows large deviations from the PBC DOS, especially at the band edges. This is the case even when no self-consistent polarization is applied, albeit less pronounced. Compared to our adsorption-optimized cluster models (cf. Sec. III A), $Ti_{46}O_{92}$ should be large enough to compensate for an imperfect embedding and should yield a DOS comparable in quality with the $Ti_{44}O_{88}$ cluster model. Instead, however, the performance regarding the $Ti_{46}O_{92}$ is closer to a much smaller cluster like $Ti_{28}O_{56}$.

b. Frontier orbital shape. Considering that the error in the DOS is most pronounced at the band edges, in a next step, we thus investigated the general shapes of the frontier orbitals of the used cluster models. Figure 9 shows the HOMO and LUMO calculated with a supercell approach. Widely known in the literature[41,43,59] and also confirmed by our calculations, the HOMO is dominated by a linear combination of oxygen 2*p* orbitals. In contrast, the LUMO is dominated by Ti 3*d* states. In the embedded $Ti_{46}O_{92}$, however, the situation is quite different. In this system, the HOMO is also dominated by oxygen 2*p* orbitals, but charge density tends to accumulate at the cluster boundary (Fig. 10). While the HOMO might be correct in a broad, qualitative sense, the LUMO shows a completely different shape compared to PBC, being entirely located at the bottom of the cluster. Thus, in $Ti_{46}O_{92}$, the electronic structure of even the defect-free system without polarons is already far from the periodic reference. At the same time, polaronic states are strongly influenced by both the energetic alignment of frontier orbitals[34] and their local

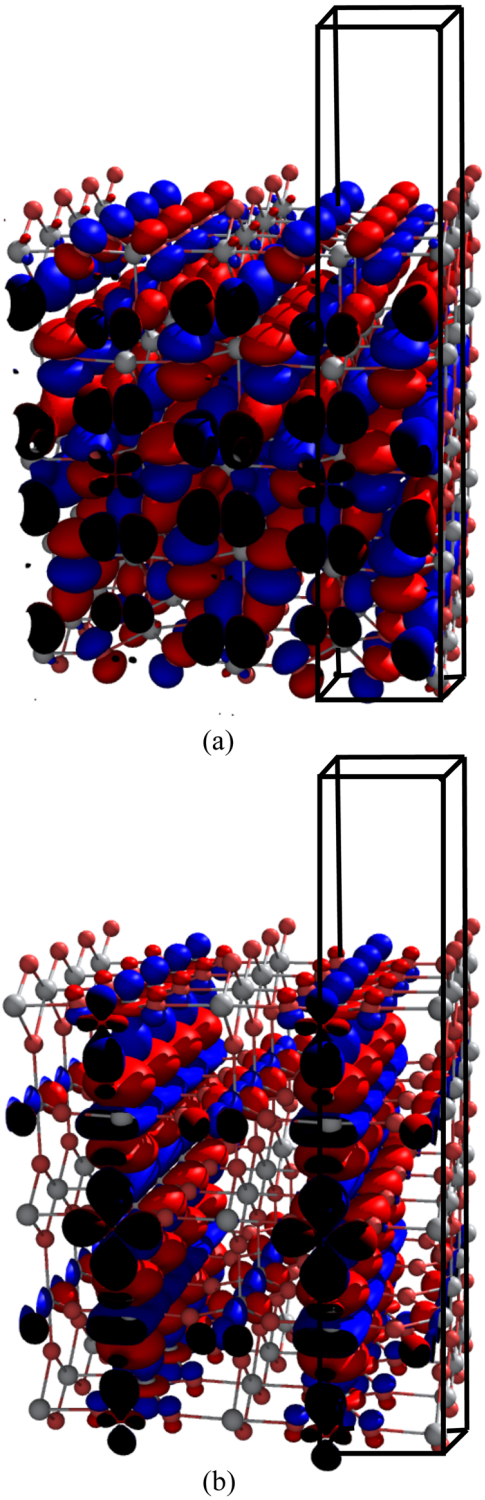

FIG. 9. HOMO (a) and LUMO (b) of the pristine periodic rutile TiO_2 (110) surface. The HOMO is dominated by a linear combination of oxygen 2*p* states, while Ti 3*d* orbitals determine the character of the LUMO. Isosurface value 0.015 eÅ^{-3}.

Published under license by AIP Publishing

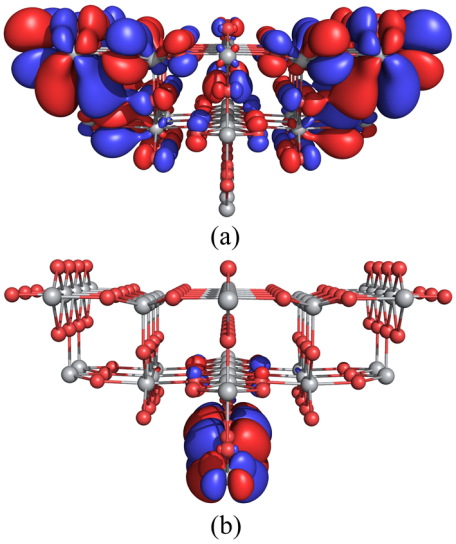

FIG. 10. HOMO (a) and LUMO (b) of the pristine $Ti_{46}O_{92}$ cluster model. For the HOMO, there is a tendency to accumulate charge at the cluster boundary. The LUMO shows unphysical localization at the bottom of the cluster. Isosurface value 0.015 eÅ^{-3}.

structure,[25] which partly explains the failure of $Ti_{46}O_{92}$. In comparison, the $Ti_{60}O_{120}$ cluster model renders both the HOMO and the LUMO shape of the periodic reference broadly correctly (Fig. 11). This is made possible by the cluster's more cubic shape compared

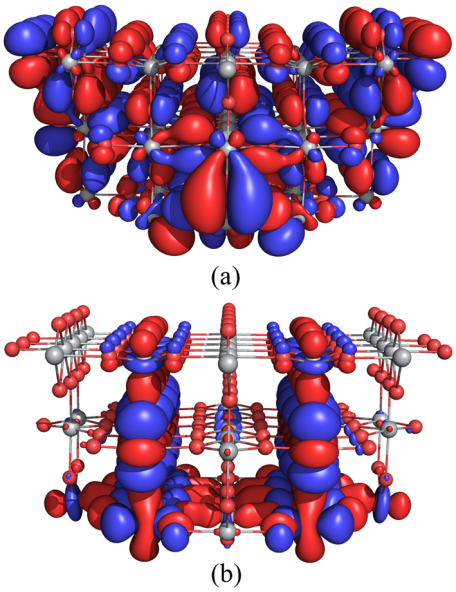

FIG. 11. HOMO (a) and LUMO (b) of the pristine $Ti_{60}O_{120}$ cluster model. In this model, both the shapes of HOMO and LUMO, respectively, resemble that of the PBC reference (Fig. 9) with remarkable accuracy. Isosurface value 0.015 eÅ^{-3}.

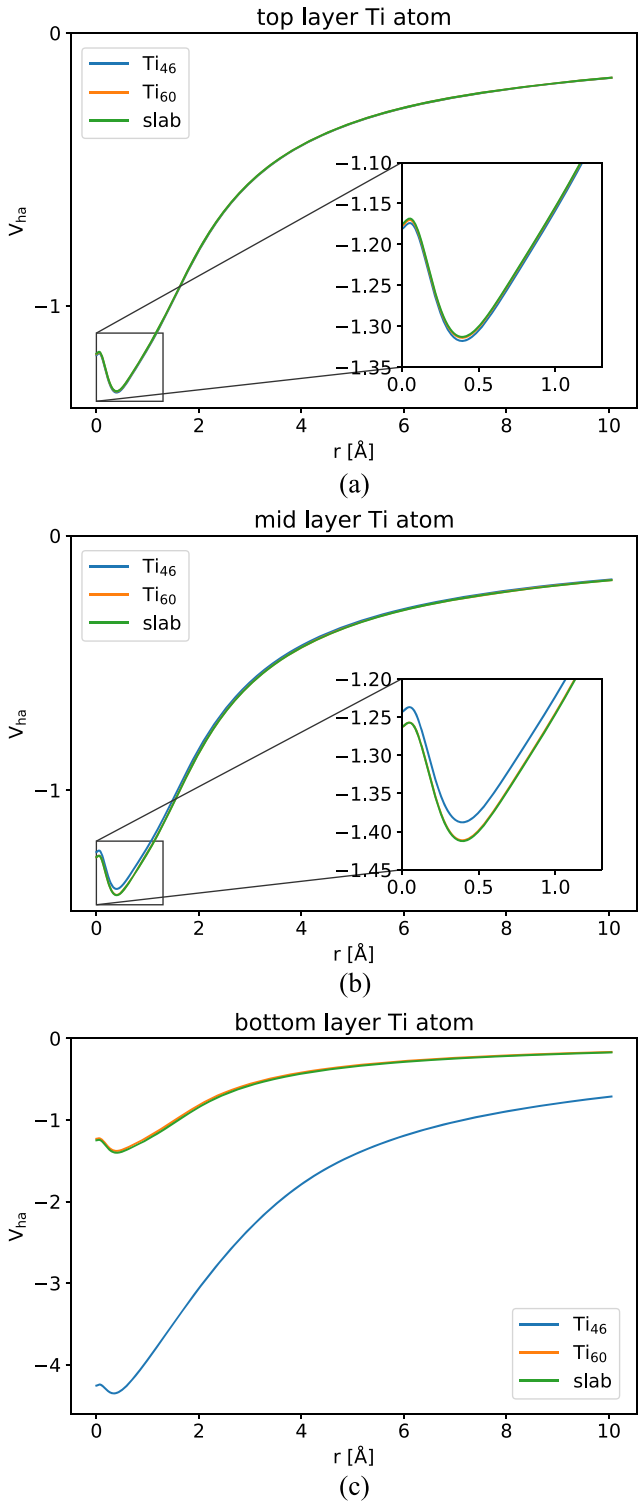

FIG. 12. The monopole (l = 0) component of the Hartree potential for the central row of Ti atoms of the polaron-optimized cluster models $Ti_{46}O_{92}$ and in model $Ti_{60}O_{120}$ compared to a PBC reference. Shown is a surface Ti atom (a), a mid layer Ti atom (b), and one bottom layer Ti atom (c).

Published under license by AIP Publishing

to spherical form of $Ti_{42}O_{92}$, which more naturally resembles the periodicity of the supercell approach.

c. Hartree potential. Finally, in order to investigate the unphysical charge accumulation at the boundaries of $Ti_{42}O_{92}$, we plot in Fig. 12 the monopole components of the Hartree potential for the central row of Ti atoms for each layer in a cluster and the PBC reference. For the first Ti atom, which is directly located under the bridging oxygen row in the center, all cluster models ($Ti_{46}O_{92}$ and $Ti_{60}O_{120}$) show excellent agreement with the periodic slab. For the Ti atom, in the second layer, the $Ti_{60}O_{120}$ model still shows perfect agreement with the slab calculation for $Ti_{46}O_{92}$; however, we observe slight deviations from the slab potential. This situation is greatly exacerbated on the third layer Ti atom. Here, the $Ti_{46}O_{92}$ model shows a huge error in the Hartree potential, whereas $Ti_{60}O_{120}$ is still in good agreement with the periodic reference. At this point, it should be highlighted that this huge error in the Hartree potential is not unique to this single atom but holds true for all atoms that are located directly at each cluster's boundary. From this perspective, it becomes clear that the inability of locating polarons in an S1-3/S1-11 configuration is a direct result of the erroneous description of the boundary atoms as the actual polaron state is also partly located at neighboring titanium and oxygen atoms.

C. Design criteria for embedded cluster models

Having understood the role of a cluster's shape and its local electrostatic potential in determining its suitability in an embedding setup allows us to now formulate more general criteria for the cluster design. The natural error estimate thereby is the maximum deviation of the Hartree potential $\Delta V_{Ha}(at)$—using again the monopole component—from its periodic counterpart at each atom (at) within the QM region. To be precise, we are calculating the maximum error according to

$$\Delta V_{Ha}(at) = \max\left\{\left|V_{Ha}^{PBC}(r;at) - V_{Ha}^{QM/MM}(r;at)\right|\right\}, \quad (4)$$

where $V_{Ha}^{PBC}(r)$ and $V_{Ha}^{QM/MM}(r)$ denote the Hartree potential for the periodic reference calculation and for the QM/MM approach, respectively. The corresponding results are depicted in Figs. 13 and 14 in the form of a histogram of the amount of atoms showing specific errors in their Hartree potentials. Owing to the especially fitted embedding environments, most atoms of each cluster thereby show only very minor to no deviations. Larger errors can be found on atoms close to or directly at the cluster's boundary. In general, as the cluster size increases, the surface to volume ratio decreases. This straightforwardly explains why larger clusters tend toward smaller errors in the potential and thus their electronic properties. A larger cluster can better compensate for errors in the embedding scheme. This view is further reinforced by the respective frontier orbital shapes plotted in Fig. 15, where again larger cluster models achieve better agreement with the periodic reference. However, as discussed before, by just considering the cluster size, one would expect the $Ti_{46}O_{96}$ cluster model to show equal or better performance than the $Ti_{44}O_{88}$ model. Regarding the DOS (see Fig. 8) and the shapes of the

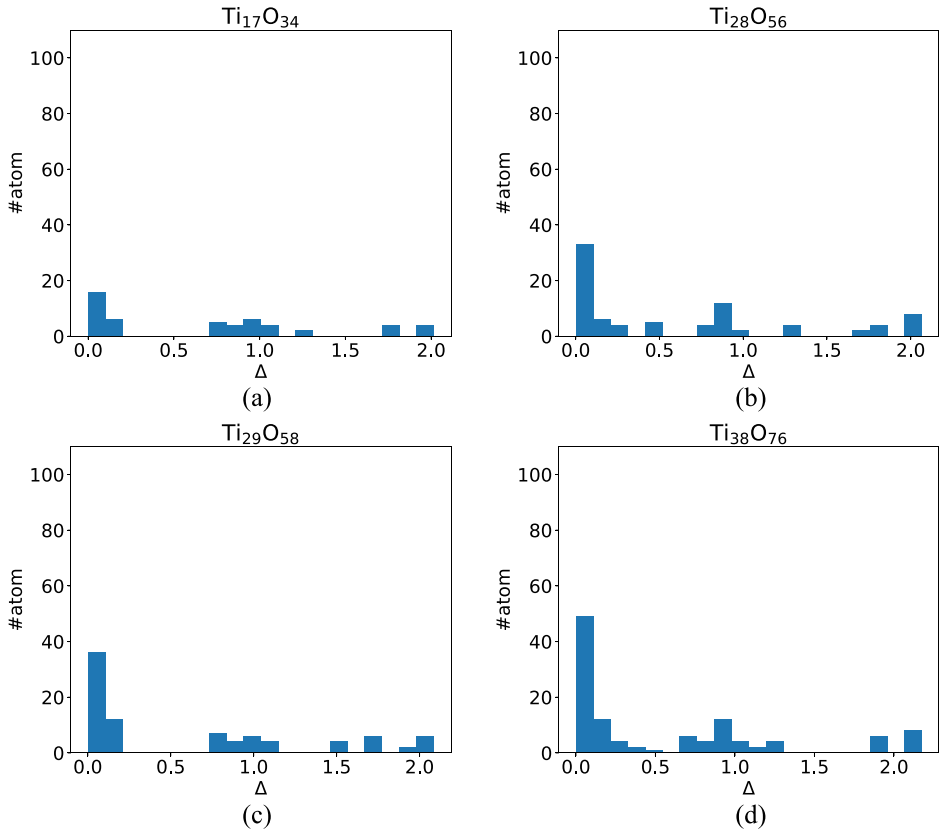

FIG. 13. Histogram of the number of atoms (at) showing given errors in their respective Hartree potentials $\Delta V_{ha}(at)$ ($l = 0$ component). Here, ΔV_{ha} is defined as the maximum deviation from a periodic reference calculation. Ordering is according to the size of the cluster starting with (a) $Ti_{17}O_{34}$, (b) $Ti_{28}O_{56}$, (c) $Ti_{29}O_{58}$, and (d) $Ti_{38}O_{76}$.

Published under license by AIP Publishing

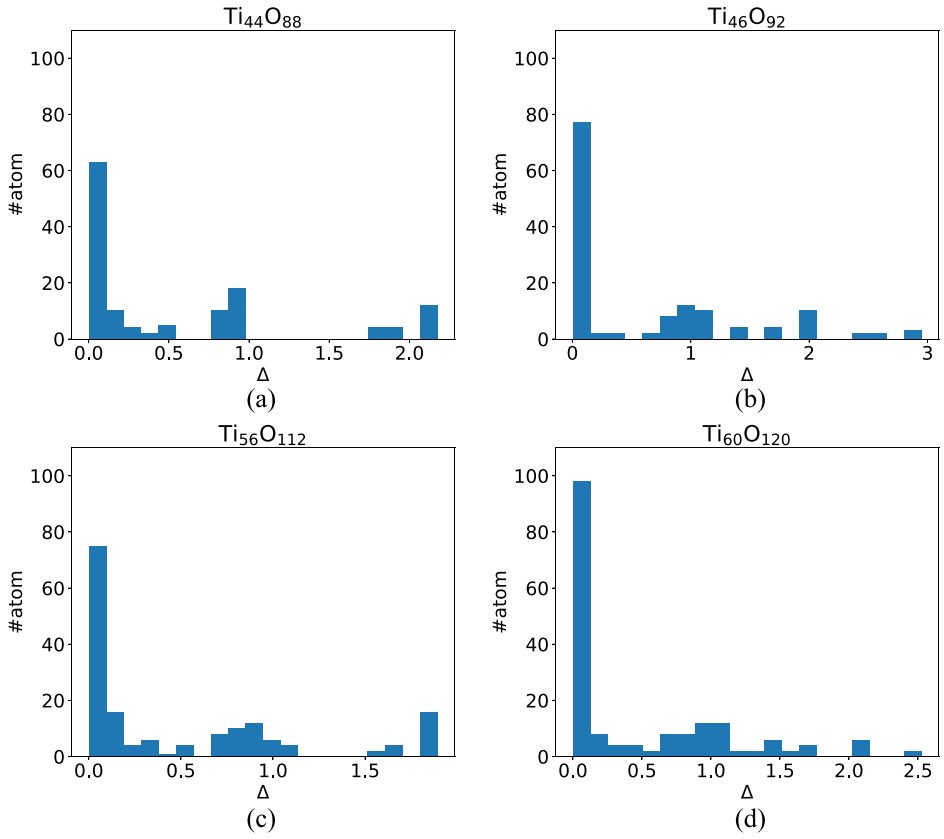

FIG. 14. Histogram of the number of atoms (at) showing given errors in their respective Hartree potentials ΔV_{ha}(at) (l = 0 component). Here, ΔV_{ha} is defined as the maximum deviation from a periodic reference calculation. Ordering is according to the size of the cluster starting with (a) $Ti_{44}O_{88}$, (b) $Ti_{46}O_{92}$, (c) $Ti_{56}O_{112}$, and (d) $Ti_{60}O_{120}$.

frontier orbitals (see Fig. 10), this is obviously not the case. Although for $Ti_{44}O_{88}$ there still is some accumulation of the LUMO at the bottom of the cluster, the overall orbital shapes resemble the periodic reference much better (see Fig. 15). The smaller cluster $Ti_{38}O_{76}$ even outperforms $Ti_{46}O_{96}$, both with regard to HOMO and LUMO shapes (see Fig. 15) as well as the DOS (Figs. 2 and 3). It is thus not necessarily the size of the cluster that governs its performance, but rather the number of atoms exposed to the cluster boundary, i.e., those with very erroneous local potentials. This clearly shows that by simply enlarging the cluster size, the results do not necessarily have to converge to those from a PBC approach, which one would otherwise intuitively assume. Notably, the number of atoms exposed to the cluster boundary seems to be the reason for the better performance of the $Ti_{38}O_{76}$ and $Ti_{44}O_{88}$ model compared to the $Ti_{46}O_{96}$ cluster. The more cubic shapes of $Ti_{38}O_{76}$ and $Ti_{44}O_{88}$ avoids very exposed rows of atoms like those on the bottom of $Ti_{46}O_{96}$, which suffer from huge deviations in the Hartree potential, thus giving rise to wrong frontier orbital shapes. It should be highlighted that these observed errors can not be fully explained by having a potentially erroneous embedding environment. If one compares $Ti_{28}O_{56}$ with $Ti_{29}O_{58}$—differing in size only by three atoms—one would expect an equally poor performance; however, $Ti_{28}O_{56}$ resembles the frontier orbitals shape much better than $Ti_{29}O_{58}$ [see parts (c)–(f) of Fig. 15]. This direct comparison between clusters of almost the same size again clearly indicates that the shape of the cluster plays an important role if all features of a PBC reference should be reproduced. Note, though, that this does not influence their performance in single-site adsorption studies, cf. Sec. III A, and thus cannot serve to derive a more detailed design criterion.

At that point, one could argue that a spherical shape would suit best as a design criterion as it shows the smallest surface to volume ratio. However, as demonstrated, a more cubic shape leads to a better description of frontier orbitals. Obviously, one has to find a trade-off between both the reduction in erroneous atoms and maintaining the overall periodic shape of the underlying material.

Furthermore, one "simple" solution to the problems of the cluster shape could arguably be to make the clusters larger and larger, approaching the limit of an infinitely extended, periodic crystal. As long as these large clusters do not suffer from any low order multipoles due to their shape,[16] the influence of erroneous atoms at the boundary should decrease compared to the large bulk of atoms at the interior of the cluster. Indeed, our results also point toward larger clusters generally yielding more accurate results. However, one of the main reasons for the use of solid state embedding models is the balance they strike between highly accurate electronic structure methods with the efficiency of having just a small number of atoms to treat. Our study thus represents a useful step toward the reliable design of solid state embedded models employing the smallest possible quantum region to still yield good agreement with periodic references.

Published under license by AIP Publishing

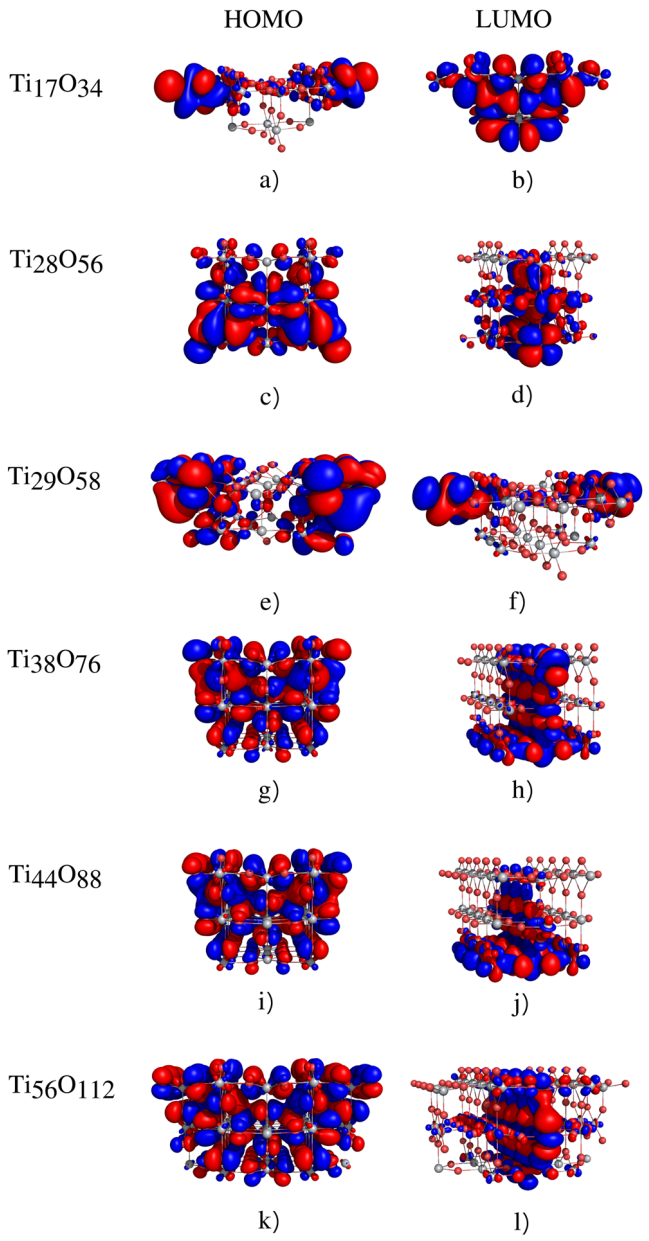

FIG. 15. Frontier orbitals of proposed cluster models for adsorption studies, $Ti_{17}O_{34}$ [(a) and (b)], $Ti_{28}O_{56}$ [(c) and (d)], $Ti_{29}O_{58}$ [(e) and (f)], $Ti_{38}O_{76}$ [(g) and (h)], $Ti_{44}O_{88}$ [(i) and (j)], and $Ti_{56}O_{112}$ [(k) and (l)]. HOMOs are given on the left column (a), (c), (e), (g), (i), and (k), while LUMOs are in the right column (b), (d), (f), (h), (j), and (l). As the cluster size decreases, errors due to imperfect embedding become more and more pronounced, making it harder for the cluster to correctly render the HOMO and LUMO shapes of a periodic reference calculation. Isosurface value 0.015 $eÅ^{-3}$.

Finally, although the above guidelines for the cluster design have only been directly tested on the rutile phase of TiO_2, they should be transferable to other phases of TiO_2 and even other materials. The—chemically highly important—frontier orbitals need to be well represented in the nonperiodic cluster model in order to accurately reflect the complex electronic states such as the formation of polarons in the material. In rutile TiO_2 (110), we have shown that this necessitates mostly square cluster shapes due to the periodicity of especially the lowest unoccupied frontier state. While other materials could show different geometries of the frontier states, a cluster shape that reflects these geometries is very likely always going to minimize embedding errors.

IV. SUMMARY AND CONCLUSION

In this work, we critically analyzed the performance of a common solid-state QM/MM embedding setup. Specifically, we focused on the influence of the size and shape of the cluster on the simulation results by studying the chemisorption of small molecules and formation of small polarons at the rutile TiO_2 (110) surface. Often in the literature,[3,9,16] the density of states or the adsorption energy of small molecules serves as a quality measurement of the employed computational approach. Yet, in light of our results, this should only be considered as one part of the puzzle. Especially if one deals with more complicated phenomena, the DOS or small molecular adsorption energies might prove to be too insensitive to give a full overview of a method's quality. In the case of dealing with ultrasensitive systems such as polaronic states, it turns out that it is crucial that all features of the periodic counter part reference, e.g., the shape of the frontier orbitals, are reproduced by the embedded cluster approach as well. We found that the observed robustness of adsorption energies vs cluster size or shape can be explained by the remarkable agreement of the Hartree potential at the central adsorption site with periodic references. In general, for adsorption energy studies where the adsorbate is located at a central cluster atom, very small cluster geometries already proved to be sufficient. However, as seen from our polaron localization results, one has to ensure that the observed physical phenomena are not affected by the erroneous description of cluster boundary atoms.

As a guideline for the cluster design, our analysis demonstrates that both the shape of the frontier orbitals and the density of states can give first hints of judging the quality of the used geometries. Moreover, the overall objective should be a reduction in the number of atoms with an erroneous Hartree potential. These two criteria seem to compete, to a certain degree, in that the former would call for a more rectangular cluster, mimicking a supercell in PBC, while the latter would favor (hemi-)spherical clusters in order to reduce the number of boundary atoms. Yet, we found that for realistically sized, i.e., not too large, clusters, the round shape often leads to highly exposed rows of atoms with Hartree potentials far from the periodic reference. Overall, we thus recommend the use of mostly rectangular cluster shapes for SSE models because these tend to render the electronic structure of the extended material most faithfully. The overall goal should be to mimic the electronic structure of the pristine periodic reference as accurate as possible, laying an accurate basis for further simulation of more complicated phenomena.

Finally, although the exact details of the ideal embedded cluster structure might vary between different embedding approaches, we fully expect our general conclusions to hold beyond our specific SSE approach and the here studied TiO_2 (110).

Published under license by AIP Publishing

SUPPLEMENTARY MATERIAL

In the supplementary material, we depict the adsorption geometries of OH, OOH, and H_2O used in this study. Furthermore, we provide structure files for the QM clusters used here.

ACKNOWLEDGMENTS

The authors would like to thank the German Research Foundation DFG (Grant No. OB425/4-1) and the Solar Technologies Go Hybrid Initiative of the State of Bavaria for support. This work was partially funded by the Deutsche Forschungsgemeinschaft (DFG, German Research Foundation) under Germany's Excellence Strategy – No. EXC 2089/1–390776260.

REFERENCES

[1] R. LeSar, *Introduction to Computational Materials Science: Fundamentals to Applications* (Cambridge University Press, 2013).
[2] N. Bernstein, J. R. Kermode, and G. Csányi, "Hybrid atomistic simulation methods for materials systems," Rep. Prog. Phys. **72**, 026501 (2009).
[3] C. S. Ammal and A. Heyden, "Modeling the noblemetal/TiO_2 (110) interface with hybrid DFT functionals: A periodic electrostatic embedded cluster model study," J. Chem. Phys. **133**, 164703 (2010).
[4] C. W. M. Castleton, A. Höglund, and S. Mirbt, "Density functional theory calculations of defect energies using supercells," Modell. Simul. Mater. Sci. Eng. **17**, 084003 (2009).
[5] S. Lany and A. Zunger, "Accurate prediction of defect properties in density functional supercell calculations," Modell. Simul. Mater. Sci. Eng. **17**, 084002 (2009).
[6] G. Makov and M. C. Payne, "Periodic boundary conditions in *ab initio* calculations," Phys. Rev. B **51**, 4014–4022 (1995).
[7] H. Oberhofer, "Electrocatalysis beyond the computational hydrogen electrode," in *Handbook of Materials Modeling: Applications: Current and Emerging Materials* (Springer, Netherlands, 2018), pp. 1–33.
[8] S. Grimme and M. Steinmetz, "A computationally efficient double hybrid density functional based on the random phase approximation," Phys. Chem. Chem. Phys. **18**, 20926–20937 (2016).
[9] D. Berger, H. Oberhofer, and K. Reuter, "First-principles embedded-cluster calculations of the neutral and charged oxygen vacancy at the rutile TiO_2(110) surface," Phys. Rev. B **92**, 075308 (2015).
[10] W. Chibani, X. Ren, M. Scheffler, and P. Rinke, "Self-consistent green's function embedding for advanced electronic structure methods based on a dynamical mean-field concept," Phys. Rev. B **93**, 165106 (2016).
[11] F. R. Manby, M. Stella, J. D. Goodpaster, and T. F. Miller III, "A simple, exact density-functional-theory embedding scheme," J. Chem. Theory Comput. **8**, 2564–2568 (2012).
[12] A. Kubas, D. Berger, H. Oberhofer, D. Maganas, K. Reuter, and F. Neese, "Surface adsorption energetics studied with "gold standard" wave-function-based *ab initio* methods: Small-molecule binding to TiO_2(110)," J. Phys. Chem. Lett. **7**, 4207–4212 (2016).
[13] V. A. Nasluzov, V. V. Rivanenkov, A. B. Gordienko, K. M. Neyman, U. Birkenheuer, and N. Rösch, "Cluster embedding in an elastic polarizable environment: Density functional study of Pd atoms adsorbed at oxygen vacancies of MgO (001)," J. Chem. Phys. **115**, 8157–8171 (2001).
[14] H. Lin and D. G. Truhlar, "QM/MM: What have we learned, where are we, and where do we go from here?," Theor. Chem. Acc. **117**, 185 (2007).
[15] T. W. Keal, P. Sherwood, G. Dutta, A. A. Sokol, and C. R. A. Catlow, "Characterization of hydrogen dissociation over aluminium-doped zinc oxide using an efficient massively parallel framework for QM/MM calculations," Proc. R. Soc. A **467**, 1900–1924 (2011).
[16] D. Berger, A. J. Logsdail, H. Oberhofer, M. R. Farrow, C. R. A. Catlow, P. Sherwood, A. A. Sokol, V. Blum, and K. Reuter, "Embedded-cluster calculations in a numeric atomic orbital density-functional theory framework," J. Chem. Phys. **141**, 024105 (2014).
[17] S. Bhattacharya, D. Berger, K. Reuter, L. M. Ghiringhelli, and S. V. Levchenko, "Theoretical evidence for unexpected O-rich phases at corners of MgO surfaces," Phys. Rev. Mater. **1**, 071601 (2017).
[18] L. E. Ratcliff, S. Mohr, G. Huhs, T. Deutsch, M. Masella, and L. Genovese, "Challenges in large scale quantum mechanical calculations," Wiley Interdiscip. Rev.: Comput. Mol. Sci. **7**, e1290 (2017).
[19] A. J. Logsdail, C. A. Downing, T. W. Keal, P. Sherwood, A. A. Sokol, and C. R. A. Catlow, "Hybrid—DFT modeling of lattice and surface vacancies in MnO," J. Phys. Chem. C **123**, 8133–8144 (2019).
[20] M. Alessio, F. A. Bischoff, and J. Sauer, "Chemically accurate adsorption energies for methane and ethane monolayers on the MgO(001) surface," Phys. Chem. Chem. Phys. **20**, 9760–9769 (2018).
[21] G. Piccini, M. Alessio, and J. Sauer, "*Ab initio* study of methanol and ethanol adsorption on Brønsted sites in zeolite H-MFI," Phys. Chem. Chem. Phys. **20**, 19964–19970 (2018).
[22] P. Sherwood, A. H. de Vries, M. F. Guest, G. Schreckenbach, C. R. A. Catlow, S. A. French, A. A. Sokol, S. T. Bromley, W. Thiel, A. J. Turner, S. Billeter, F. Terstegen, S. Thiel, J. Kendrick, S. C. Rogers, J. Casci, M. Watson, F. King, E. Karlsen, M. Sjøvoll, A. Fahmi, A. Schäfer, and C. Lennartz, "QUASI: A general purpose implementation of the QM/MM approach and its application to problems in catalysis," J. Mol. Struct.: THEOCHEM **632**, 1–28 (2003).
[23] S. Metz, J. Kästner, A. A. Sokol, T. W. Keal, and P. Sherwood, "ChemShell—A modular software package for QM/MM simulations," Wiley Interdiscip. Rev.: Comput. Mol. Sci. **4**, 101–110 (2014).
[24] M. Matsui and S. Sakaki, "Embedded cluster model for Al_2O_3 and $AlPO_4$ surfaces using point charges and periodic electrostatic potential," J. Phys. Chem. C **121**, 20242–20253 (2017).
[25] N. A. Deskins, R. Rousseau, and M. Dupuis, "Distribution of Ti^{3+} surface sites in reduced TiO_2," J. Phys. Chem. C **115**, 7562–7572 (2011).
[26] M. Setvin, C. Franchini, X. Hao, M. Schmid, A. Janotti, M. Kaltak, C. G. Van de Walle, G. Kresse, and U. Diebold, "Direct view at excess electrons in TiO_2 rutile and anatase," Phys. Rev. Lett. **113**, 086402 (2014).
[27] E. Finazzi, C. Di Valentin, G. Pacchioni, and A. Selloni, "Excess electron states in reduced bulk anatase TiO_2: Comparison of standard GGA, GGA+U, and hybrid DFT calculations," J. Chem. Phys. **129**, 154113 (2008).
[28] A. Valdés, Z.-W. Qu, G.-J. Kroes, J. Rossmeisl, and J. K. Nørskov, "Oxidation and photo-oxidation of water on TiO_2 surface," J. Phys. Chem. C **112**, 9872–9879 (2008).
[29] P. J. D. Lindan and C. Zhang, "Exothermic water dissociation on the rutile TiO_2(110) surface," Phys. Rev. B **72**, 075439 (2005).
[30] K. Reuter, C. P. Plaisance, H. Oberhofer, and M. Andersen, "Perspective: On the active site model in computational catalyst screening," J. Chem. Phys. **146**, 040901 (2017).
[31] C. Di Valentin, G. Pacchioni, and A. Selloni, "Electronic structure of defect states in hydroxylated and reduced rutile TiO_2(110) surfaces," Phys. Rev. Lett. **97**, 166803 (2006).
[32] S. Schnur and A. Groß, "Properties of metal–water interfaces studied from first principles," New J. Phys. **11**, 125003 (2009).
[33] D. O. Scanlon, C. W. Dunnill, J. Buckeridge, S. A. Shevlin, A. J. Logsdail, S. M. Woodley, C. R. A. Catlow, M. J. Powell, R. G. Palgrave, I. P. Parkin, G. W. Watson, T. W. Keal, P. Sherwood, A. Walsh, and A. A. Sokol, "Band alignment of rutile and anatase TiO_2," Nat. Mater. **12**, 798 (2013).
[34] M. Kick, K. Reuter, and H. Oberhofer, "Intricacies of DFT+U, not only in a numeric atom centered orbital framework," J. Chem. Theory Comput. **15**, 1705–1718 (2019).
[35] B. G. Dick and A. W. Overhauser, "Theory of the dielectric constants of alkali halide crystals," Phys. Rev. **112**, 90–103 (1958).
[36] V. Blum, R. Gehrke, F. Hanke, P. Havu, V. Havu, X. Ren, K. Reuter, and M. Scheffler, "*Ab initio* molecular simulations with numeric atom-centered orbitals," Comput. Phys. Commun. **180**, 2175–2196 (2009).
[37] O. Lamiel-Garcia, K. C. Ko, J. Y. Lee, S. T. Bromley, and F. Illas, "When anatase nanoparticles become bulklike: Properties of realistic TiO_2 nanoparticles in the

Published under license by AIP Publishing

1–6 nm size range from all electron relativistic density functional theory based calculations," J. Chem. Theory Comput. **13**, 1785–1793 (2017).
[38]H. J. Monkhorst and J. D. Pack, "Special points for Brillouin-zone integrations," Phys. Rev. B **13**, 5188–5192 (1976).
[39]V. Anisimov, J. Zaanen, and O. K. Andersen, "Band theory and Mott insulators: Hubbard *U* instead of Stoner *I*," Phys. Rev. B **44**, 943–954 (1991).
[40]S. L. Dudarev, G. A. Botton, S. Y. Savrasov, C. J. Humphreys, and A. P. Sutton, "Electron-energy-loss spectra and the structural stability of nickel oxide: An LSDA+U study," Phys. Rev. B **57**, 1505–1509 (1998).
[41]T. Shibuya, K. Yasuoka, S. Mirbt, and B. Sanyal, "A systematic study of polarons due to oxygen vacancy formation at the rutile TiO_2 (110) surface by GGA+U and HSE06 methods," J. Phys.: Condens. Matter **24**, 435504 (2012).
[42]P. M. Kowalski, M. F. Camellone, N. N. Nair, B. Meyer, and D. Marx, "Charge localization dynamics induced by oxygen vacancies on the TiO_2(110) surface," Phys. Rev. Lett. **105**, 146405 (2010).
[43]M. E. Arroyo-de Dompablo, A. Morales-García, and M. Taravillo, "DFT+U calculations of crystal lattice, electronic structure, and phase stability under pressure of TiO_2 polymorphs," J. Chem. Phys. **135**, 054503 (2011).
[44]B. Himmetoglu, A. Floris, S. de Gironcoli, and M. Cococcioni, "Hubbard-corrected DFT energy functionals: The LDA+U description of correlated systems," Int. J. Quantum Chem. **114**, 14–49 (2014).
[45]H. Eschrig, K. Koepernik, and I. Chaplygin, "Density functional application to strongly correlated electron systems," J. Solid State Chem. **176**, 482–495 (2003).
[46]C. M. Yim, C. L. Pang, and G. Thornton, "Oxygen vacancy origin of the surface band-gap state of TiO_2(110)," Phys. Rev. Lett. **104**, 036806 (2010).
[47]B. Hammer, L. B. Hansen, and J. K. Norskov, "Improved adsorption energetics within density-functional theory using revised Perdew-Burke-Ernzerhof functionals," Phys. Rev. B **59**, 7413–7421 (1999).
[48]R. A. Buckingham and J. E. Lennard-Jones, "The classical equation of state of gaseous helium, neon and argon," Proc. R. Soc. A **168**, 264–283 (1938).
[49]H. Sato, K. Ono, T. Sasaki, and A. Yamagishi, "First-principles study of two-dimensional titanium dioxides," J. Phys. Chem. B **107**, 9824–9828 (2003).
[50]H. Oberhofer and K. Reuter, "First-principles thermodynamic screening approach to photo-catalytic water splitting with co-catalysts," J. Chem. Phys. **139**, 044710 (2013).
[51]T. Stecher, K. Reuter, and H. Oberhofer, "First-principles free-energy barriers for photoelectrochemical surface reactions: Proton abstraction at TiO_2 (110)," Phys. Rev. Lett. **117**, 276001 (2016).
[52]J. P. Prates Ramalho, F. Illas, and J. R. B. Gomes, "Adsorption of CO on the rutile TiO_2(110) surface: A dispersion-corrected density functional theory study," Phys. Chem. Chem. Phys. **19**, 2487–2494 (2017).
[53]Y.-C. Wang, Z.-H. Chen, and H. Jiang, "The local projection in the density functional theory plus U approach: A critical assessment," J. Chem. Phys. **144**, 144106 (2016).
[54]Y.-C. Wang and H. Jiang, "Local screened Coulomb correction approach to strongly correlated d-electron systems," J. Chem. Phys. **150**, 154116 (2019).
[55]B. Dorado, B. Amadon, M. Freyss, and M. Bertolus, "DFT+U calculations of the ground state and metastable states of uranium dioxide," Phys. Rev. B **79**, 235125 (2009).
[56]J. P. Allen and G. W. Watson, "Occupation matrix control of d- and f-electron localisations using DFT+U," Phys. Chem. Chem. Phys. **16**, 21016–21031 (2014).
[57]H. Oberhofer and J. Blumberger, "Charge constrained density functional molecular dynamics for simulation of condensed phase electron transfer reactions," J. Chem. Phys. **131**, 064101 (2009).
[58]Q. Wu and T. Van Voorhis, "Direct optimization method to study constrained systems within density-functional theory," Phys. Rev. A **72**, 024502 (2005).
[59]Z. Wang, C. Brock, A. Matt, and K. H. Bevan, "Implications of the DFT+U method on polaron properties in energy materials," Phys. Rev. B **96**, 125150 (2017).

Published under license by AIP Publishing

C Paper # 3

Mobile Small Polarons Explain Conductivity in Lithium Titanium Oxide Battery Electrodes

Matthias Kick, Cristina Grosu, Markus Schuderer, Christoph Scheurer and Harald Oberhofer
Published on arXiv.org (2020).
arXiv:2001.00263

Reprinted under the terms of Creative Commons Attribution 4.0 International License.

Mobile Small Polarons Explain Conductivity in Lithium Titanium Oxide Battery Electrodes

Matthias Kick,[†] Cristina Grosu,[†,‡] Markus Schuderer,[†] Christoph Scheurer,[†] and Harald Oberhofer[*,†]

†*Chair for Theoretical Chemistry and Catalysis Research Center, Technical University of Munich, Lichtenbergstr. 4, 85747 Garching, Germany*

‡*Institute of Energy an Climate Research (IEK-9), Forschungszentrum Jülich, 52425 Jülich, Germany*

E-mail: harald.oberhofer@tum.de

Abstract

Lithium titanium oxide $Li_4Ti_5O_{12}$ (LTO) is an intriguing anode material promising particularly long lived batteries, due to its remarkable phase stability during (dis)charging of the cell. However, its usage is limited by its low intrinsic electronic conductivity. Introducing oxygen vacancies can be one method to overcome this drawback, possibly by altering the charge carrier transport mechanism. We use Hubbard corrected density-functional theory (DFT+U) to show that polaronic states in combination with a possible hopping mechanism can play a crucial role in the experimentally observed increase of electronic conductivity. To gauge polaronic charge mobility, we compute relative stabilities of different localization patterns and estimate polaron hopping barrier heights. With this we finally show how defect engineering can indeed raise the electronic conductivity of LTO up to the level of its ionic conductivity, thereby explaining first experimental results for reduced LTO.

Introduction

Energy storage solutions such as Li-ion batteries (LIB) are a key technology in the transition from a fossil fuel based economy to a society based on sustainable resource management.[1,2] Despite the tremendous advancements in battery research over the last few years,[3] durability and especially storage capacity still need significant improvements for batteries to represent a viable alternative e.g. in the transport and mobility sectors.[2,4] One promising material envisioned as a potential remedy for these problems in conventional as well as all-solid state batteries (ASSB) is lithium titanium oxide (LTO).[2] Zero strain insertion, high cycling stability and a stable charge/discharge plateau render LTO an excellent anode material for long living batteries.[2,4–6] Its general use, however, is still limited by the fact that LTO suffers from a very low intrinsic electronic conductivity.[7,8] One way to overcome this drawback is to expose LTO to a reductive hydrogen atmosphere at elevated temperatures, leading to the formation of oxygen vacancies. As experimental data shows,[9] this not only causes a color change from white to blue but also lowers electronic resistance and impedance. Moreover, this blue LTO also shows improved Li-ion mobility compared to pristine white LTO.[9]

Unfortunately, neither of these improvements in carrier mobility are currently fully understood from a mechanistic viewpoint. Yet, first hints at the nature of the improved electronic conductivity in LTO emerged recently with the experimental discovery of paramagnetic Ti^{3+} centers.[8–11] The significance of these becomes apparent considering an analogous case in TiO_2, where oxygen vacancies are known to lead to the formation of small polarons mainly localized on Ti sites.[12–14] While these polarons are somewhat attracted to the vacancy itself,[15,16] they were also shown to be very mobile, with kinetic barriers that can easily be overcome at room temperature.[17] In this context we studied the formation and stability of polarons in bulk LTO, as well as the kinetic barriers separating them. Especially the latter strongly hints at a polaron hopping mechanism as the source of the observed improvement of electronic conductivity in blue LTO.

Results

For our analysis we considered a $2 \times 2 \times 1$ supercell of $Li_4Ti_5O_{12}$ (LTO) in its most stable[6] spinel configuration,[18] and created an oxygen vacancy at the energetically most favorable of the symmetry inequivalent sites (cf. supplementary material). This realization of the structural Li/Ti disorder is known to exhibit a Ti-deficient zone separating titanium layers as illustrated in Figure 1. It therefore lets us examine the interplay between structure, in the form of Li-rich and Li-poor regions, and function of the material. Removing a neutral oxygen atom from the simulation cell gives rise to two excess electrons, which can form two polaronic Ti^{3+} centers. In standard semi-local LDA[19] or GGA[20] based DFT these can generally not be described at all due to the functionals' well known charge and spin delocalization errors.[21] As a cost-efficient remedy, we here make use of the popular Hubbard corrected[22–24] variant of the PBE[20] functional (PBE+U) in combination with the matrix control approach.[25,26] This combination has not only been shown to yield easy access to all manners of polaron configurations but also to yield excellent results compared to the computationally much more expensive hybrid DFT functionals.[15] Given the great structural complexity of defect-rich LTO, there is a large number—$\binom{40}{2} = 780$—of unique polaron localization patterns even in our relatively small simulation box. To distinguish them we calculated their relative stability according to $E_{\mathrm{rel}} = E_{\mathrm{tot,i}} - E_{\mathrm{tot,\,min}}$, where $E_{\mathrm{tot,i}}$ denotes the total energy of a given simulation box calculated with DFT and $E_{\mathrm{tot,\,min}}$ denotes the total energy of the most stable structure found so far. Hence, following standard procedures,[12] the most stable configuration serves as zero point of our energy scale, with all other configurations possessing positive relative energy.

An exhaustive computational sampling is complicated further by the fact that the electrons can localize both in a triplet or an open-shell singlet configuration.[12,13] On the other hand, many of these patterns are, if not fully degenerate, at least very close in energy. For a first demonstration of the existence and mobility of polarons in LTO and their influence on the electronic conductivity a complete sampling of all configurations is therefore not nec-

essary. Instead, we focus on triplet configurations and localization patterns representative for the system as a whole. In detail, we considered 13 patterns with different distances to the defect site, localized within different Ti layers in the bulk unit cell. To distinguish them, we adapt a naming convention used in our earlier work[15] to the case of LTO, cf. Figure 1. We found the most stable defect position to be located in the center of the Ti-rich region of our layered LTO model (black circle in Figure 1, cf. also supplementary material). This localization is not at all surprising, as it allows the O-vacancy to be as far as possible from the Li-rich zone of our simulation cell and the structural distortions caused by it. Using this defect position throughout, Table 1 lists our obtained results regarding the relative stability of different polaron localization patterns. We found that the most stable

Table 1: Relative stabilities of the most representative polaronic configurations. The systems are ordered by their relative stabilities. A complete list of calculated systems can be found in the supplementary information. Also shown is the shortest periodic distance between the two Ti^{3+} centers ($d_{Ti^{3+}-Ti^{3+}}$).

For vertical layer–layer distances see Fig. 1.

system	E_{rel} [eV]	$d_{Ti^{3+}-Ti^{3+}}$[Å]	system	E_{rel} [eV]	$d_{Ti^{3+}-Ti^{3+}}$[Å]
L3-7/L2-9	0.00	6.6	L5-1/L3-12	0.45	7.9
L3-8/L3-4	0.12	6.0	L4-2/L4-4	0.75	5.9
L3-7/L3-12	0.13	7.9	L1-1/L1-4	0.77	10.0
L2-7/L2-8	0.14	5.9	L5-5/L4-2	0.82	7.9
L3-9/L3-12	0.23	3.0	L4-3/L4-4	1.00	6.0
L2-9/L2-12	0.26	2.9	L5-1/L5-5	2.59	6.0

configurations are those where one polaron is located in L2 and the other is located in L3 (cf. Figure 2a), followed by configurations where both polarons are either located in L2 or L3. The main difference is that "same-plane" polarons approach each other more closely and hence Coulomb repulsion is more pronounced compared to the most stable L3-X/L2-Y configurations. Furthermore, our analysis shows that there is also a tendency for polarons to be less stable the closer they are located to the defect site. This is clearly indicated by the configurations where both excess electrons are localized on Ti atoms belonging to layers L4 or L5 (see supplementary information for detailed distances to the defect site). Both of

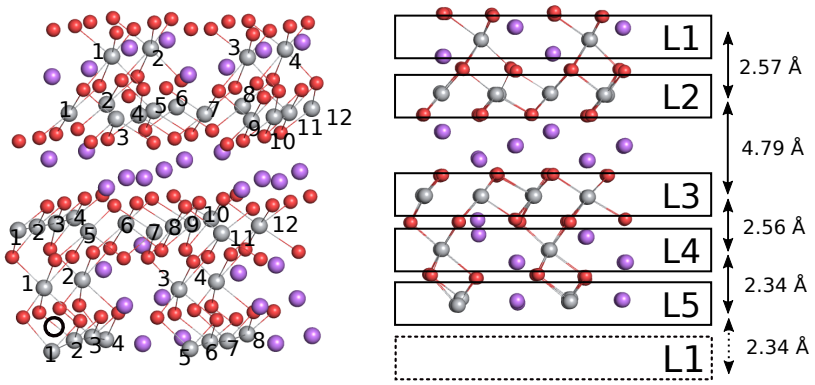

Figure 1: Sketch of the site naming convention of the different localization patterns. Lx-m/Ly-n specifies the localization of one electron within layer Lx on atom m with the second electron localized in layer Ly on atom n. Additionally, the position of the oxygen vacancies is marked with a black circle. Titanium atoms are depicted as grey spheres, oxygen atoms are shown as red spheres. On the right, arrows and numbers indicate the average inter layer titanium distance within the given unit cell.

these effects compete with each other, such that polarons try to adopt configurations with maximal distances to the defect and between each other. This situation seems similar to TiO_2 where the oxygen defect is acting as a charge trapping center.[27,28] However, in LTO one can not directly extract a clear stability trend with the distance to the defect, as positively charged Li-ions also show some influence on the overall stabilities of the polarons.[29] Indeed, our choice of LTO cell allows us to quantify their influence, considering the fact that all our most stable defect configurations are located next to the Li-rich zone situated between L2 and L3.

Finally, in order to gauge the polaron mobility we calculate hopping barriers between our most stable configuration and adjacent Ti atoms. To this end, we again make use of the matrix control approach,[25,26] but with a modified occupation matrix scheme outlined in the supplementary material. This approach allows us to restrain the electronic configuration of the system along a pre-selected reaction coordinate x, which linearly interpolates between two stable polaronic states, localized at neighboring atoms. Representatively for all hopping processes in the system we compute the "in-plane" transition of L3-7/L2-10 (x = 0.0) to L3-7/L2-9 (x = 1.0) and the "out-of-plane" transition of L3-7/L1-3 (x = 0.0) to L3-7/L2-9

(x = 1.0).

We illustrate this pathway in Figure 2, which in a) shows the spin density of the final state L3-7/L2-9 and in b) depicts we the relaxation of atoms from their respective sites in the pristine crystal for the transition from L3-7/L2-10 to L3-7/L2-9 via a transition state. We thereby only depict O atoms nearest to the involved Ti sites as only these show any significant distortion during a full geometry optimization. Figure 2b clearly shows relaxation of the O-atoms towards the respective Ti^{3+} sites in the initial (L2-10, blue) and final (L2-9, red) states, indicating a small polaron hopping mechanism. A similar picture arises for the transition from L3-7/L1-3 to L3-7/L2-9 (not pictured).

The energy profiles of these two transitions are depicted in Figure 3. As highlighted by the dashed black lines, the hopping barriers for transition L3-7/L2-10 to L3-7/L2-9 and for transition L3-7/L1-3 to L3-7/L2-9 are 186 meV and 583 meV respectively, with the later being much larger due to the already significant energy difference of 485 meV between the two stable states. With these barrier heights we can roughly estimate the in- and out-of-plane conductivity based on a simple hopping model (cf. supplementary material) and using an experimentally measured density of Ti^{3+} centers of 13.1 at%[30] as a measure for the charge carrier density. For the in-plane conductivity we thus find a value of 95.3 mS/cm, while the significantly higher out-of-plane hopping barrier results in a much smaller conductivity of 17×10^{-6} mS/cm. To put these results into context, even our lower bound for the conductivity of reduced LTO is already five orders of magnitude higher than the pristine material,[30] while our ideal upper bound is of the order of the ion conductivities in currently employed electrolytes.[31] Note that the estimate for the ideal conductivity rests on the assumption that there are no other, significantly higher barriers along the whole pathway of charge percolation through the crystal. This implies a distribution of defects aligned along the [100] axis of the crystal. Considering the fairly high density of oxygen defects present in blue LTO, such a case is certainly achievable.

Discussion

To conclude, our stability analysis clearly indicates that the experimentally observed Ti^{3+} centers in reduced LTO can in fact be the result of small polaron formation. Moreover, comparatively small barrier heights indicate that charge hopping dynamics can already occur at room temperature. This renders a polaron hopping mechanism to be the most likely origin of the increased electronic conductivity observed in blue LTO. Indeed a simple conductivity model puts even the worst estimate of 17×10^{-6} mS/cm five orders of magnitude above pristine LTO. On the other hand, the ideal predicted case based on an in-plane hopping mechanism would lead to a conductivity of 100 mS/cm, which, though significantly lower than that of other anode materials,[31–33] is nevertheless comparable to the ion conductivities of the pristine material and super–ionic conductors.[2,10,34] Moreover, the existence of polarons also hints at a mechanism for the improved ion diffusivity in blue LTO, which is about twice that of pristine LTO.[30] The presence of polarons, which we have shown to localize near Li-rich regions, could serve to "soften" the environment for Li-diffusion by screening the positive charge carriers. Thus, both, the ideal polaron conductivity of blue LTO, and its improved Li diffusivity, would make it a suitable option for an anode material for use in tomorrow's batteries. Note that our results show a very wide range of potential conductivity values, depending on defect patterning, local crystal structure and crystal orientation. Our study thus highlights the potential and also pitfalls of defect engineering as a means for the generation of mobile charge carriers in otherwise insulating materials.

Methods

All necessary calculations have been carried out using the FHI-aims[35] code. To account for adequate electron localization we used the DFT+U[23] variant of the PBE[20] exchange correlation functional. The Ti $3d$ atomic like basis functions served as Hubbard projectors and a U value of 2.65 eV has been applied. In detail we used the rotationally invariant

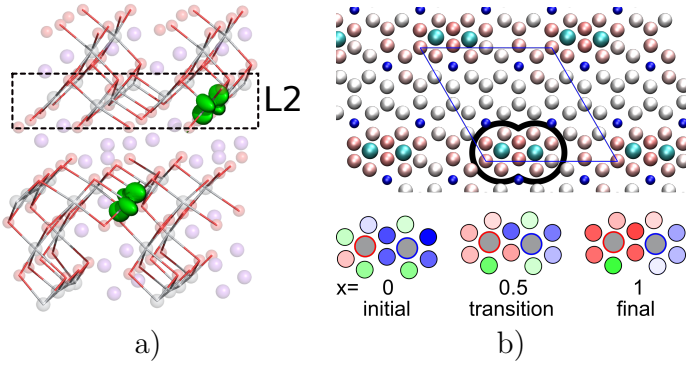

Figure 2: a) Spin density of the most stable configuration L3-7/L2-9 of our simulation. Isosurface level 0.015 eÅ^{-3}. b) Top: cut through the simulation cell showing the L2-layer, showing the distortion of the lattice at the transition state. Atoms in cyan indicating the L2-9 and L2-10 positions respectively. Darker red colors indicate a stronger movement during the transition from L3-7/L2-10 to L3-7/L2-9. Note that only nearest neighbor oxygen atoms show significant movement, indicating indeed the hopping of a small polaron. Bottom: schematic of the movement of oxygen atoms from their undistorted sites for the transition from L3-7/L2-10 (left) to L3-7/L2-9 (right) via a transition state (center). Circles filled in red hues indicate a predominant movement of the respective O atom towards the Ti atom at L2-9 (red circle filled with grey), while blue hues depict a movement towards L2-10 (blue circle filled with grey). Circles filled in green hues show movement not clearly aimed at either Ti atoms. In all cases darker colors indicate stronger movement.

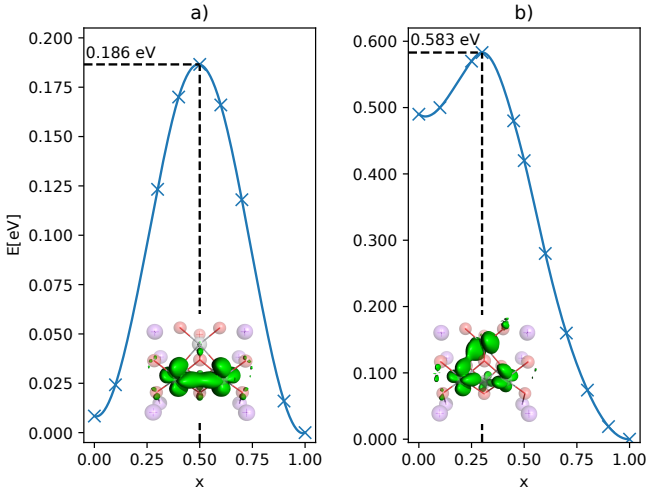

Figure 3: Calculated barrier profiles for the transition L3-7/L2-10 to L3-7/L2-9 (a) and L3-7/L1-3 to L3-7/L2-9 (b). In both plots x = 1.0 is equal to configuration L3-7/L2-9. The lowest lying configuration in energy serves as zero point for the energy scale. Also shown is the spin density of the corresponding transition state. Isosurface level 0.015 eÅ^{-3}.

+U form[24] with the double-counting correction in the fully localized limit[36]. Numerical convergence has been reached using a *tight tier1* basis employing a $2 \times 2 \times 1$ k-point grid. Geometries have been relaxed until residual force fell below 10^{-2} eV/Å. For more detailed information the reader is referred to our supporting information.

Acknowledgements

The authors would like to thank the German Research Foundation DFG (Grant OB425/4-1) and the Solar Technologies Go Hybrid Initiative of the State of Bavaria for support. Partially funded by the Deutsche Forschungsgemeinschaft (DFG, German Research Foundation) under Germany's Excellence Strategy EXC 2089/1 390776260.

References

(1) Islam, M. S.; Fisher, C. A. J. Lithium and sodium battery cathode materials: computational insights into voltage, diffusion and nanostructural properties. *Chem. Soc. Rev.* **2014**, *43*, 185–204.

(2) Zhao, B.; Ran, R.; Liu, M.; Shao, Z. A comprehensive review of $Li_4Ti_5O_{12}$-based electrodes for lithium-ion batteries: The latest advancements and future perspectives. *Mater. Sci. Eng. R Rep* **2015**, *98*, 1 – 71.

(3) Chu, S.; Majumdar, A. Opportunities and challenges for a sustainable energy future. *Nature* **2012**, *488*, 294 EP –.

(4) Armand, M.; Tarascon, J.-M. Building better batteries. *Nature* **2008**, *451*, 652 EP –.

(5) Aricò, A. S.; Bruce, P.; Scrosati, B.; Tarascon, J.-M.; van Schalkwijk, W. Nanostructured materials for advanced energy conversion and storage devices. *Nat. Mater.* **2005**, *4*, 366–377.

(6) Heenen, H. H.; Scheurer, C.; Reuter, K. Implications of occupational Disorder on ion mobility in $Li_4Ti_5O_{12}$ battery materials. *Nano Lett.* **2017**, *17*, 3884–3888.

(7) Yuan, T.; Yu, X.; Cai, R.; Zhou, Y.; Shao, Z. Synthesis of pristine and carbon-coated $Li_4Ti_5O_{12}$ and their low-temperature electrochemical performance. *J. Power Sources* **2010**, *195*, 4997 – 5004.

(8) Yan, B.; Li, M.; Li, X.; Bai, Z.; Yang, J.; Xiong, D.; Li, D. Novel understanding of carbothermal reduction enhancing electronic and ionic conductivity of $Li_4Ti_5O_{12}$ anode. *J. Mater. Chem. A* **2015**, *3*, 11773–11781.

(9) Qiu, J.; Lai, C.; Gray, E.; Li, S.; Qiu, S.; Strounina, E.; Sun, C.; Zhao, H.; Zhang, S. Blue hydrogenated lithium titanate as a high-rate anode material for lithium-ion batteries. *J. Mater. Chem. A* **2014**, *2*, 6353–6358.

(10) Kaftelen, H.; Tuncer, M.; Tu, S.; Repp, S.; Gmez, H.; Thomann, R.; Weber, S.; Erdem, E. Mn-substituted spinel $Li_4Ti_5O_{12}$ materials studied by multifrequency EPR spectroscopy. *J. Mater. Chem. A* **2013**, *1*, 9973–9982.

(11) Jakes, P.; Granwehr, J.; Kungl, H.; Rüdiger-A, E. Mixed ionic-electronic conducting $Li_4Ti_5O_{12}$ as anode material for lithium ion batteries with enhanced rate capability - impact of oxygen non-stoichiometry and aliovalent Mg^{2+}-doping studied by electron paramagnetic resonance. *Z. Phys. Chem.* **2015**, *229*, 1439–1450.

(12) Deskins, N. A.; Rousseau, R.; Dupuis, M. Distribution of Ti^{3+} surface sites in reduced TiO_2. *J. Phys. Chem. C* **2011**, *115*, 7562–7572.

(13) Shibuya, T.; Yasuoka, K.; Mirbt, S.; Sanyal, B. A systematic study of polarons due to oxygen vacancy formation at the rutile TiO_2(110) surface by GGA+U and HSE06 methods. *J. Phys. Condens. Matter* **2012**, *24*, 435504.

(14) Setvin, M.; Franchini, C.; Hao, X.; Schmid, M.; Janotti, A.; Kaltak, M.; Van de Walle, C. G.; Kresse, G.; Diebold, U. Direct view at excess electrons in TiO_2 rutile and anatase. *Phys. Rev. Lett.* **2014**, *113*, 086402.

(15) Kick, M.; Reuter, K.; Oberhofer, H. Intricacies of DFT+U, not only in a numeric atom centered orbital framework. *J. Chem. Theor. Comput.* **2019**, *15*, 1705–1718.

(16) Reticcioli, M.; Setvin, M.; Schmid, M.; Diebold, U.; Franchini, C. Formation and dynamics of small polarons on the rutile TiO_2(110) surface. *Phys. Rev. B* **2018**, *98*, 045306.

(17) Kowalski, P. M.; Camellone, M. F.; Nair, N. N.; Meyer, B.; Marx, D. Charge localization dynamics induced by oxygen vacancies on the TiO_2(110) surface. *Phys. Rev. Lett.* **2010**, *105*, 146405.

(18) Deschanvres, A.; Raveau, B.; Sekkal, Z. Mise en evidence et etude cristallographique d'une nouvelle solution solide de type spinelle $Li_1 + xTi_2 - xO_4$ $0 \leq x \leq 0.333$. *Mater. Res. Bull.* **1971**, *6*, 699 – 704.

(19) Hohenberg, P.; Kohn, W. Inhomogeneous electron gas. *Phys. Rev.* **1964**, *136*, B864–B871.

(20) Perdew, J. P.; Burke, K.; Ernzerhof, M. Generalized gradient approximation made simple. *Phys. Rev. Lett.* **1996**, *77*, 3865–3868.

(21) Cohen, A. J.; Mori-Sánchez, P.; Yang, W. Insights into current limitations of density functional theory. *Science* **2008**, *321*, 792–794.

(22) Hubbard, J. Electron correlations in narrow energy bands. *Proc. R. Soc. A* **1963**, *276*, 238–257.

(23) Anisimov, V.; Zaanen, J.; Andersen, O. K. Band theory and Mott insulators: Hubbard U instead of Stoner I. *Phys. Rev. B* **1991**, *44*, 943–954.

(24) Dudarev, S. L.; Botton, G. A.; Savrasov, S. Y.; Humphreys, C. J.; Sutton, A. P. Electron-energy-loss spectra and the structural stability of nickel oxide: An LSDA+U study. *Phys. Rev. B* **1998**, *57*, 1505–1509.

(25) Dorado, B.; Amadon, B.; Freyss, M.; Bertolus, M. DFT + U. *Phys. Rev. B* **2009**, *79*, 235125.

(26) Allen, J. P.; Watson, G. W. Occupation matrix control of d- and f-electron localisations using DFT + U. *Phys. Chem. Chem. Phys.* **2014**, *16*, 21016–21031.

(27) Kohtani, S.; Kawashima, A.; Miyabe, H. Reactivity of trapped and accumulated electrons in titanium dioxide photocatalysis. *Catalysts* **2017**, *7*, 303.

(28) Diebold, U. The surface science of titanium dioxide. *Surf. Sci. Rep.* **2003**, *48*, 53–229.

(29) Morgan, B. J.; Watson, G. W. GGA+U description of lithium intercalation into anatase TiO_2. *Phys. Rev. B* **2010**, *82*, 144119.

(30) Nasara, R. N.; Tsai, P.-C.; Lin, S.-K. One-step synthesis of highly oxygen-deficient lithium titanate oxide with conformal amorphous carbon coating as anode material for lithium ion batteries. *Adv. Mater. Interfaces* **2017**, *4*.

(31) Park, M.; Zhang, X.; Chung, M.; Less, G. B.; Sastry, A. M. A review of conduction phenomena in Li-ion batteries. *J. Power Sources* **2010**, *195*, 7904 – 7929.

(32) Dutta, A. K. Electrical Conductivity of Single Crystals of Graphite. *Phys. Rev.* **1953**, *90*, 187–192.

(33) Creffield, G. K.; Down, M. G.; Pulham, R. J. Electrical resistivity of liquid and solid lithium. *J. Chem. Soc., Dalton Trans.* **1974**, 2325–2329.

(34) Stenina, I. A.; Il'in, A. B.; Yaroslavtsev, A. B. Synthesis and ionic conductivity of $Li_4Ti_5O_{12}$. *Inorg. Mater.* **2015**, *51*, 62–67.

(35) Blum, V.; Gehrke, R.; Hanke, F.; Havu, P.; Havu, V.; Ren, X.; Reuter, K.; Scheffler, M. Ab initio molecular simulations with numeric atom-centered orbitals. *Comput. Phys. Commun.* **2009**, *180*, 2175–2196.

(36) Himmetoglu, B.; Floris, A.; de Gironcoli, S.; Cococcioni, M. "Hubbard-corrected DFT energy functionals: The LDA+U description of correlated systems". *Int. J. Quantum Chem.* **2014**, *114*, 14–49.

Supplementary Information: Mobile Small Polarons Explain Conductivity in Lithium Titanium Oxide Battery Electrodes

Matthias Kick,[†] Cristina Grosu,[†,‡] Markus Schuderer,[†] Christoph Scheurer,[†] and Harald Oberhofer[*,†]

[†]*Chair for Theoretical Chemistry and Catalysis Research Center, Technical University of Munich, Lichtenbergstr. 4, 85747 Garching, Germany*

[‡]*Institute of Energy an Climate Research (IEK-9), Forschungszentrum Jülich, 52425 Jülich, Germany*

E-mail: harald.oberhofer@tum.de

1 Structures

1.1 Pristine bulk structures

Spinel lithium titanium oxide (LTO, $Li_4Ti_8O_{12}$) crystallizes in the $Fd\overline{3}m$ (No. 227) space group. The O atoms form a face center cubic packing (fcc) and occupy the 32e sites within the cubic unit cell. The titanium atoms and one quarter of the lithium atoms are octahedral cooordinated by oxygen and occupy the 16d sites. The ratio between Li and Ti atoms at these octahedral sites is $\frac{1}{6}$:$\frac{5}{6}$. The remaining Li atoms occupy the 8a sites.[1]

The mixed occupancy of Ti and Li at the 16d sites can not be realized with the conventional cubic unit cell of $Fd\overline{3}m$ as there are only sixteen possible sites resulting in a no integer ratio of Li and Ti atoms if the mixed occupancy would be considered. A suitable

subgroup that allows for the right stoichiometry within a single unit cell is R3$\overline{\text{m}}$ (No. 166). The unit cell of this space group is hexagonal. Within this cell the mixed occupancy can be easily realized. It contains 12 sites corresponding to the 16d sites in Fd3$\overline{\text{m}}$. Among them one has to distribute two Li atoms and ten Ti atoms to achieve the correct ratio. In total this yields $\binom{12}{2} = 66$ possibilities. Among these one can identify 6 unique structures the others are equivalent by symmetry. All of those are different in energy and are denoted c0001 to c0006. All LTO structure are shown in Figure 1.

These configurations are the starting point for our analysis. We performed pure PBE[2] calculations. Table 1 list the obtained results. Among all systems, c0002 is identified to be the most stable configuration. Therefore, we continue our analysis using the c0002 structure.

Table 1: Relative stabilities, E_{rel}^{LTO}, of the different pristine bulk structures. Most stable structure c0002 serves as zero point for the energy scale.

system	E_{rel}^{LTO}[eV]
c0001	0.72
c0002	0.00
c0003	2.14
c0004	4.38
c0005	0.77
c0006	0.36

1.1.1 Computational details

Calculations have been performed using the PBE[2] functional as it is implemented in the CASTEP[3] code using a 4 x 4 x 2 k-point grid. Structures have been fully relaxed until forces where below 10^{-2} eV/Å in combination with a plane wave basis set using an energy cut-off of 600 eV.

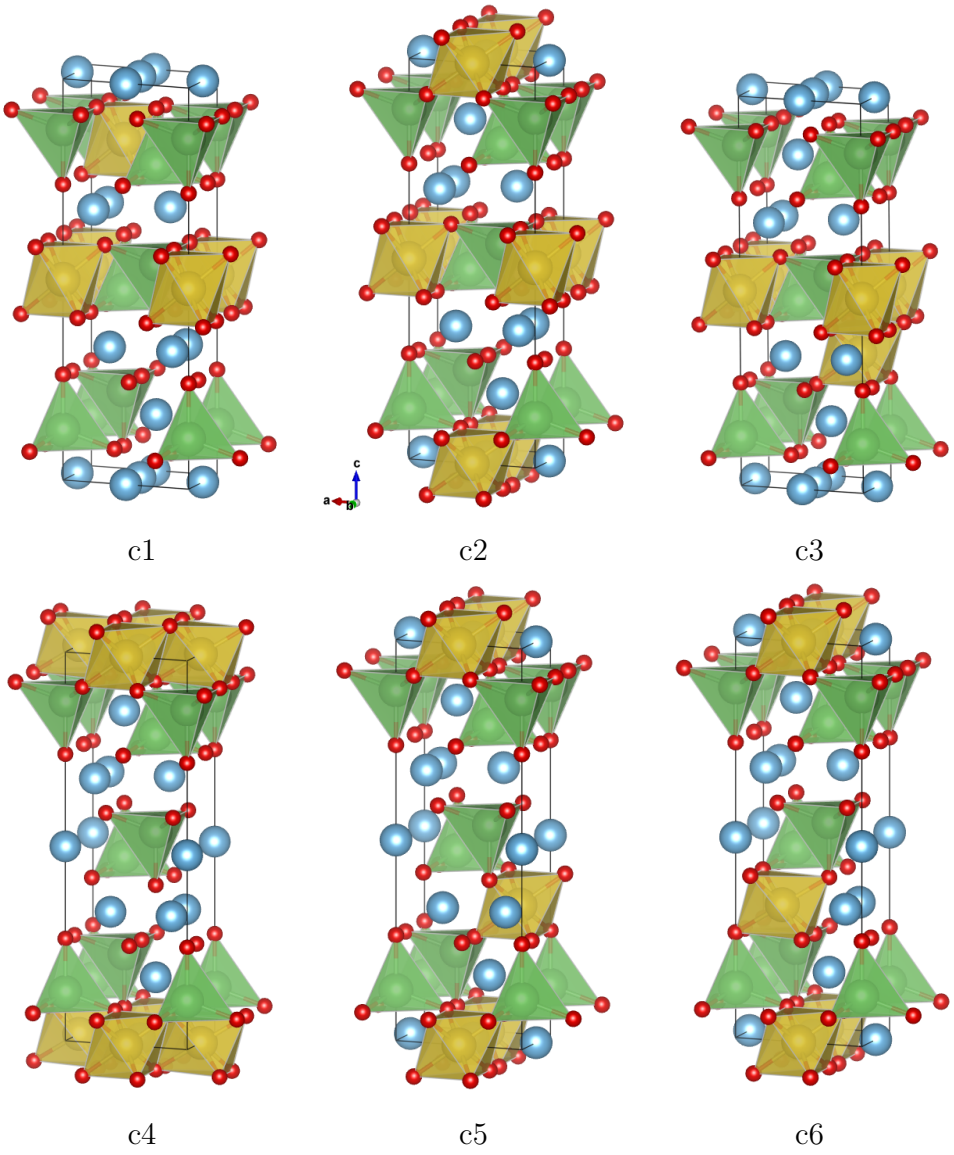

Figure 1: Shown are the different LTO unit cells. Ti atoms are shown in light blue, oxygen atoms are red and Li atoms are shown as green spheres. Tetrahedral and octahedral sites are depicted accordingly.

1.2 Defect bulk structures

Within the c0002 unit cell one can identify nine unique O vacancies all others are equivalent due to symmetry (see Figure 2). For this purpose the Site Occupancy Disorder (SOD) package[4] has been used.

We embedded each of the nine unique oxygen vacancies into 2 x 2 x 1 supercells, yielding a supercell based on three standard defect free unit cells and one with O vacancy. This structural variety of LTO makes computational sampling rather demanding, therefore, as a first starting point we performed full geometry relaxations using only the PBE functional within FHI-aims. Our results are showed in table 2 where the different structures are named from v1 to v9 according to the position of the oxygen vacancy in the primitive cell. Again, the most stable configuration serves as zero point for the energy scale.

We like to highlight, that in principle one has to consider here all possible configurations of this system to find the true configuration which is lowest in energy. Therefore, this should be seen just as a first attempt to tackle the problem. Considering, neutral, single and doubly charged oxygen defects in combination with all possible localization patterns of polarons is by far not tractable as one has to go beyond LDA or GGA approximations in order to correctly describe the defect states.

Among all nine different vacancy configurations we use the most stable one (v3) as the starting point for all further polaron calculations. The supercell of configuration v3 is shown in Figure 3.

1.2.1 Computational details

All calculations have been performed using the PBE functional as implemented in the FHI-aims code with preoptimized structures obtained from CASTEP calculations. Reciprocal space has been sampled using a 2 x 2 x 2 Monkhorst-Pack[5] k-point grid. The structures were fully relaxed until forces have been below 10^{-2} eV/Å applying a *light tier1* basis set.

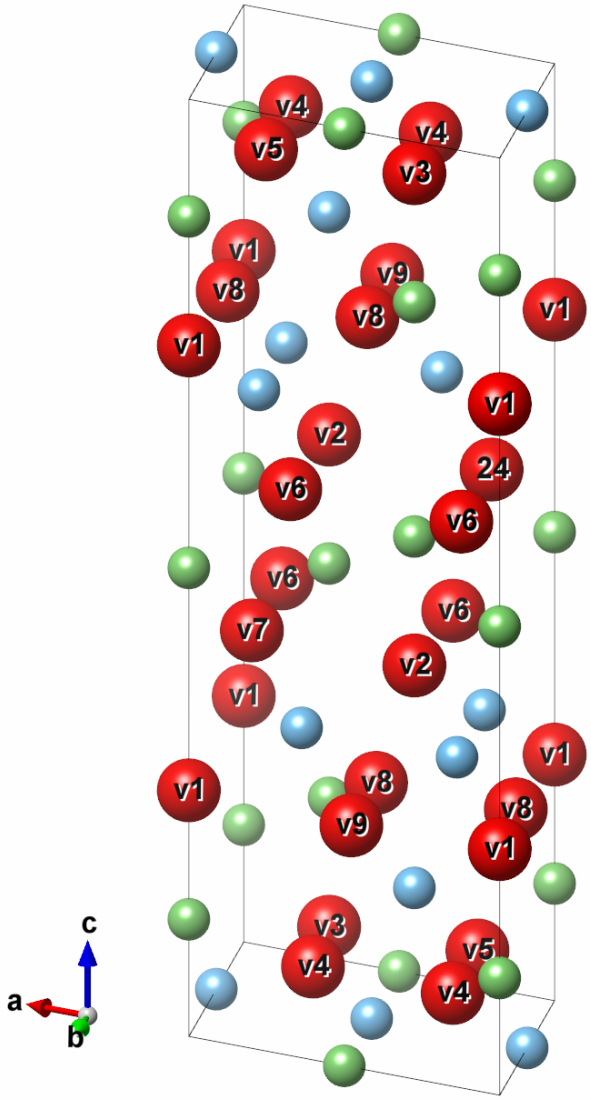

Figure 2: Single unit cell of the c2 LTO structure. Ti atoms are shown in light blue, Li atoms are shown in green and oxygen atoms are displayed as red spheres. The different position for an oxygen vacancy are named from v1 to v9. Double naming indicates a symmetry equivalent site.

Table 2: Relative stabilities, $E_{rel}^{LTO+O_v}$, of the different bulk structures with O vacancy. Most stable structure v3 serves as zero point for the energy scale.

system	$E_{rel}^{LTO+O_v}$[eV]
v1	1.58
v2	1.95
v3	0.00
v4	0.38
v5	1.06
v6	0.87
v7	1.13
v8	0.78
v9	1.13

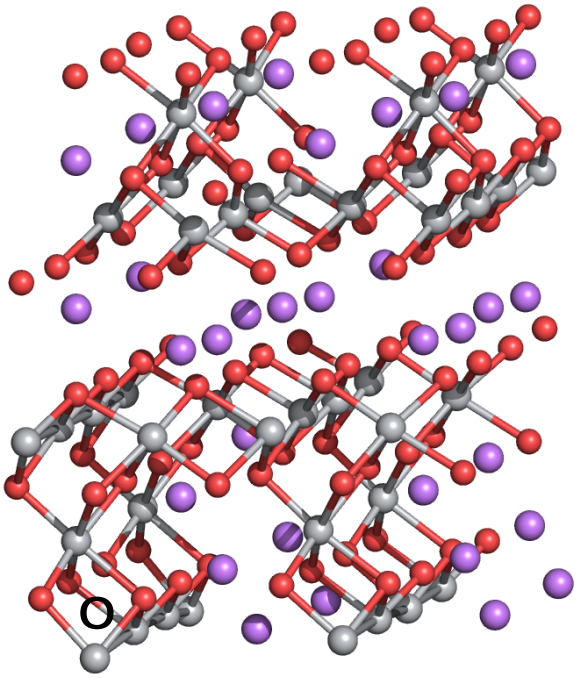

Figure 3: Supercell structure consisting of four LTO c2 cells including the v3 vacancy. The O vacancy is marked with a black circle. Li atoms are purple. O atoms are shown as red spheres. Ti atoms are shown as grey spheres.

2 Polaron calculations

2.1 Localizing the Polarons

From a methodological point of view, a key aspect of DFT+U is the choice of the correct projector-dependent Hubbard U value.[6,7] A common strategy would be to choose the value according to the experimentally determined defect position within the band gap.[7,8] However, owing to the relative novelty of blue LTO, there are no such results to be found in the literature. From TiO_2 the gap state position is experimentally known to be about 1 eV below the conduction band minimum (CBM)[9]. Arguably, titanium atoms in both LTO an TiO_2 are embedded in a similar chemical environment, leading to a similar position of the defect state within the band gap. This assumption is further supported by the observation that both defective TiO_2 and LTO show the same blue color.[10–12] Based on this approximation, all our analysis are conducted with a U value of 2.65 eV, yielding gap states at around 1 eV below the CBM for the most stable polaronic configurations found. For localizing the electrons at different Ti atoms we made use of the matrix control approach[13,14]. We started with the occupation matrices obtained from a pure PBE[2] run and used this as input for the matrix control routines. To obtain electron localization in specific orbitals on a specific Ti atoms, we modified the corresponding diagonal matrix element to 1. Afterwards, full geometry optimization is performed by fixing this modified occupation matrix. To obtain full self-consistency, we used the obtained geometry and the wave function information as input for a second run without constraining the occupation matrix. Table 3 contains the complete list of calculated polaron systems and their relative stabilities. The relative stabilities have been calculated according to

$$E_{\mathrm{rel}} = E_{\mathrm{tot,i}} - E_{\mathrm{tot,\ most\ stable\ structure}} \quad , \tag{1}$$

where $E_{\mathrm{tot,i}}$ is the total energy of a specific configuration and $E_{\mathrm{tot,\ most\ stable\ structure}}$ is the total energy of the most stable configuration. By this, all other less stable configurations show positive energies.[8]

Table 3: Relative stabilities of the calculated polaronic configurations. Here, we only considered triplet configurations. Furthermore, d_{V_O} indicates the distance form the Ti^{3+} center to the next periodic oxygen vacancy in the unit cell. Only the distances within the unrelaxed defect supercell have been considered.

system	E_{rel} [eV]	d_{V_O}[Å]	system	E_{rel} [eV]	d_{V_O}[Å]
L3-7/L2-9	0.00	6.52/7.47	L3-9/L3-12	0.23	5.05/6.55
L3-7/L2-11	0.01	6.52/8.63	L2-8/L2-12	0.23	9.45/7.38
L3-7/L2-10	0.01	6.52/8.50	L2-8/L2-11	0.23	9.45/8.63
L3-7/L2-7	0.02	6.52/7.43	L3-9/L3-10	0.26	5.05/4.92
L2-7/L3-5	0.07	7.43/4.95	L5-1/L3-9	0.43	2.08/5.05
L3-8/L3-4	0.12	6.51/4.93	L5-1/L3-12	0.45	2.08/6.55
L3-11/L3-12	0.12	6.34/6.55	L3-7/L1-3	0.49	6.52/6.69
L3-7/L3-12	0.13	6.52/6.55	L4-2/L4-4	0.75	3.71/3.68
L2-7/L2-8	0.14	7.43/9.45	L4-3/L4-2	0.77	6.99/3.71
L2-7/L2-12	0.15	7.43/7.38	L1-1/L1-4	0.77	6.84/6.70
L3-5/L3-6	0.19	4.95/4.81	L5-5/L4-2	0.82	6.22/3.71
L3-5/L4-2	0.19	4.95/3.71	L4-3/L4-4	1.00	6.99/3.68
L3-7/L3-9	0.20	6.52/5.05	L5-1/L5-5	2.59	2.08/6.22

2.2 Computational details

Electronic structure calculations have been performed entirely using the FHI-aims program package[15]. All structure optimizations have been performed with applying the DFT+U[16–18] variant of the PBE exchange correlation functional using the fully-localized limit (FLL)[6] as double counting correction. The Ti 3*d* atomic basis functions serve as Hubbard projectors in each run. Only the on-site representation[19] for the DFT+U occupation matrix have been used in combination with a U value of 2.65 eV. Numerically convergence have been already reached with a *tight tier1* basis set. Reciprocal space has been sampled using a 2 x 2 x

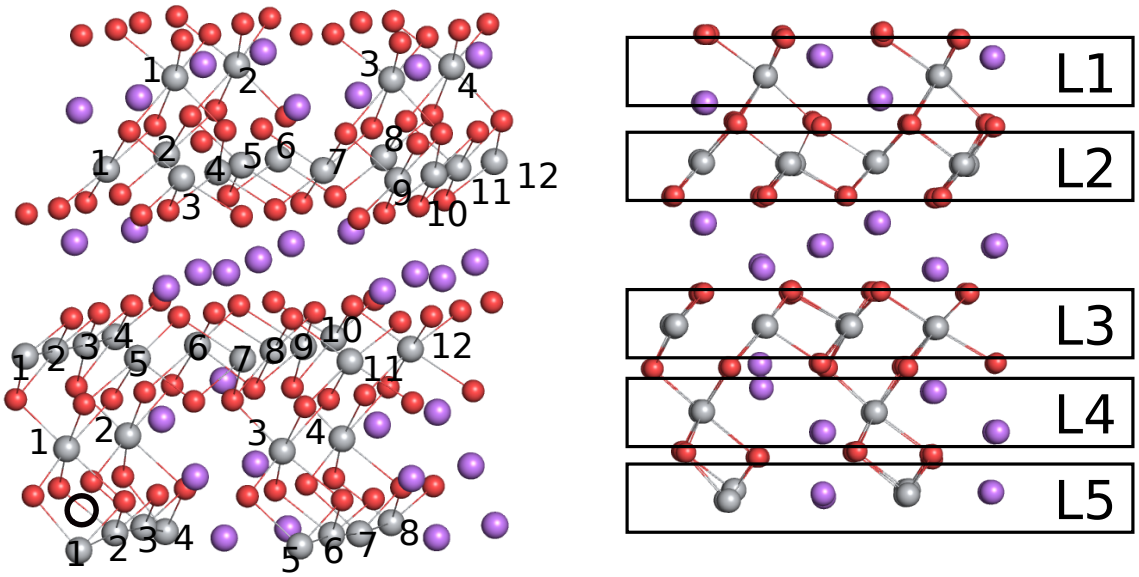

Figure 4: Site naming convention of the different localization patterns. Lx-m/Ly-n thus specifies the localization of one electron within layer Lx on atom m with the second electron localized in layer Ly on atom n. The position of the oxygen vacancy is also marked with a black circle. Titanium atoms are depicted as grey spheres, oxygen atoms are shown as red spheres.

2 Monkhorst-Pack[5] k-point grid. The structures were fully relaxed until forces have been below 10^{-2} eV/Å.

If not otherwise noted, all structures related to the polaron calculations have been fully optimized with PBE+U(=2.65) only.

3 Barrier calculations

3.1 Obtaining the barrier profile

For the barrier profiles we again make use of the matrix control approach. However, instead of fixing all the occupation matrices we only fix the occupation matrices of the atoms between which we assume electron hopping to occur. In detail we studied the hopping of one electron from L3-7/L2-3 to L3-7/L1-9 and from L3-7/L2-10 to L3-7/L2-9. For this we define a reaction coordinate x which describes the occupation matrices of both atoms between the

hopping process. The occupation matrix $\mathbf{n}'$ for a certain atom A and a certain atom B is then defined according to

$$\mathbf{n}'_A = x\mathbf{n}_A^{\mathrm{Ti}^{3+}} + (1-x)\mathbf{n}_A^{\mathrm{Ti}^{4+}} \quad , \tag{2a}$$

$$\mathbf{n}'_B = (1-x)\mathbf{n}_B^{\mathrm{Ti}^{3+}} + x\mathbf{n}_B^{\mathrm{Ti}^{4+}} \quad . \tag{2b}$$

$\mathbf{n}^{\mathrm{Ti}^{3+}}$ is the occupation matrix where the excess electron is fully localized at a certain atom, this occupation matrix is obtained from a full self-consistent calculation as it is described in section 2.1. $\mathbf{n}^{\mathrm{Ti}^{4+}}$ is the occupation matrix at a certain atom if none of the excess electrons is localized. Going from L3-7/L2-10 to L3-7/L2-9 this means $\mathbf{n}_A^{\mathrm{Ti}^{3+}}$ belongs to the self-consistent occupation matrix of L2-9 in system L3-7/L2-9 and $\mathbf{n}_A^{\mathrm{Ti}^{4+}}$ belongs to the occupation matrix of atom L2-9 in the L3-7/L2-10 system. Occupation matrix $\mathbf{n}_B^{\mathrm{Ti}^{3+}}$ would then be the self-consistent occupation matrix of atom L2-10 in system L3-7/L2-10 and $\mathbf{n}_B^{\mathrm{Ti}^{4+}}$ corresponds to the self-consistent occupation matrix of atom L2-10 in system L3-7/L2-9. As a next step we performed full structure relaxations with applying the above described constraints. This means that our chosen reaction coordinate directly translates also to a structural change along the reaction path. Table 4 lists the obtained energies with respect to the configuration lowest lying in energy. However, this is the energy with applied constraints from the matrix control approach. In addition, in order to further judge the quality of this approach we use the obtained wave-function information from the saddle point and evaluate the DFT+U functional again without constraining the occupation matrices (red points in Figure 5). This gives a direct estimate how the electron density is able to adapt to the applied bias potential. For the transition L3-7/L2-10 to L3-7/L2-9 depicted in Figure 5a both energies agree remarkable well, with a difference of only about 6 meV. For the other transition considered here, L3-7/L1-3 to L3-7/L2-9, (Figure 5b) the difference is with 56 meV significantly larger. To analyse this further, we calculated the difference in the sum of the diagonal elements between applied occupation matrix $\mathbf{n}'$ and the actual occupation matrix

Table 4: Listed are the points calculated for the barrier profile which is shown in figure 5. All points have been calculated from the matrix-control run. The lowest energy configuration serves as zero point for the energy scale. The notation in brackets corresponds to the self-consistent polaron configuration.

x	L3-7/L2-10 → L3-7/L2-9 [eV]	L3-7/L2-3 → L3-7/L1-9 [eV]
0.00	0.008	0.485
	(L3-7/L2-10)	(L3-7/L1-3)
0.10	0.024	0.501
0.25	-	0.565
0.30	0.123	0.583
0.40	0.170	-
0.45	-	0.483
0.50	0.186	0.416
0.60	0.166	0.280
0.70	0.118	0.162
0.80	-	0.074
0.90	0.016	0.019
1.00	0.000	0.000
	(L3-7/L2-9)	(L3-7/L2-9)

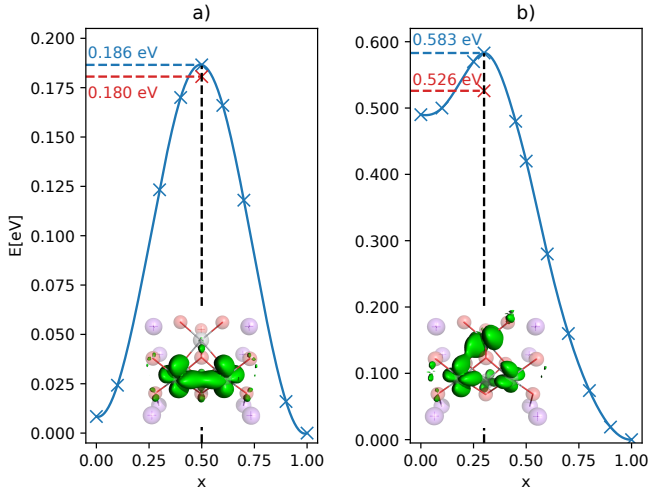

Figure 5: Calculated barrier profile for the transition L3-7/L2-10 to L3-7/L2-9 (a) and L3-7/L1-3 to L3-7/L2-9 (b). x = 1.0 is equal to configuration L3-7/L2-9. Blue points are energies obtained with fixed occupation matrix according to eq. 2a in both subfigures. Red points are DFT+U energies calculated from the wave-function obtained from the matrix control run. The lowest lying configuration in energy serves as zero point for the energy scale. Also shown is the spin density of the corresponding transition state. Isosurface level 0.015 eÅ^{-3}.

n determined from the wave function at the transition state points, $\Delta = \sum_n |n'_{nn}| - |n_{nn}|$. For transition L3-7/L2-10 to L3-7/L2-9 the highest deviation is for the occupation of L2-9 with a value of 0.036. Contrary, for transition L3-7/L1-3 to L3-7/L2-9 our analysis yields a deviation of 0.176 for the occupation matrix at L2-8. This large difference is due to the electron not only being located at L2-8 and L1-3 but also at neighboring titanium atoms. This might indicate that the applied bias potential does not fit the transition state equally well as in the case of the L3-7/L2-10 to L3-7/L2-9 transition and hence is responsible for the observed difference in barrier height. However, this problem is closely related to the problem of defining proper fragments in CDFT.[20] Yet, given the fact that this specific transition already shows a significant energy difference of 485 meV between the two stable states, this discrepancy is most likely of minor importance. Our new approach is thus capable of gauging hopping barriers at nearly no overhead over standard DFT calculations. Our results which we obtain for a U value of 2.65 eV are listed in table 5. It should be highlighted, that

Table 5: Barrier heights calculated from the density obtained from the matrix control run.

x	L3-7/L2-10 → L3-7/L2-9 [eV]	L3-7/L2-3 → L3-7/L1-9 [eV]
0.30	-	0.526
0.50	0.180	-

the obtained barriers sensitively depend on the applied U value, however, this is a general aspect of DFT+U and not a result of the here applied strategy for obtaining the barrier profiles. Moreover, hybrid functionals should suffer from this drawback too. The U value in DFT+U determines the strength of the on-site coulomb repulsion and hence it determines the amount of how DFT+U will accounts for the self-interaction error. In hybrid functional the mixing factor determines the amount of exact exchange and hence how much a specific hybrid functional accounts for the self-interaction error.

3.1.1 Marcus reaction coordinate

Going along reaction coordinate x the polaron hopping from atom A to atom B occurs as the system passes the transition state. By again exploiting the matrix control approach one is able to constrain the electron at a certain atom and thus preventing the electron to hop. In figure 6 we are showing the corresponding results. Blue dots have been obtained as described in section 3.1, for orange dots we use the structure obtained for a certain x and use the occupation matrix control to constrain the polaron to one specific site. No geometry relaxation have been allowed during that procedure.

In a next step, this allows to define a new reaction coordinate according to,

$$\Delta E = E\left(x, A\right) - E\left(x, B\right) \quad . \tag{3}$$

Here, $E\left(x, A\right)$ is the energy if the electron is located on atom A. Whereas $E\left(x, B\right)$ is the energy if the electron is located at atom B. For both energies the same geometry has been

used. In Figure 7 we show the new reaction profile. Clearly, Figure 7b indicates an early transition state for the hopping from L3-7/L1-3 to L3-7/L2-9.

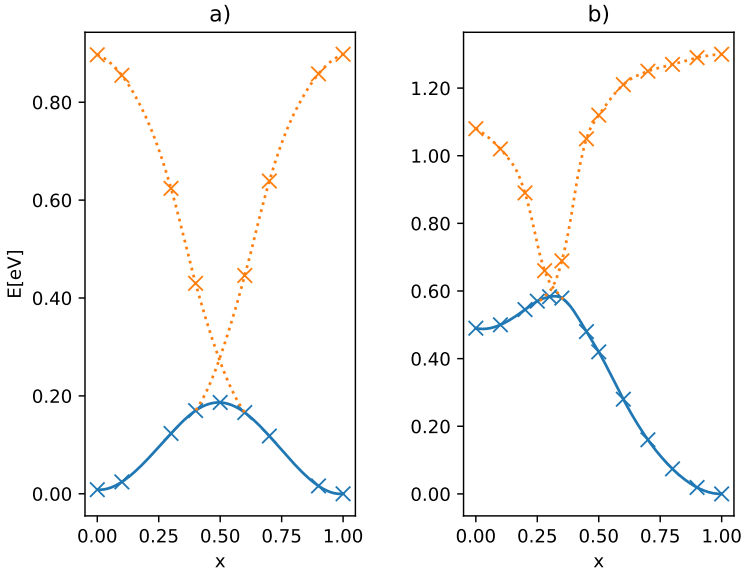

Figure 6: Full reaction profile according to reaction coordinate x which defines the occupation matrices according to eq. 2a and eq. 2b respectively. Blue curve and blue points have been obtained according to the description in section 3.1. L3-7/L2-10 to L3-7/L2-9 is shown in (a) and L3-7/L1-3 to L3-7/L2-9 is depicted in (b). x = 1.0 is equal to configuration L3-7/L2-9.

3.2 Computational details

For the barrier calculations we applied the same computational settings as described in section 2.2.

References

(1) Scharner, S.; Weppner, W.; SchmidBeurmann, P. Evidence of twophase formation upon lithium insertion into the $Li_{1.33}Ti_{1.67}O_4$ spinel. *J. Electrochem. Soc.* **1999**, *146*, 857–861.

(2) Perdew, J. P.; Burke, K.; Ernzerhof, M. Generalized gradient approximation made simple. *Phys. Rev. Lett.* **1996**, *77*, 3865–3868.

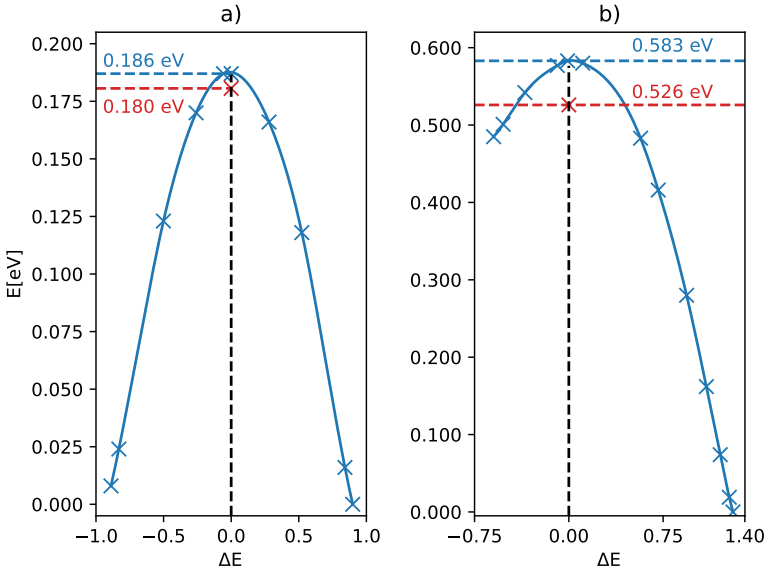

Figure 7

(3) J. Clark, S.; Segall, M.; J. Pickard, C.; Hasnip, P.; Probert, M.; Refson, K.; C. Payne, M. First principles methods using CASTEP. *Z. Kristallogr.* **2005**, *220*.

(4) Grau-Crespo, R.; Hamad, S.; Catlow, C. R. A.; de Leeuw, N. H. Symmetry-adapted configurational modelling of fractional site occupancy in solids. *J. of Phys. Condens. Matter* **2007**, *19*, 256201.

(5) Monkhorst, H. J.; Pack, J. D. Special points for Brillouin-zone integrations. *Phys. Rev. B* **1976**, *13*, 5188–5192.

(6) Himmetoglu, B.; Floris, A.; de Gironcoli, S.; Cococcioni, M. "Hubbard-corrected DFT energy functionals: The LDA+U description of correlated systems". *Int. J. Quantum Chem.* **2014**, *114*, 14–49.

(7) Kick, M.; Reuter, K.; Oberhofer, H. Intricacies of DFT+U, not only in a numeric atom centered orbital framework. *J. Chem. Theor. Comput.* **2019**, *15*, 1705–1718.

(8) Deskins, N. A.; Rousseau, R.; Dupuis, M. Distribution of Ti^{3+} surface sites in reduced TiO_2. *J. Phys. Chem. C* **2011**, *115*, 7562–7572.

(9) Yim, C. M.; Pang, C. L.; Thornton, G. Oxygen vacancy origin of the surface band-gap state of TiO_2(110). *Phys. Rev. Lett.* **2010**, *104*, 036806.

(10) Diebold, U. The surface science of titanium dioxide. *Surf. Sci. Rep.* **2003**, *48*, 53–229.

(11) Nasara, R. N.; Tsai, P.-C.; Lin, S.-K. One-step synthesis of highly oxygen-deficient lithium titanate oxide with conformal amorphous carbon coating as anode material for lithium ion batteries. *Adv. Mater. Interfaces* **2017**, *4*.

(12) Qiu, J.; Lai, C.; Gray, E.; Li, S.; Qiu, S.; Strounina, E.; Sun, C.; Zhao, H.; Zhang, S. Blue hydrogenated lithium titanate as a high-rate anode material for lithium-ion batteries. *J. Mater. Chem. A* **2014**, *2*, 6353–6358.

(13) Dorado, B.; Amadon, B.; Freyss, M.; Bertolus, M. DFT + U. *Phys. Rev. B* **2009**, *79*, 235125.

(14) Allen, J. P.; Watson, G. W. Occupation matrix control of d- and f-electron localisations using DFT + U. *Phys. Chem. Chem. Phys.* **2014**, *16*, 21016–21031.

(15) Blum, V.; Gehrke, R.; Hanke, F.; Havu, P.; Havu, V.; Ren, X.; Reuter, K.; Scheffler, M. Ab initio molecular simulations with numeric atom-centered orbitals. *Comput. Phys. Commun.* **2009**, *180*, 2175–2196.

(16) Hubbard, J. Electron correlations in narrow energy bands. *Proc. R. Soc. A* **1963**, *276*, 238–257.

(17) Anisimov, V.; Zaanen, J.; Andersen, O. K. Band theory and Mott insulators: Hubbard *U* instead of Stoner *I*. *Phys. Rev. B* **1991**, *44*, 943–954.

(18) Dudarev, S. L.; Botton, G. A.; Savrasov, S. Y.; Humphreys, C. J.; Sutton, A. P. Electron-energy-loss spectra and the structural stability of nickel oxide: An LSDA+U study. *Phys. Rev. B* **1998**, *57*, 1505–1509.

(19) Eschrig, H.; Koepernik, K.; Chaplygin, I. Density functional application to strongly correlated electron systems. *J. Solid State Chem.* **2003**, *176*, 482–495.

(20) Oberhofer, H.; Blumberger, J. Electronic coupling matrix elements from charge constrained density functional theory calculations using a plane wave basis set. *J. Chem. Phys.* **2010**, *133*, 244105.